POLITECNICO
MILANO 1863

Department of Chemistry, Materials and Chemical Engineering "Giulio Natta"
Doctoral Program in Material Engineering 34th cycle

HUMIDITY-RESPONSIVE LAYERED SELF-ACTUATOR

Doctoral dissertation of: Shiva Khoshtinat

Supervisors: Claudia Marano, Valter Carvelli
Tutor: Giovanni Dotelli

POLITECNICO
MILANO 1863

Department of Chemistry, Materials and Chemical Engineering "Giulio Natta"

Doctoral Program in Material Engineering 34th cycle

HUMIDITY-RESPONSIVE LAYERED SELF-ACTUATOR

Doctoral dissertation of: Shiva Khoshtinat

Supervisors: Claudia Marano, Valter Carvelli

Tutor: Giovanni Dotelli

Abstract

This project aims to develop and characterize a low-cost humidity-responsive self-actuator that exploits the dimensional variation mismatch between a hygroscopic material (used as an active layer for coating) and a non or less-hygroscopic substrate, due to changes in the humidity level of the environment. For this goal, a cellulose-based polymer, namely a cellulose acetate (CA), was chosen as a highly hygroscopic material. A systematic investigation of cellulose acetate membrane fabrication to produce the appropriate membrane for the project's intended purpose was performed. The effect of the type of solvent adopted for CA solution preparation, CA concentration, casting process, and solvent evaporation method was analyzed.

After optimizing the manufacturing process of cellulose acetate membranes, surface morphology, thermal, and mechanical properties of the membranes are studied. The hygroscopic behavior of this material and the parameters governing the moisture diffusion process and the relevant material expansion are investigated. Material properties such as moisture diffusion coefficient, moisture concentration at saturation and moisture absorption induced expansion were evaluated.

The moisture diffusion in cellulose acetate membranes has been investigated via gravimetric measurements and the dependency of the CA moisture concentration at saturation on the environment's humidity level was characterized. The non-Fickian behavior of moisture diffusion in cellulose acetate membranes was characterized using an analytical model, which enabled the influence of both membrane thickness and relative humidity level to be considered across a wide range of the experimental campaign. A finite element model has been developed to predict this non-Fickian behavior.

The moisture absorption induced expansion of cellulose acetate membranes has been characterized as a function of relative humidity via Thermomechanical Analysis (TMA). A finite element model that combines the moisture diffusion process and the hygroscopic mechanical deformation induced in the membrane is presented. Finally, the response of a humidity-responsive bilayer self-actuator consisting of the characterized cellulose acetate membrane as active layer and a non-hygroscopic substrate was investigated. The bending curvature induced in the bilayer composite by an environment humidity variation was compared to a generally used analytical model, which is complemented by a finite element model.

Thesis Structure

The study intends to develop a model to describe the manufacturing process and the hygroscopic behavior of a cellulose acetate based humidity-responsive layered self-actuator. The path to achieve the project's goal may be divided into three main steps:

- Offering a systematic procedure for the fabrication of hygroscopic membranes,
- Determining and defining the inherent properties of these membranes that are important in the material's hygroscopic behavior,
- Development of a comprehensive finite element model that can take advantage of the known intrinsic properties of the hygroscopic membrane in order to predict the reaction of a bi-layered self-actuator to changes in relative humidity.

In this context, the structure of this thesis is as follow:

- ***Chapter 1*** discusses the inspiring idea and specified major purpose of this research. The state of the art on smart materials for self-actuator and a brief overview of conceptual solutions are presented. Finally, the potential use of hygroscopic material for the humidity-responsive self-actuator is discussed.
- ***Chapter 2*** outlines the theory of hygroscopic behavior and the material properties involved in sensitivity to variations in relative humidity of the environment. A brief review on the experimental techniques commonly adopted for hygroscopic materials' characterization are summarized and compared. The main modeling approaches adopted in the last decade for the description of this behavior are reviewed. Moreover, the framework for the experimental characterizations and numerical modeling that have been carried out through this research is presented.
- ***Chapter 3*** offers an introduction to the structural and physical properties of cellulose acetate. The experimental method optimized to generate a pure cellulose acetate membrane starting from the cellulose acetate powder is described. The morphological, thermal, and mechanical characterization of the membrane produced through such a process are presented.
- ***Chapter 4*** introduces the moisture diffusion anomaly in hygroscopic materials. The analytical model for interpreting the non-Fickian sigmoidal behavior of moisture diffusion in cellulose acetate membrane is reviewed in depth. An experimental characterization has been carried to evaluate the moisture absorption process in CA membrane in relation to environment relative humidity and membrane thickness. A detailed finite element model using experimentally determined material properties such as

relaxation factor (β), diffusion coefficient (D), and moisture concentration at saturation (C_{sat}) as a function of relative humidity at constant temperature is presented.

- ***Chapter 5*** discusses the experimental methodology adopted to perform the Thermomechanical Analysis on cellulose acetate membranes to quantify the induced hygroscopic strain (ε_{hygro}) by moisture absorption at equilibrium condition (saturation state) for different values of humidity levels. Furthermore, the dependency of the coefficient of hygroscopic expansion (α) as a function of relative humidity is described, and a numerical model predicting CA membrane hygroscopic behavior at different relative humidity values has been presented.
- ***Chapter 6*** offers a study of the response of a humidity-responsive bi-layered self-actuator created by the coupling of the characterized cellulose acetate membrane and a non-hygroscopic substrate to environmental humidity variations. The adopted experimental setup, test procedure, and result analysis technique are presented. The finite element model for the prediction of the self-actuators' behavior is provided. The outcomes of experimental, numerical, and analytical model for the bending movement of the self-actuator in response to variation in environment relative humidity are compared.

Contents

Abstract I

Thesis Structure III

List of Tables IX

List of Figures XI

1 From Emergency Shelters to Humidity-responsive Self-actuator 1

1.1 Introduction 2

1.2 Possible solutions 3

1.3 Decision-making criteria and project's goal 7

References 9

2 Hygroscopic Materials: Applications and Characterization 17

2.1 Introduction 18

2.2 Progress in exploiting hygroscopic materials 20

2.3 Hygroscopic materials 24

2.4 Bilayer composite production 27

2.5 Hygroscopic properties and governing parameters 30

2.6 Descriptive models 35

2.7 Project framework 37

References 42

3 Cellulose Acetate Membrane 51

3.1 Cellulose-based materials 52

3.2 Membrane Preparation 54

3.3 Scanning Electron Microscopy (SEM) 65

3.4 Thermal properties 67

3.4.1 Differential Scanning Calorimetry (DSC) 67
3.4.2 Thermogravimetric Analysis (TGA) 68
3.5 Mechanical characterization 71
References 75
4 Moisture Diffusion 79
4.1 Moisture diffusion kinetic in hygroscopic materials 80
4.2 Gravimetric measurements 84
4.3 Analytical model 87
4.4 Finite Element Modeling 91
References 97
Appendix 4. 1. The "variable surface concentration model" parametric study 100
Appendix 4. 2. Complete gravimetric measurements 103
Appendix 4. 3. Python script developed for the best fitting of the experimental by the analytical model 106
Appendix 4. 4. Complete set of material characteristics by best fitting 109
Appendix 4. 5. Simulation of the non-Fickian Diffusion for two CA membranes differing in their thicknesses 111
5 Hygroscopic Strain and Coefficient of Hygroscopic Expansion 113
5.1 Introduction 114
5.2 Thermomechanical Analysis 116
5.3 Coefficient of Hygroscopic Expansion ($\boldsymbol{\alpha}$) 120
5.4 Finite Element Modeling 122
References 126
Appendix 5. 1. Image correlation 129
Appendix 5. 2. Thermomechnical analysis with macro-expansion probe 133

Appendix 5. 3. Thermomechanical Analysis experimental data ... 134
Appendix 5. 4. Thermal expansion of cellulose acetate membrane ... 136
6 Bending Deformation of Humidity-responsive Self-actuator ... 137
6.1 Introduction ... 138
6.2 Bending cantilever experiments ... 139
6.2.1 Preparation of the bilayered ... 139
6.2.2 Experimental setup ... 140
6.2.3 Experimental results ... 142
6.3 Finite element modeling ... 146
6.4 Results and comparisons ... 149
References ... 152
Appendix 6. 1. Parametric study of the bending cantilever model ... 154
Appendix 6. 2. Evolution of bending curvature of specimen $\boldsymbol{S1}$ in time ... 157
Appendix 6. 3. Curvature at RH = 17 % ... 158
7 Conclusions and Further Developments ... 159
Acknowledgement ... 165

List of Tables

Table 2. 1. Details of publications in building construction area exploring hygroscopic materials 22

Table 2. 2. Details of publications in sensors development area exploring hygroscopic materials 23

Table 2. 3. A summary of the experimental techniques adopted for the characterization of hygroscopic behavior as reported in literature 31

Table 3. 1. Details of publications in building construction area exploring hygroscopic materials 55

Table 4. 1. Details of gravimetric measurement specimen and condition 85

Table 4. 2. Finite element simulation inputs 94

Table 5. 1. Details and input parameters of the specimens simulated by finite element model. 123

Table 6. 1. Bi-layered specimens' geometry at 25 °C and RH = 35% and experimental conditions. 140

Table 6. 2. Materials' properties values used for the finite element simulations. 146

List of Figures

Figure 1. 1. Possible solutions by exploring piezoelectric fibers or membrane 3

Figure 1. 2. Possible solutions using conductive fibers or coating.. 4

Figure 1. 3. Possible solutions combining piezoelectric and conductive materials for textile fiber 4

Figure 1. 4. Possible solutions exploiting hygroscopic materials as fiber sheath or membrane 6

Figure 2. 1. Hygroscopic behavior of cellulose in presence of water molecules....................................... 18

Figure 2. 2. (a) Schematic representation for the geometrical deformation of an isotropic hygroscopic material based 1D, 2D or 3D product, (b) Schematic representation of humidity-induced bending of a bi-layered composite... 19

Figure 2. 3. Number of publications in the area building construction and sensor exploiting the hygroscopic behavior of materials.. 20

Figure 2. 4. HygroSkin: Meteorosensitive Pavilion, 2013, Achim Menges, Permanent Collection, FRAC Centre Orleans 50... 24

Figure 2. 5. Project framework 41

Figure 3. 1. Resources for different cellulose-based materials... 52

Figure 3. 2. Designed experimental layout for the optimization of membrane preparation procedure .. 56

Figure 3. 3. Variation in time for membranes weight, normalized to its value at time zero 60

Figure 3. 4. Microscope image of dried membrane, a) in climatized room, b) under hood, (microscope: Olympus BX-60 equipped with Infinity 2 camera).. 60

Figure 3. 5. Mean value of the normalized weight as a function of time and standard deviation for six membranes dried for 3 h in a closed chamber and then under vacuum 62

Figure 3. 6. Schematic representation of the optimized procedure for membrane production and drying process 64

Figure 3. 7. SEM image of the membrane dried in closed chamber and vacuum a) a view of membrane surface and its cross section b) detail of the cross section. 66

Figure 3. 8. Differential Scanning Calorimetry thermograms of CA powder and membranes 68

Figure 3. 9. Thermogravimetric analysis, a) the average normalized residual mass of CA powder and membrane (three specimens each), b) Detail of the normalized mass loss caused by water desorption together with standard error (semi-transparent area) 70

Figure 3. 10. Uniaxial tensile test of cellulose acetate membranes (RH=38%) 72

Figure 3. 11. Uniaxial tensile test of cellulose acetate membranes in different conditions (semi-transparent area indicates the standard error). 74

Figure 4. 1. Schematic representation of mass transport phenomenology for absorption and desorption in polymers, adapted from 1 and 4, where RD is the diffusion rate and RR is the relaxation rate. 81

Figure 4. 2. Some experimental results for gravimetric measurements a) Repeatability of moisture absorption for a membrane with a thickness ha = 66 ± 1.5 μm at 40 % relative humidity, b) The membrane's moisture absorption at 50 % RH for various thicknesses. 86

Figure 4. 3. Analytical model interpolation of moisture absorption experimental data obtained at RH=50% with three membranes different in their thickness. 87

Figure 4. 4. Determined values by the best fitting of the analytical model to the experimental data for, a) Relaxation constant (β), b) Diffusion coefficient (D). 88

Figure 4. 5. Average moisture concentration at saturation ($Csat$) as a function of relative humidity (RH) (bars represent the standard deviation). 89

Figure 4. 6. Finite element model: (a) Specimen dimensions, discretization, and boundary conditions; (b) elements for monitoring concentration at each time increment. 92

Figure 4. 7. Simulation of moisture diffusion over thickness using Fickian (left) and non-Fickian (right) behavior, each curve represents a time interval of 5 seconds. 93

Figure 4. 8. Finite Element simulations and experimental data comparison 95

Figure 4. 9. Finite Element Modelling validation: comparison between the experimental results (symbols) of moisture absorption tests carried out on CA specimens' others than the ones used for model definition and the relevant FEM predictions (continuous lines). 96

Figure AP4. 1. Parametric study of the "variable surface concentration model" 102

Figure AP4. 2. Complete gravimetric measurements 105

Figure AP4. 3. Finite element Simulation of the non-Fickian Diffusion for different thicknesses 111

Figure 5. 1. a) Specimen thermal history and relevant length change as measured in a Thermomechanical test, b) Mechanical deformation of the membrane due to applied force at the beginning of the test 118

Figure 5. 2. Thermomechanical Analysis and the best-fitting polynomial for hygroscopic strain (bars represent data semi-dispersion of measurements) 119

Figure 5. 3. (a) hygroscopic strain and concentration at saturation as a function of relative humidity, (the domain containing experimental data and extrapolation of the polynomial fit are shown by the continuous and dashed lines, respectively), (b) hygroscopic strain as a function of moisture concentration at saturation, (c) coefficient of hygroscopic expansion (α) as function of relative humidity 121

Figure 5. 4. Finite element model's details 123

Figure 5. 5. Comparison of experimental and finite element simulation for hygroscopic stresses 125

Figure AP5. 1. Illustration of the specimen preparation and image analysis procedures 130

Figure AP5. 2. a) Hygroscopic strain determined by image analysis of a membrane in its dry and saturated condition reached after exposure to a relative humidity of 38 %, b) Hygroscopic strain determined by the same image analysis procedure for 3 areas of interest repeated 3 time, where the numbers in the subscript of ε refer to the number of the area and the repetition time, respectively. Hollow squares inside the boxes and the bars represent the mean value and variation range within 1.5 of the interquartile range IQR, respectively. 132

Figure AP5. 3. Thermomechnical analysis with macro-expansion probe 133

Figure AP5. 4. Complete set of Thermomechanical Analysis 135

Figure AP5. 5. Thermal expansion of cellulose acetate membrane 136

Figure 6. 1. Schematic illustration of the experimental setup 141

Figure 6. 2. A digital image of Specimen S1 after 100 minutes of exposure to relative humidity of 80 % in the closed chamber (continuous blue line is the considered arc for the calculation of the bending curvature and the dotted blue line is the effect of the slight twist). 142

Figure 6. 3. Experimental results of bending curvature of bilayer self-actuators in response to changes in relative humidity 143

Figure 6. 4. Evolution of bending curvature in time in cyclic variation of relative humidity for specimen S1 144

Figure 6. 5. Evolution of bending curvature in time in cyclic variation of relative humidity for specimen S3 145

Figure 6. 6. Details of the finite element model.. 147

Figure 6. 7. (a) Finite element simulation of self-actuator deformation; (b) Comparison of final deformation between experimental data and numerical model for specimen equilibrated at RH = 80% (Staring relative humidity for the simulation and the experiment are 0% and 35%, respectively) 150

Figure 6. 8. Comparison of experimental data, analytical and numerical models. 151

Figure AP6. 1. Parametric study of the bending cantilever model... 156

Figure AP6. 2. Digital images of bending curvature evolution of specimen S1 in time......................... 157

Figure AP6. 3. Bending curvature of the bilayer self-actuator at relative humidity of 17%................... 158

1 From Emergency Shelters to Humidity-responsive Self-actuator

In this chapter, the origin and the problem definition of the research topic are discussed. State of the art on smart textiles and a brief overview of possible solutions for the defined problem are presented. After evaluating the opportunities and obstacles of each solution, hygroscopic materials have been selected as the most suitable one. Finally, the possible application of hygroscopic materials for a humidity-responsive self-actuator is described.

1.1 Introduction

The inadequacy of comfort and insulation in currently used emergency shelters, primarily in terms of respiratory difficulties, has been highlighted repeatedly by emergency supporting organizations (NOGs). This issue stems from the textiles used to cover the tents, which are inefficient in response to changes in the environment. The study reported in this thesis evolved from the idea of empowering these textiles with the ability of automatic response to environmental stimuli. Recently, the development of these so-called smart textiles have received a lot of interest in different industries [1–21]. Production of these textiles requires a meticulous design from the microscopic to the macroscopic scale. The smart textile's features depend on many factors such as materials, production method, scale of application (micro to macro), and level of application in the production process (weaving [16,22,23], coating [24–27], knitting [2,28,29]).

Smart Textiles that are defined as textile products such as fibers and filaments, yarns together with woven, knitted or non-woven structures, which integrate a high "level of intelligence" to interact with the environment or user [30]. In their review article, Stoppa and Chiolerio [30] divided the level of intelligence of smart textile into three subgroups.

- **Passive smart textiles** are only able to sense the environment/user with sensors but are not able to respond.
- **Active smart textiles**, on the other hand, can sense the stimuli from the environment and react to the changes based on the designed response from the actuator.
- **Very smart textiles** are able to sense, react and adapt their behavior to the given circumstances simultaneously without the need of sensors or processor devices.

Among the materials that could be augmented to currently used textiles, piezoelectric [1,22,29–38], conductive [2,13,23,28–30,36,39–44], and hygroscopic [25,27,45–75] materials have been considered as possible choices for the design of an environmentally-responsive smart textile to enhance the level of comfort in emergency shelter tents.

1.2 Possible solutions

The most profitable application of piezoelectric materials, which are able to transform mechanical energy into electrical energy and vice versa, for the goal of this thesis project is energy harvesting [22,31,32]. Woven textiles produced by piezoelectric filament or fibers, or piezoelectric membrane can provide the possibility of harvesting energy when the textile is under tension (e.g. in windy conditions, see Figure 1. 1). The most convenient piezoelectric materials for the limits of this project are piezoelectric polymers such as Poly (vinylidene fluoride) (PVDF), due to its low density, high tensile strength, and flexibility.

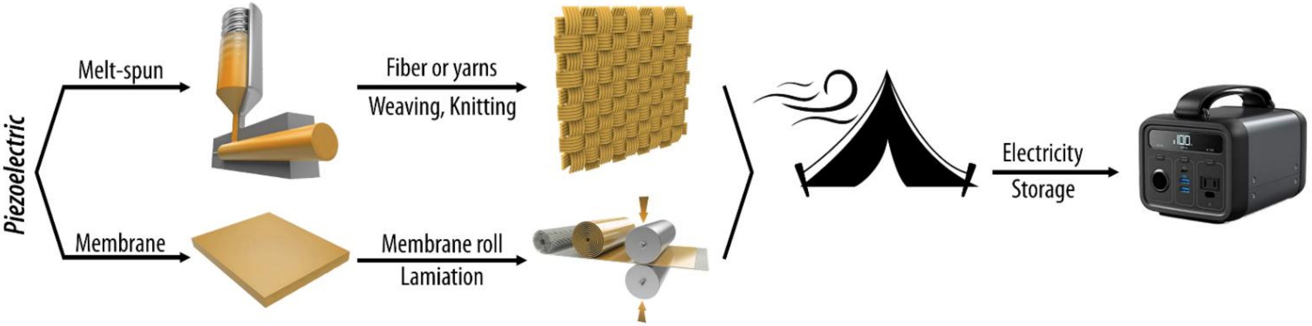

Figure 1. 1. Possible solutions by exploring piezoelectric fibers or membrane

Regarding conductive materials, the produced Joule heat by the electrical current could be a good resource for heating the tents. Compared to piezoelectric materials, applying conductive materials on textiles seems to be a more facilitated manufacturing process. Figure 1. 2 depicts the potential use of conductive materials in textiles for this project. Since conductive fibers used for textiles are typically expensive and heavy, a woven textile made only of conductive fibers cannot fulfill the cost and weight constraints for these tents. Therefore, a more suitable application of conductive fibers can be the use of a weaving pattern for these fibers in combination with another type of fiber that can take the structural role. In addition to conductive fiber, dip-coating and inkjet printing techniques can add conductivity to an already fabricated textile. In comparison to dip-coating, inkjet printing allows for more flexibility in textile design. By applying the conductive layer on one side of the textile, it is possible to create a product with differing indoor (heating) and outdoor (waterproof) properties. Although, mechanical and structural criteria are no longer a concern with these manufacturing processes;

delamination and electrical circuit discontinuity can raise some issues. Furthermore, a power generator at the refugee camp is a key requirement that must be considered.

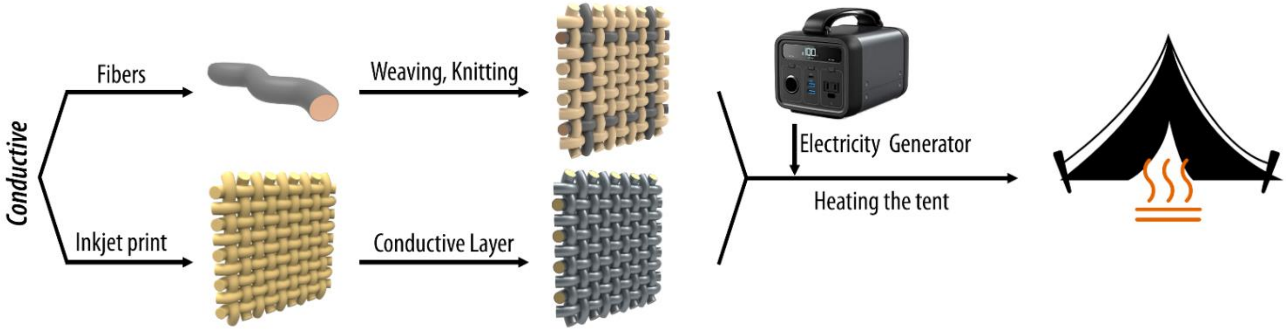

Figure 1. 2. Possible solutions using conductive fibers or coating

In terms of energy usage, a mix of conductive and piezoelectric materials is likely to be a more appropriate design in the context of emergency scenarios (Figure 1. 3). A conductive core surrounded by a piezoelectric substance and a protective sheath as the fibers or yarns of a woven textile can provide a closed-loop energy consumption, to a certain extent. The piezoelectric component of these fibers can generate energy from deformation caused by environmental conditions (rain, wind); this energy can then be stored in electrical storage, and the same electricity can be used to charge the conductive core of the fibers, thereby heating the tent via the Joule heat in the created textile. By including a wind sensor into the system, the product may also function in reverse, providing resistance and stiffness to the wind via the applied electrical charge.

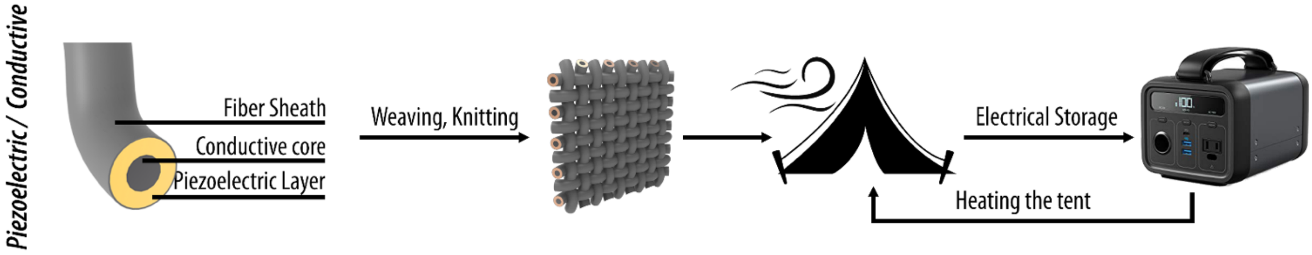

Figure 1. 3. Possible solutions combining piezoelectric and conductive materials for textile fiber

Finally, hygroscopic materials that are able to readily absorb moisture from the environment and deform as a result of the moisture absorption can provide some valuable aspects in the design of an environmentally-responsive smart textile. Although, humidity has only a minor impact on overall thermal comfort, but a significant impact on respiratory comfort, air quality, and perceived temperature [76]. Within the context of emergency shelter tents, the use of a hygroscopic material with adequate engineering may favor or reduce the exchange of air between the inside and the outside, providing humidity regulation and user comfort.

Recently, researchers have learned how to exploit the materials' sensitivity to external humidity to develop humidity-responsive self-actuators capable of controlling the indoor humidity level [25,27,46,51,73,74,77,78]. Since the rigidity of these materials may be compromised when relative humidity rises [69], they cannot be used as fibers of the structural textile in an emergency tent. But they can be applied on a textile that can meet the mechanical requirements for the tents. Vast majority of the recent development of exploiting hygroscopic materials employ a bi-layered composite of a hygroscopic material layer paired with a non-hygroscopic material layer and take advantage of the different dimensional variation caused by a change in the humidity of the atmosphere [25,27,53–62,45,63–72,46,73–75,47–52].

The non-hygroscopic layer can be also a composite product such as woven textiles with external coating used for tents. By applying a hygroscopic membrane on a prefabricated textile and applying suitable apertures in a bi-layered composite, different opening can be achieved based on the relative humidity (Figure 1. 4). Another application of hygroscopic materials for the aim of this project might be as a sheath for fibers with greater mechanical characteristics and the ability to meet the structural demands of the textile. In this situation, by adjusting the fiber count of the textile, it will be possible to create a textile that is breathable in a dry climate. As the hygroscopic sheath absorbs moisture from the environment (fog, rain, humid air), it expands and closes the porous between the warp and weft strands, rendering the textile waterproof.

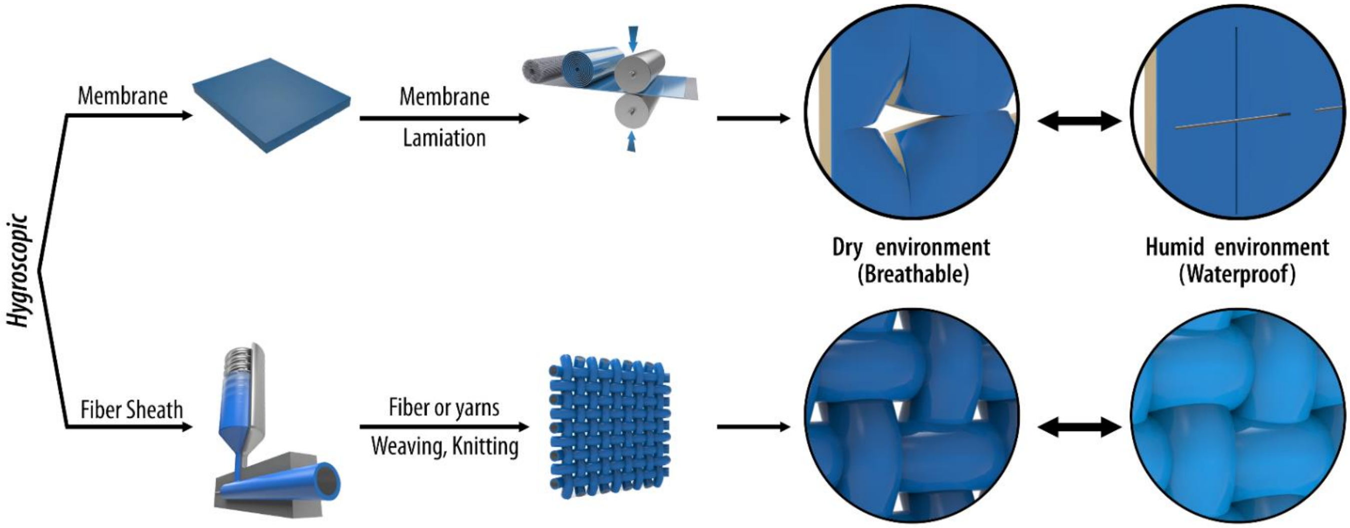

Figure 1. 4. Possible solutions exploiting hygroscopic materials as fiber sheath or membrane

1.3 Decision-making criteria and project's goal

The decision-making criterion for selecting the optimum solution from the above-mentioned concepts may be separated into two groups. One is the limits set by supporting organizations of NGOs for criteria such as cost, weight, and the structural properties of the textile. Another is connected to physical conditions and sources in the refugee camp, such as access to power and the availability of skilled and equipped technicians.

The key drawbacks of piezoelectric (Figure 1. 1) and conductive (Figure 1. 2) proposals are related to maintenance and cost-efficiency. Apart from the extra weight to be carried by the refugee, the additional cost for the manufacturer and the presence of an expert technician in the refugee camp to maintain the device are points of concern. Although the energy harvesting capability of piezoelectric materials combined with conductive materials can be a great advantage in emergency camps for heating purposes (Figure 1. 3), the concept does not appear feasible when viewed through the realistic lens of skilled technician availability and economic resources.

These criteria are not an issue for proposals that use hygroscopic materials. Hygroscopic polymers, which are primarily bio-based, are relatively cheap. Moreover, the proposed concepts' response to changes in the environment is derived from the intrinsic properties of the materials. This implies no maintenance or additional device is required for these solutions, placing them in the previously defined “very smart textile” category. What affects the selection of the best solution among the presented concepts for hygroscopic material application, instead, is related to the manufacturing process limitation. Considering that the turning point for utilizing hygroscopic materials as humidity-responsive self-actuators began about a decade ago, the technology of mass manufacturing for the use of these materials is not well explored. Pipetting, inkjet printing, and 3D printing are the methods explored to apply a hygroscopic layer to a non-hygroscopic substrate to create bi-layered self-actuators. To the best of the author's knowledge, no record of using a hygroscopic material as a fiber sheath and optimizing the fiber count for the concept shown in Figure 1. 4 has been published. Although the concept of woven textile using fibers with hygroscopic sheath is original and more effective, the manufacturing process for exploring this idea is not available. Moreover, the textile production for the emergency shelter tents is restricted to exclusive suppliers with predefined manufacturing process.

At this stage, the bi-layered composite consisting of the lamination of the hygroscopic membrane to a prefabricated textile that already satisfies the mechanical and economic criteria appears to be the most realistic concept among all the provided options. Taking into consideration all the production and manufacturing process limits for these suppliers the application of hygroscopic membrane on the textiles used for the emergency tents must sit within their production line. This suggests that a hygroscopic material can be used as a coating throughout the manufacturing process of these textiles without disrupting the production line.

Therefore, this thesis aims to provide a model that can describe the hygroscopic behavior to be used as the designing tool for the manufacturing process toward the optimization of humidity-responsive bi-layered self-actuator using these textiles. The ideal strategy to reach the aim of this project is:

- providing a systematic process to produce membranes of a hygroscopic material (Cellulose Acetate)
- identifying and characterizing the intrinsic properties of these membranes involved in the hygroscopic behavior of this material
- developing a detailed finite element model that can employ the characterized intrinsic properties of the hygroscopic membrane to predict the response of a bi-layered self-actuator to relative humidity variations

The experimental procedure and the numerical model provided for achieving the described aim will be the design guidelines for the fine tuning of the performance of the manufactured products.

References

1. Tuloup C, Harizi W, Aboura Z, Meyer Y, Khellil K, Lachat R. On the use of in-situ piezoelectric sensors for the manufacturing and structural health monitoring of polymer-matrix composites: A literature review. *Compos Struct*. 2019;215:127-149. doi:10.1016/j.compstruct.2019.02.046

2. Chen S, Liu S, Wang P, Liu H, Liu L. Highly stretchable fiber-shaped e-textiles for strain/pressure sensing, full-range human motions detection, health monitoring, and 2D force mapping. *J Mater Sci*. 2018;53(4):2995-3005. doi:10.1007/s10853-017-1644-y

3. Liu L, Su D, Tang Y, Fang G. Thermal conductivity enhancement of phase change materials for thermal energy storage: A review. *Renew Sustain Energy Rev*. 2016;62:305-317. doi:10.1016/j.rser.2016.04.057

4. Sze JY, Mu C, Romagnoli A, Li Y. Non-eutectic Phase Change Materials for Cold Thermal Energy Storage. *Energy Procedia*. 2017;143:656-661. doi:10.1016/j.egypro.2017.12.742

5. Huang X, Alva G, Jia Y, Fang G. Morphological characterization and applications of phase change materials in thermal energy storage: A review. *Renew Sustain Energy Rev*. 2017;72(April 2016):128-145. doi:10.1016/j.rser.2017.01.048

6. Pereira da Cunha J, Eames P. Thermal energy storage for low and medium temperature applications using phase change materials – A review. *Appl Energy*. 2016;177:227-238. doi:10.1016/j.apenergy.2016.05.097

7. Farid MM, Khudhair AM, Razack SAK, Al-Hallaj S. A review on phase change energy storage: materials and applications. *Energy Convers Manag*. 2004;45(9-10):1597-1615. doi:10.1016/j.enconman.2003.09.015

8. Liu M, Saman W, Bruno F. Review on storage materials and thermal performance enhancement techniques for high temperature phase change thermal storage systems. *Renew Sustain Energy Rev*. 2012;16(4):2118-2132. doi:10.1016/j.rser.2012.01.020

9. Veerakumar C, Sreekumar A. Phase change material based cold thermal energy storage: Materials, techniques and applications – A review. *Int J Refrig*. 2016;67:271-289. doi:10.1016/j.ijrefrig.2015.12.005

10. Zhai XQ, Wang XL, Wang T, Wang RZ. A review on phase change cold storage in air-conditioning system: Materials and applications. *Renew Sustain Energy Rev*. 2013;22:108-120. doi:10.1016/j.rser.2013.02.013

11. de Gracia A, Cabeza LF. Phase change materials and thermal energy storage for buildings. *Energy Build*. 2015;103:414-419. doi:10.1016/j.enbuild.2015.06.007

12. Agyenim F, Hewitt N, Eames P, Smyth M. A review of materials, heat transfer and phase change problem formulation for latent heat thermal energy storage systems (LHTESS). *Renew Sustain Energy Rev*. 2010;14(2):615-628. doi:10.1016/j.rser.2009.10.015

13. Sánchez-Romate XF, Artigas J, Jiménez-Suárez A, Sánchez M, Güemes A, Ureña A. Critical parameters of carbon nanotube reinforced composites for structural health monitoring applications: Empirical results versus theoretical predictions. *Compos Sci Technol*. 2019;171(2019):44-53. doi:10.1016/j.compscitech.2018.12.010

14. Pielichowska K, Pielichowski K. Phase change materials for thermal energy storage. *Prog Mater Sci*. 2014;65:67-123. doi:10.1016/j.pmatsci.2014.03.005

15. TQ T, NE L. Flexible and Stretchable Physical Sensor Integrated Platforms for Wearable Human-Activity Monitoringand Personal Healthcare. *Adv Mater*. 2016;28(22):4338-4372. doi:10.1002/ADMA.201504244

16. Yan T, Wang Z, Pan Z-J. A highly sensitive strain sensor based on a carbonized polyacrylonitrile nanofiber woven fabric. *J Mater Sci*. 2018;53(16):11917-11931. doi:10.1007/s10853-018-2432-z

17. Ratna D, Karger-Kocsis J. Recent advances in shape memory polymers and composites: a review. *J Mater Sci*. 2008;43(1):254-269. doi:10.1007/s10853-007-2176-7

18. Zarma IH, Hassan H, Ookawara S, Ahmed M. Thermal Energy Storage in Phase Change Materials:-Applications, Advantages and Disadvantages. *Icceee 2017*. 2017;(November):0-11.

19. Oró E, de Gracia A, Castell A, Farid MM, Cabeza LF. Review on phase change materials (PCMs) for cold thermal energy storage applications. *Appl Energy*. 2012;99:513-533. doi:10.1016/j.apenergy.2012.03.058

20. Fredi G, Dorigato A, Pegoretti A. Multifunctional glass fiber/polyamide composites with thermal energy storage/release capability. *Express Polym Lett*. 2018;12(4):349-364. doi:10.3144/expresspolymlett.2018.30

21. Tay NHS, Liu M, Belusko M, Bruno F. Review on transportable phase change material in thermal energy storage systems. *Renew Sustain Energy Rev*. 2017;75(October 2016):264-277. doi:10.1016/j.rser.2016.10.069

22. Lund A, Rundqvist K, Nilsson E, Yu L, Hagström B, Müller C. Energy harvesting textiles for a rainy day: woven piezoelectrics based on melt-spun PVDF microfibres with a conducting core. *npj Flex Electron*. 2018;2(1):9. doi:10.1038/s41528-018-0022-4

23. Schäl P, Juhász Junger I, Grimmelsmann N, Ehrmann A. Development of graphite-based conductive textile coatings. *J Coatings Technol Res*. 2018;15(4):875-883. doi:10.1007/s11998-017-0024-5

24. Ritter A. Smart coatings for textiles in architecture. *Act Coatings Smart Text*. Published online 2016:429-453. doi:10.1016/B978-0-08-100263-6.00018-6

25. Taccola S, Greco F, Sinibaldi E, Mondini A, Mazzolai B, Mattoli V. Toward a New Generation of Electrically Controllable Hygromorphic Soft Actuators. *Adv Mater*. 2015;27(10):1668-1675. doi:10.1002/adma.201404772

26. Mondal S. Phase change materials for smart textiles – An overview. *Appl Therm Eng*. 2008;28(11-12):1536-1550. doi:10.1016/j.applthermaleng.2007.08.009

27. Wang W, Yao L, Cheng C-Y, et al. Harnessing the hygroscopic and biofluorescent behaviors of genetically tractable microbial cells to design biohybrid wearables. *Sci Adv*. 2017;3(5):e1601984. doi:10.1126/sciadv.1601984

28. Li X, Hu H, Hua T, Xu B, Jiang S. Wearable strain sensing textile based on one-dimensional stretchable and weavable yarn sensors. *Nano Res*. 2018;11(11):5799-5811. doi:10.1007/s12274-018-2043-7

29. Jian M, Wang C, Wang Q, et al. Advanced carbon materials for flexible and wearable sensors. *Sci China Mater*. 2017;60(11):1026-1062. doi:10.1007/s40843-017-9077-x

30. Stoppa M, Chiolerio A. Wearable electronics and smart textiles: A critical review. *Sensors (Switzerland)*. 2014;14(7):11957-11992. doi:10.3390/s140711957

31. Nilsson E, Mateu L, Spies P, Hagström B. Energy Harvesting from Piezoelectric Textile Fibers. *Procedia Eng*. 2014;87:1569-1572. doi:10.1016/J.PROENG.2014.11.600

32. Navneet Soin, H. Shah T, C. Anand S, et al. Novel "3-D spacer" all fibre piezoelectric textiles for energy harvesting applications. *Energy Environ Sci*. 2014;7(5):1670-1679. doi:10.1039/C3EE43987A

33. Jean-Mistral C, Basrour S, Chaillout JJ. Comparison of electroactive polymers for energy scavenging applications. *Smart Mater Struct*. 2010;19(8):085012. doi:10.1088/0964-1726/19/8/085012

34. Matsouka D, Vassiliadis S. Piezoelectric Melt-Spun Textile Fibers: Technological Overview. In: *Piezoelectricity - Organic and Inorganic Materials and Applications*. InTech; 2018. doi:10.5772/intechopen.78389

35. Kim H, Kim SM, Son H, et al. Enhancement of piezoelectricity via electrostatic effects on a textile platform. *Energy Environ Sci*. 2012;5(10):8932-8936.

36. Chen J, Li H, Yu Q, et al. Strain sensing behaviors of stretchable conductive polymer composites loaded with different dimensional conductive fillers. *Compos Sci Technol*. 2018;168:388-396. doi:10.1016/j.compscitech.2018.10.025

37. Ma M, Guo L, Anderson DG, Langer R. Bio-Inspired Polymer Composite Actuator and Generator Driven by Water Gradients. *Science (80-)*. 2013;339(6116):186-189. doi:10.1126/science.1230262

38. Buenger D, Topuz F, Groll J. Hydrogels in sensing applications. *Prog Polym Sci*. 2012;37(12):1678-1719. doi:10.1016/j.progpolymsci.2012.09.001

39. Aly K, Bradford PD. Real-time impact damage sensing and localization in composites through embedded aligned carbon nanotube sheets. *Compos Part B Eng*. 2019;162:522-531. doi:10.1016/j.compositesb.2018.12.104

40. Ke K, McMaster M, Christopherson W, Singer KD, Manas-Zloczower I. Highly sensitive capacitive pressure sensors based on elastomer composites with carbon filler hybrids. *Compos Part A Appl Sci Manuf*. 2019;126:105614. doi:10.1016/j.compositesa.2019.105614

41. Gong S, Ni H, Jiang L, Cheng Q. Learning from nature: constructing high performance graphene-based nanocomposites. *Mater Today*. 2017;20(4):210-219. doi:10.1016/j.mattod.2016.11.002

42. Khair N, Islam R, Shahariar H. Carbon-based electronic textiles: materials, fabrication processes and applications. *J Mater Sci*. 2019;54(14):10079-10101. doi:10.1007/s10853-019-03464-1

43. Gong X, Liu L, Liu Y, Leng J. An electrical-heating and self-sensing shape memory polymer composite incorporated with carbon fiber felt. *Smart Mater Struct*. 2016;25(3):35036. doi:10.1088/0964-1726/25/3/035036

44. Chung DDL. A review of multifunctional polymer-matrix structural composites. *Compos Part B Eng*. 2019;160:644-660. doi:10.1016/j.compositesb.2018.12.117

45. Wood D, Vailati C, Menges A, Rüggeberg M. Hygroscopically actuated wood elements for weather responsive and self-forming building parts – Facilitating upscaling and complex shape changes. *Constr Build Mater*. 2018;165:782-791. doi:10.1016/j.conbuildmat.2017.12.134

46. Reichert S, Menges A, Correa D. Meteorosensitive architecture: Biomimetic building skins based on materially embedded and hygroscopically enabled responsiveness. *Comput Des*. 2015;60:50-69. doi:10.1016/j.cad.2014.02.010

47. Grönquist P, Wittel FK, Rüggeberg M. Modeling and design of thin bending wooden bilayers. Johnson C, ed. *PLoS One*. 2018;13(10):e0205607. doi:10.1371/journal.pone.0205607

48. Menges A, Reichert S. Performative Wood: Physically Programming the Responsive Architecture of the HygroScope and HygroSkin Projects. *Archit Des*. 2015;85(5):66-73. doi:10.1002/ad.1956

49. Simonson CJ, Olutimayin S, Salonvaara M, Ojanen T, O'Connor J. Potential for hygroscopic building materials to improve indoor comfort and air quality in the canadian climate. *Therm Perform Exter Envel Whole Build*. Published online 2004.

50. Xie H, Gong G, Wu Y, Liu Y, Wang Y. Research on the Hygroscopicity of a Composite Hygroscopic Material and its Influence on Indoor Thermal and Humidity Environment. *Appl Sci*. 2018;8(3):430. doi:10.3390/app8030430

51. Holstov A, Farmer G, Bridgens B. Sustainable materialisation of responsive architecture. *Sustain*. 2017;9(3). doi:10.3390/su9030435

52. Holstov A, Morris P, Farmer G, Bridgens B. Towards Sustainable Adaptive Building Skins with Embedded Hygromorphic Responsiveness. In: *Proceedings of the International Conference on Building Envelope Design and Technology - Advanced Building Skins*. ; 2015:57-67. https://www.researchgate.net/publication/278901137_Towards_sustainable_adaptive_building_skins_with_embedded_hygromorphic_responsiveness

53. Correa D, Papadopoulou A, Guberan C, et al. 3D-Printed Wood: Programming Hygroscopic Material Transformations. *3D Print Addit Manuf*. 2015;2(3):106-116. doi:10.1089/3dp.2015.0022

54. Rivadeneyra A, Marín-Sánchez A, Wicklein B, et al. Cellulose nanofibers as substrate for flexible and biodegradable moisture sensors. *Compos Sci Technol*. 2021;208:108738. doi:10.1016/j.compscitech.2021.108738

55. Yao L, Ou J, Cheng C-Y, et al. bioLogic:Natto Cells as Nanoactuators for Shape Changing Interfaces. In: *Proceedings of the 33rd Annual ACM Conference on Human Factors in Computing Systems*. Vol 2015-April. ACM; 2015:1-10. doi:10.1145/2702123.2702611

56. Zhu P, Liu Y, Fang Z, et al. Flexible and Highly Sensitive Humidity Sensor Based on Cellulose Nanofibers and Carbon Nanotube Composite Film. *Langmuir*. 2019;35(14):4834-4842. doi:10.1021/ACS.LANGMUIR.8B04259/SUPPL_FILE/LA8B04259_SI_001.PDF

57. Wang Y, Zhang L, Zhou J, Lu A. Flexible and Transparent Cellulose-Based Ionic Film as a Humidity Sensor. *ACS Appl Mater Interfaces*. 2020;12(6):7631-7638. doi:10.1021/acsami.9b22754

58. González del Campo MM, Darder M, Aranda P, et al. Functional Hybrid Nanopaper by Assembling Nanofibers of Cellulose and Sepiolite. *Adv Funct Mater*. 2018;28(27):1703048. doi:10.1002/ADFM.201703048

59. Castaldo R, Lama GC, Aprea P, et al. Humidity-Driven Mechanical and Electrical Response of Graphene/Cloisite Hybrid Films. *Adv Funct Mater*. 2019;29(14):1807744. doi:10.1002/adfm.201807744

60. Okuzaki H, Kuwabara T, Funasaka K, Saido T. Humidity-Sensitive Polypyrrole Films for Electro-Active Polymer Actuators. *Adv Funct Mater*. 2013;23(36):4400-4407. doi:10.1002/adfm.201203883

61. Wang DH, McKenzie RN, Buskohl PR, Vaia RA, Tan L-S. Hygromorphic Polymers: Synthesis, Retro-Michael Reaction, and Humidity-Driven Actuation of Ester–Sulfonyl Polyimides and Thermally Derived Copolyimides. *Macromolecules*. 2016;49(9):3286-3299. doi:10.1021/acs.macromol.6b00250

62. Shrestha S, Diaz JA, Ghanbari S, Youngblood JP. Hygroscopic Swelling Determination of Cellulose Nanocrystal (CNC) Films by Polarized Light Microscopy Digital Image Correlation. *Biomacromolecules*. 2017;18(5):1482-1490. doi:10.1021/acs.biomac.7b00026

63. Ochoa M, Chitnis G, Ziaie B. Laser-micromachined cellulose acetate adhesive tape as a low-cost smart material. *J Polym Sci Part B Polym Phys*. 2013;51(17):1263-1267. doi:10.1002/polb.23337

64. Weng M, Zhou P, Chen L, et al. Multiresponsive Bidirectional Bending Actuators Fabricated by a Pencil-on-Paper Method. *Adv Funct Mater*. 2016;26(40):7244-7253. doi:10.1002/adfm.201602772

65. Greco F, Zucca A, Taccola S, et al. Ultra-thin conductive free-standing PEDOT/PSS nanofilms. *Soft Matter*. 2011;7(22):10642. doi:10.1039/c1sm06174g

66. Bridgens B, Holstov A, Farmer G. Architectural application of wood-based responsive building skins. In: *In Proceedings of the 12th International Conference on Advanced Building Skins*. ; 2017:2-3. https://www.researchgate.net/publication/320244562%0AArchitectural

67. Heibeck F, Tome B, Della Silva C, Ishii H. uniMorph:Fabricating Thin-Film Composites for Shape-Changing Interfaces. In: *Proceedings of the 28th Annual ACM Symposium on User Interface Software & Technology*. ACM; 2015:233-242. doi:10.1145/2807442.2807472

68. Syrový T, Maronová S, Kuberský P, et al. Wide range humidity sensors printed on biocomposite films of cellulose nanofibril and poly(ethylene glycol). *J Appl Polym Sci*. 2019;136(36):47920. doi:10.1002/app.47920

69. Dingler C, Müller H, Wieland M, Fauser D, Steeb H, Ludwigs S. From Understanding Mechanical Behavior to Curvature Prediction of Humidity-Triggered Bilayer Actuators. *Adv Mater*. 2021;33(9). doi:10.1002/ADMA.202007982

70. Ramirez-figueroa C, Hernan L, Guyet A, Dade-robertson M. Bacterial Hygromorphs: Experiments into the integration of soft technologies into building skins. In: *ACADIA 2016 - Posthuman Frontiers*. Association for Computer Aided Design in Architecture; 2016:244-253. http://2016.acadia.org

71. Vazquez E, Gürsoy B, Duarte JP. Formalizing shape-change: Three-dimensional printed shapes and hygroscopic material transformations. *Int J Archit Comput*. 2019;18(1):67-83. doi:10.1177/1478077119895216

72. Abdelmohsen S. HMTM : Hygromorphic-Thermobimetal Composites as a Novel Approach to Enhance Passive Actuation of Adaptive Façades. *18th CAAD Futur 2019 Int Conf*. 2019;(June). Accessed December 14, 2021. https://www.researchgate.net/publication/332604413_HMTM_Hygromorphic-Thermobimetal_Composites_as_a_Novel_Approach_to_Enhance_Passive_Actuation_of_Adaptive_Facades

73. Holstov A, Bridgens B, Farmer G. Hygromorphic materials for sustainable responsive architecture. *Constr Build Mater*. 2015;98:570-582. doi:10.1016/j.conbuildmat.2015.08.136

74. Reyssat E, Mahadevan L. Hygromorphs: from pine cones to biomimetic bilayers. *J R Soc Interface*. 2009;6(39):951-957. doi:10.1098/rsif.2009.0184

75. Abdelmohsen S, Adriaenssens S, Gabriele S, Olivieri L, El-Dabaa R. Hygroscapes: Innovative shape shifting façades. In: *Lecture Notes in Civil Engineering*. Vol 24. Springer, Cham; 2019:675-702. doi:10.1007/978-3-030-03676-8_26

76. ASHRAE. *Handbook of Fundamentals, SI Edition*. SI. (Kennedy HE, Owen MS, eds.). ASHRAE; 2017.

77. Alexander SLM, Korley LTJ. Tunable hygromorphism: structural implications of low molecular weight gels and electrospun nanofibers in bilayer composites. *Soft Matter*. 2017;13(1):283-291. doi:10.1039/C6SM00749J

78. Burgert I, Fratzl P. Actuation systems in plants as prototypes for bioinspired devices. *Philos Trans R Soc A Math Phys Eng Sci*. 2009;367(1893):1541-1557. doi:10.1098/rsta.2009.0003

2 Hygroscopic Materials: Applications and Characterization

In this chapter, theoretical background on hygroscopic materials response to changes in the environment relative humidity and the related material properties are introduced. An overview of recent attempts for exploiting this behavior for the production of self-actuators is presented. Different categories of hygroscopic materials will be described. The main fields of application and production processes and technologies will be briefly presented. Experimental characterization techniques will be summarized and compared. The main modeling approaches adopted in the last decade for the description of this behavior will be reviewed. At last, but not least, the framework for experimental characterization and numerical modeling for the conduction of this research will be presented.

2.1 Introduction

Hygroscopicity refers to a material capability to attract and hold water molecules from the surrounding environment. This phenomenon occurs in polymeric materials whose chemical structure contains polar groups like "OH" or "COO^-" functional groups and can cause their deformation [1]. In this context, cellulose-based materials are one of the most well-known categories of materials for their hygroscopic expansion tendency.

Figure 2. 1 depicts, as an example, a schematic representation of cellulose molecules before and after interaction with water molecules. As shown, in the absence of water molecules, the hydrogen and oxygen of each hydroxyl group of cellulose can form a hydrogen bond with the surrounding oxygen and hydrogen, respectively. When the material is exposed to a higher level of relative humidity, the presence of water molecules, the intermolecular interaction, and the previously described hydrogen bond are all disturbed. Water molecules' small size enhances their diffusivity through cellulose chains and the establishment of new hydrogen bonds with cellulose's hydroxyl groups [1]. This mechanism causes cellulose chains to take distance from each other, which leads to the expansion of the material on a mesoscopic scale.

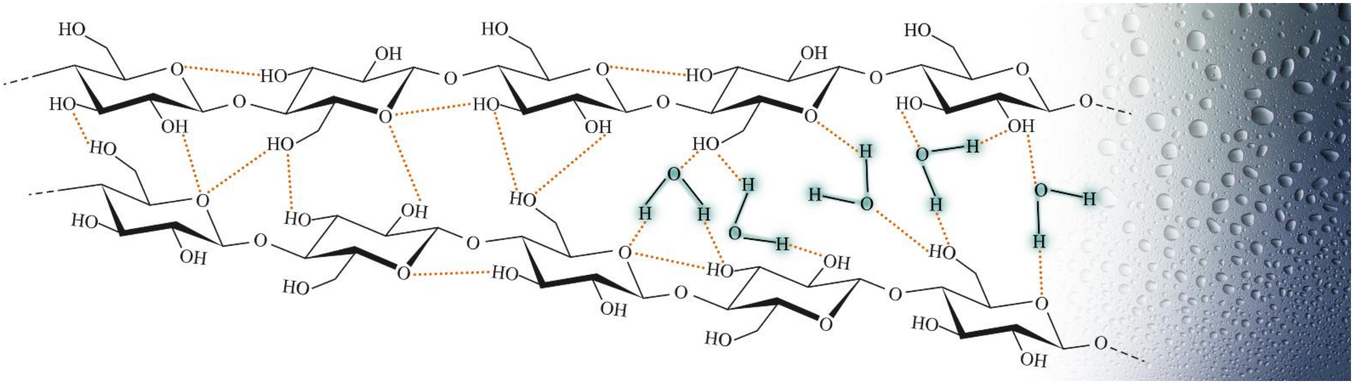

Figure 2. 1. Hygroscopic behavior of cellulose in presence of water molecules

Considering a product made of an isotropic hygroscopic material , depending on its geometry (1D, 2D or 3D), this induced expansion will manifest as a linear, planar, or volumetric expansion, as shown in Figure 2. 2 (a). The vast majority of recent attempts to take advantage of materials' hygroscopic behavior have focused on using these materials as an active layer in a bilayer composite, exploiting linear or planar expansion [2–34]. Using a bi-layered composite made of a thin layer of a hygroscopic material and a layer of a non-hygroscopic or less hygroscopic one, these investigations employed the difference in dimensional variation caused by changes in humidity in the environment. A change in the humidity level of the environment produces a large change in the length of the hygroscopic material thin layer (active layer), but the substrate (passive layer) deforms less (Figure 2. 2 (b)). If the active layer is constrained on one side to the passive layer, the mismatch of deformation causes the bi-layered composite to bend. This "deformational" behavior is similar to that occurring in bi-metallic strips under heating described by Timoshenko's [35] model based on Stoney's [36] work on stresses generated in metallic films. Similarly, the moisture-induced deformation in a bilayer composite may be described using Timoshenko's bi-metal strip bending theory, as demonstrated by Berry and Pritchet [37]. Details on these theories will be reported in Section 2.6.

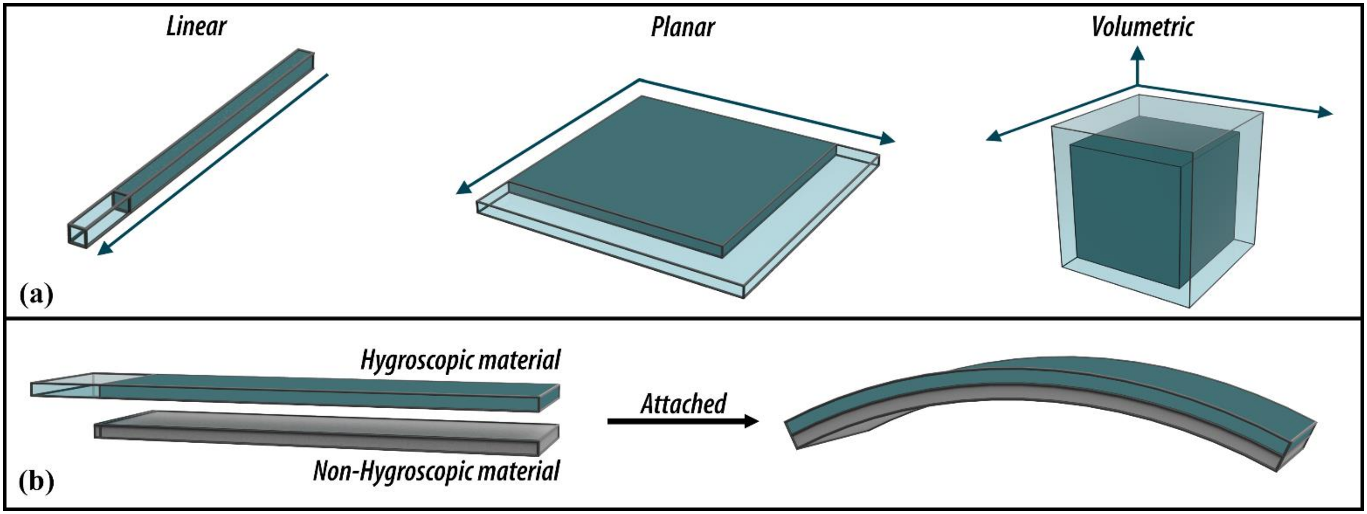

Figure 2. 2. (a) Schematic representation for the geometrical deformation of an isotropic hygroscopic material based 1D, 2D or 3D product, (b) Schematic representation of humidity-induced bending of a bi-layered composite

2.2 Progress in exploiting hygroscopic materials

For more than half a century, the hygroscopic behavior of a material was regarded as a defect in products made of such a material. The performance of epoxy molding compounds in microelectronics [38] or timber structures in building constructions [39] are significantly affected by moisture over time. Since the early 2000s, researchers began to take advantage of this behavior for the purpose of design and manufacturing products that have the ability to respond to external stimuli in an autonomous manner. Looking at this behavior through a new lens led to the manufacturing of products ranging from the large scale of environmentally responsive building façades [2–9,14,25,29–34] to the medium scale of environmentally responsive wearables [10,11] and the small scale of humidity-responsive self-actuators [12,13,15–24,26–28]. Figure 2. 3 shows the number of peer-reviewed publications in the field of building construction and sensors from the turning page for the exploiting of hygroscopic materials (2009) till 2021, with a significant change since 2015, which highlights the novelty of this topic.

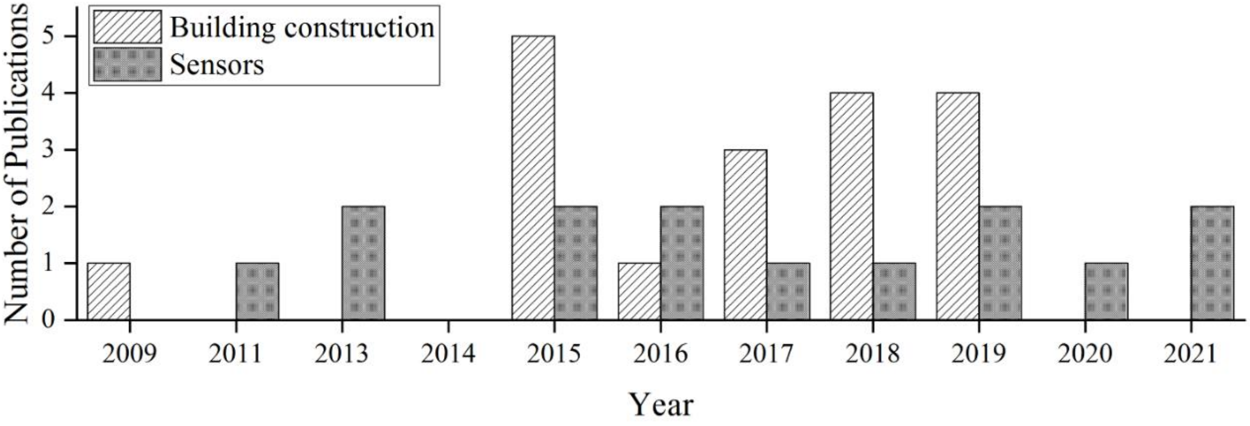

Figure 2. 3. Number of publications in the area building construction and sensor exploiting the hygroscopic behavior of materials

In these researches, a variety of organic materials such as wood [2–9,14,25,29–34], cellulose-based materials [12,13,15,16,20,21,40,41], superabsorbent hydrogels [16,42,43], conjugated polymers [12,23,24,28,44] has been explored; even bacteria [3,45,46] and microbial cells [10,11] have been used to design bio-hybrid wearables. Different manufacturing technologies have been utilized or even built from scratch for the fabrication of prototypes of the designed products. Various characterization techniques and modeling strategies for the description of moisture induced deformation have been investigated. The materials, manufacturing technologies, experimental procedures, descriptive or numerical models adopted in the areas of building construction and sensor development are summarized in Table 2. 1 and Table 2. 2 , respectively.

From a first glance at Table 2. 1, it can be noticed that wood, due to the existence of cellulose in natural fibers, is the predominant employed hygroscopic material in the field of building construction. In these investigations, a wood veneer or a layer of wood fibers was used with a non-hygroscopic material or with a less hygroscopic wood. Although different materials such as polyimide, aluminum, and CFRP were employed as passive substrates for these researches, a significant portion of these investigations concentrated on coupling two types of wood as bilayer self-actuators. The production technology utilized for layer coupling is separated into two basic approaches: employing adhesive tape or glue and 3D printing a low or non-hygroscopic material on wood veneer, or vice versa, 3D printing of a wood fiber containing polymer on a low or non-hygroscopic film. The experimental procedures for the characterization of these products limited to image analysis and the measured bending curvature of the bi-layered was compared to the bending cantilever analytical predictive model presented by Berry and Pritchet [37]. Only a few of these studies characterized the evolution of bending curvature as a function of time [7,30,48]. Holstov et al. [7] studied the reaction of a bilayer (consisting of 1 mm rotary-cut silver birch, Betula pendula, as active layers and 0.2 mm stiff laminated epoxy-glass passive layers) coupled with different methods to cyclic changes in the humidity level of the environment. Despite several errors in the experimental setup and process, the comparison of the overall curvature of bilayers demonstrated the predicted pattern by the variation of humidity level. For specimens submerged in water, RH = 41 %, submerged in water for the second time, and RH = 39 %, values of curvature around 48, -20, 52, and -21 (m^{-1}) were reported, respectively.

In the field of sensors, however, different types of hygroscopic materials, varying from cellulose-based materials and electrically conductive conjugated polymers to composites based on these materials have been used. Furthermore, different production technologies and experimental techniques for characterization of the materials' behavior were adopted (Table 2. 2). In contrast to the building construction sector, which is primarily focused on analytical and numerical modeling for the description of behavior at the macroscopic scale, the focus in sensors development is on the production process and characterization of material properties at the microscopic scale.

Table 2. 1. Details of publications in building construction area exploring hygroscopic materials

Year	Material	Production technology	Experimental techniques	Descriptive model	Ref.
2009	Paper	Adhesive	Image Analysis	Bending cantilever	30
2015	wood grain	Multi-material 3D printing	Image Analysis	Bending cantilever	9
2015	Silver Birch wood	3D Printing	Image Analysis	Bending cantilever	29
2015	Beech wood		Image Analysis	FEM (ANSYS)	33
2015	Beech wood				4
2016	Bacillus	Pipetting			3
2017	Spruce	Adhesive	Image Analysis		47
2017	Silver Birch wood	3D Printing			2
2017	Silver Birch wood	3D Printing			7
2018	Beech wood	Adhesive	Image Analysis / Flex sensor	Grasshopper/ firefly	48
2018	wood			Bending cantilever	32
2018	Beech wood	Adhesive	Image Analysis	Built-in code	34
2018	Wood fiber	Mixing	Indoor air quality control		6
2019	Beech wood	Adhesive		FEM (COMSOL)	49
2019	Beech wood	3D Printing			14
2019	Beech wood	Adhesive	Image Analysis	Bending cantilever	25
2019	Beech wood		Image Analysis		31

Table 2. 2. Details of publications in sensors development area exploring hygroscopic materials

Year	Material	Production technology	Experimental techniques	Descriptive model	Ref.
2011	PEDOT:PSS *	Spin coating	Atomic Force Microscopy		24
2013	Polypyrrole	Dispersion	Quartz Crystal Microbalance		18
2013	Cellulose acetate	off-the-shelf			21
2015	PEDOT:PSS	Spin coating		Bending cantilever	23
2015	UHMW PE **	Inkjet printing			26
2016	Polyimide				19
2016	Paper				22
2017	cellulose nanocrystal	Dispersion	Dynamic vapor sorption, Digital Image Correlation (DIC)	FEM (Abaqus)	20
2018	CNF ***		Thermogravimetric Analysis		16
2019	CNF	Dispersion			13
2019	Cloisite	Dispersion			17
2019	CNF	Screen printing	Atomic Force Microscopy		27
2020	Cellulose	Dispersion			15
2021	CNF	Screen printing	Atomic Force Microscopy		12
2021	PEDOT:PSS	Spin coating	Image correlation Quartz Crystal Microbalance	Bending cantilever	28

* PEDOT= Poly(3,4-ethylenedioxythiophene, PSS=Poly(styrene sulfonate), ** UHMW PE= Ultra-High Molecular Weight Polyethylene, *** CNF= Cellulose NanoFibers,

2.3 Hygroscopic materials

Although a vast range of materials, have been investigated for exploiting hygroscopic behavior. in this thesis three major groups will be considered: wood, cellulose-based materials and synthetic polymeric materials.

- ***Wood*** is the hygroscopic material predominantly used in the building construction sector for the production of humidity-responsive façades. For centuries, building engineers have overcome the challenges of wood bending, curling, and custom forming through the labor-intensive and complex techniques of steam bending and lamination [9]. In 2011, Achim Menges' project "HygroSkin: Meteorosensitive Pavilion [50]," co-created with Oliver David Krieg and Steffen Reichert, exhibited for the first time a novel use of wood in kinetic architecture (Figure 2. 4).

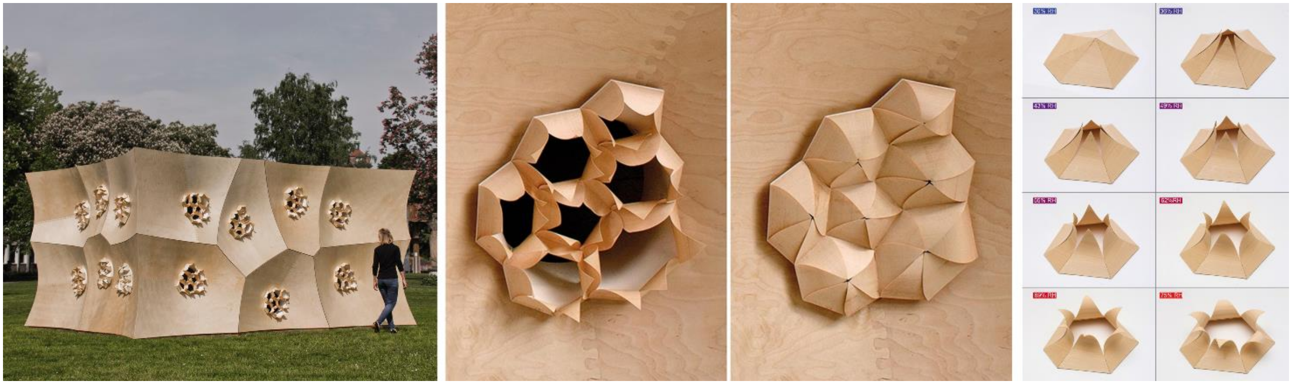

Figure 2. 4. HygroSkin: Meteorosensitive Pavilion, 2013, Achim Menges, Permanent Collection, FRAC Centre Orleans [50]

Cellulose, the primary substance of all plants, is responsible for the wood's sensitivity to variations in the humidity levels of the environment. Nevertheless, the reaction of wood is strongly dependent on the type of wood and the direction of its grain [48]. In this context, woods can be classified in two categories of hardwoods and softwoods with different intrinsic properties dictating whether they should be used as an active or passive layer in laminated hygroscopic wooden systems. Hardwoods are porous, with open-ended wood cells or pores. Therefore, water molecules can be absorbed and move through the pore walls, causing the wood to expand significantly. Softwoods, on the other hand, lack pores, and water sorption or flow occurs in tiny tracheids that have a lower tendency to volume variations than hardwood structures. Hardwoods are thus suitable as the active layer in bi-layer laminates, while softwoods may be used for the passive layer [51]. Therefore, beech [4,14,25,31,33,34,48,49], silver birch [2,7,29] and spruce [47] are the hardwoods used as the active layer and maple [4,33] and fir [48,49] are the ones used as the passive layer in building construction area.

Another characteristic that influences wood hygroscopic behavior is the grain orientation [8,25,29,48]. According to Abdelmohsen's research [25,48], the degree of bending, twisting, deflection, as well as reaction speed to an external stimulus, are highly dependent on both grain orientation and wood layer thickness. This dependence is due to wood orthotropic structure and to difference in the moisture diffusion coefficient of wood in different directions. The diffusion coefficient is the only characteristic that effects the moisture absorption process through the thickness and to the ultimate moisture concentration, and hence the response speed. Obviously, the thicker the layer, the longer it takes to attain saturation. As a result, the hygroscopic behavior of wood varies in the axial, radial, and circumferential directions. The hygroscopic behavior in these directions is also affected by whether the veneer was extracted from earlywood or latewood, heartwood or sapwood. Wood cell walls do not expand along their length in the axial direction, hence they have a very low hygroscopic expansion in this direction. According to Holstov et al. [7], the hygroscopic expansion is almost 0.1 % in the axial direction and about 4–7% in the radial direction, depending on the wood specie. Along the circumferential direction, due to the expansion of the wall cells along their thickness and radius, the highest values of hygroscopic expansion have been observed (8-12%).

- ***Cellulose-based materials*** in forms of Cellulose Nanofibers (CNF) [12,13,15,16,27] or cellulose Nanocrystals [20], as well as cellulose derivatives like cellulose acetate [21], have been studied for the production of humidity sensors or automated engines throughout the last decade. Rivadeneyra et al. [12] developed a transparent and biodegradable moisture sensor based on cellulose nanofibers/ PEDOT:PSS electrode that operates over a wide range of relative humidity (RH) from 20 to 85%. The sensing layer is made of CNF film, which does not require any additional processing to function as a sensor. Zhu et al. [13] presented a flexible cellulose nanofiber/carbon nanotube humidity sensor which showed a linear expansion of 69% for a relative humidity variation from 11 to 95%. Wang et al. [15] reported a transparent and flexible cellulose/KOH composite ionic film (CKF) as a humidity sensor for skin moisture and breath detection with the same value of hygroscopic expansion with a humidity range of 11 to 97%. A cellulose nanofibril film was employed as a substrate for screen-printing carbon electrodes by Syrovy et al.[27] The effect of plasticizers (40% PEG) on the cellulosic substrate was investigated in this study. The plasticizer had an effect on sensor external stimulus reaction kinetics. While the biocomposite film sensors had a slightly longer reaction time, the recovery time of plasticized sensors was two times faster than that of sensors that did not include PEG. An off-the-shelf cellulose acetate adhesive tape was employed as a humidity-responsive material for the fabrication of automatic underwater grip [21].

- ❖ ***Synthesized polymers*** such as (PEDOT) [23,24,28] and polypyrrole (PPy) [18] have been used in this area: they have a proclivity to absorb moisture from their surroundings, but moisture desorption and regaining the initial shape does not occur easily. Thus, researchers primarily take advantage of these materials' electrical conductivity ability to desorb water by the heat generated from the flowing current to establish a reversible reaction or even multi-responsiveness. In this context, bi-layered composites of PEDOT:PSS as a hygroscopic layer and PDMS as the non-hygroscopic substrate were investigated [23,24]. A straightforward and versatile method for fabricating bioinspired soft actuators was presented by Taccola et al. [23]. The effect of testing parameters such as current voltage, environment humidity, layers' thickness on the response of the bilayer composite was investigated both experimentally and theoretically. Dingler et al[28] studied the effect of relative humidity variation on the Young modulus and expansion of PEDOT:SS, both of which affect actuator movement. Okuzaki et al. [18] fabricated a biomorphic origami robot exploiting the hygroscopicity and the conductivity of polypyrrole. As a flexible carrier for copper clad with a polyimide Kapton®, Heibeck et al. [26] employed a composite of Ultra-High Molecular Weight Polyethylene (UHMW PE) and Pyralux®. They managed to take advantage of the mismatch between hygroscopic and thermal expansion to produce shape-changing products for possible application of lamp shading, responsive bookmark light, dynamic electronic device cover.

2.4 Bilayer composite production

A significant part of recent attempts to exploit materials' hygroscopic behavior have centered on employing these materials as an active layer in a bilayer composite, taking advantage of the linear expansion induced by changes in the environments' humidity levels. Despite the fact that several manufacturing procedures have been investigated for the creation of these bi-layered composites, a pattern may be detected based on the research field (See Table 2. 1 and Table 2. 2).

In the sector of building construction, the manufacturing method is restricted to 3D printing or the use of adhesives. While in sensors or wearable production sectors, fabrication methods vary based on the materials used in the passive and active layers. In certain studies, alternative production technologies have been recommended for the same materials. Regardless of context of research or materials used, the manufacturing method for the bi-layered self-actuator may be split into four major categories:

❖ ***Liquid adhesives*** are widely used for the production of bilayered composites. Reyssat et al. [30] ,who were the first to observe the aspect of bi-layered bending in pine cones, employed epoxy glue to join a cellulosic paper to a non-hygroscopic polymer to mimic the response of pine cones to changes in environment relative humidity. Vailati et al.[47] used a Henkel® polyurethane glue (Purbond HB-S709) to adhere two layers of beech and spruce. Similarly, in other investigations, polyurethane glues were used to join layers of wood [32,34,48,49] or one layer of wood to aluminum [25]. Holstov et al. [29] addressed different aspects of using glue as a bonding technique for coupling two wood veneer layers, pointing out the issues related to the mechanical properties of the glue, namely: proper flexibility (enough to withstand repeated bending without failure) and rigidity (enough to transfer shear stress between the layers), stating epoxy resins as the most suitable type of adhesive for this purpose.

❖ ***Printing*** techniques, including 3D printing, inkjet printing, and screen printing, have been used to create humidity-responsive bi-layered self-actuators. For the majority of the studies, the printing material was the passive layer that was deposited on a thin film of a hygroscopic material as the substrate. The choice of printing technique type, however, was dominated by the nature of the passive layer material. A mixture of wood filament with low moisture-sensitive polymers such as nylon, ABS, or PLA was 3D printed for responsive elements of the "HygroSkin: Meteorosensitive Pavilion [9,50]" project. Later on, Vazquez et al.[14] focused on formalizing the effect of the printing pattern of a mixture of wood filament and PLA on the deformation and response of 3D printed humidity-responsive self-actuators for architectural applications. On the other hand, inkjet and screen printing were used when a metallic thin film of copper [26] or carbon-based interdigitated electrodes (IDEs) [12,27] needed to be deposited as a passive layer on a hygroscopic substrate. Various printing techniques were used, in particular, to couple a hygroscopic polymer and a metallic layer where the mismatch between the hygroscopic and thermal expansion of the layers was employed to develop multi-responsive products. Some studies even extended the edge to deposit biological samples such as cell suspensions or biological solutions on a latex substrate using an inkjet printer, where the concentration or suspension density of the biological sample was determined based on the printing thread width, printing time, and needed thickness [10,11].

- ***Coating*** technologies such as spin coating or atomizing have shown to be one of the most suitable ways for applying a thin layer to a substrate for offering good control over the application thickness as well as acceptable surface morphology and uniformity. Spin coating has mostly been employed for the deposition of thin films with the thickness in scale of nanometer. In particular, this method has been used for application of PEDOT:PSS on PDMS substrates. Since PEDOT:PSS is commercially accessible as a ready-to-use aqueous dispersion, the production of homogenous films by spin coating with highly repeatable thickness in the tens to hundreds of nm range have been reported [23,24,28]. Atomization coating, on the other hand, was successfully utilized to deposit a single layer of cells with a thickness ranging from 1 to 3 micrometers [10,11].

- ***Dispersion*** technique is commonly used to create one-layer composites made of a mix of hygroscopic and non-hygroscopic elements. For example, the vacuum filtration of dispersed cellulose nanofibers and carbon nanotubes in 2,2,6,6-tetramethylpiperidine-1-oxyl (TEMPO)-oxidized/water solution, formed a monolayer of highly humidity sensors [13]. The water evaporation of dispersed cellulose pulps in aqueous solution of $BzMe_3NOH$ resulted in a cellulose hydrogel film which was exploited for skin moisture detectors [15]. This approach has been also explored for Electrochemical synthesized polypyrrole (PPy) [18] or Graphene/Cloisite hybrid [15] films.

- Other techniques have been also explored. Pipetting was adopted for the deposition of hygroscopic cells [10,11] and bacteria's [52]. Electrospinning has been utilized as a manufacturing method for self-actuators although it does not produce a completely homogenous thin layer of material. For example, Alexander et al. [42] introduce the potential of a synergistic interface of electrospun nanofiber mats and self-assembled nanofiber networks to create hygroscopic behavior, investigating the influence of procedure and composition on properties, such as water transport, layer thickness, and material modulus.

2.5 Hygroscopic properties and governing parameters

As can be seen in the selection of hygroscopic materials (wood) and manufacturing technologies (adhesive and 3D printing), the building construction industry is centered on a specific framework. There are no exceptions when it comes to the experimental characterization of hygroscopic behavior. In this sector that is interested in the behavior on a macro scale, the characterization of the behavior is mostly accomplished using image correlation [9,25,29–31,33,47,48] of the bent bilayer, with reference to the Berry and Pritchet et al. [37] model for bending cantilever, see Table 2. 1. Whereas in other areas like sensor development, product design, or wearable, the experimental approaches for characterization of behavior vary greatly depending on the subject material (e.g. cells, nanofibers, particles) and the identified governing parameters (e.g. concentration, hygroscopic expansion, etc.), see Table 2. 2. For the determination of governing parameters and the characterization of these properties, material engineering studies that investigate the popcorn cracking failure for the moisture sensitivity of polymeric materials for plastic packages of integrated circuit (IC) devices are probably the finest references [38].

In this context, the coefficient of hygroscopic expansion (α), which is defined as the ratio of the relative hygroscopic expansion produced in a dry material by absorbed moisture (ε_{hygro}) and the moisture concentration at saturation (C_{sat}), is the most important governing parameter to be determined. In this formulation, ε_{hygro}, also known as the hygroscopic strain, and C_{sat} are calculated in relation to the dry state, where L, M, and V represent the length, mass, and volume of the body in question, and the subscripts 'sat' and 'dry' denote saturated and dry conditions, respectively (Equation (2.1)).

$$\alpha = \frac{\varepsilon_{hygro}}{C_{sat}}\ , \qquad \varepsilon_{hygro} = \frac{L_{sat} - L_{dry}}{L_{dry}}\ , \qquad C_{sat} = \frac{M_{sat} - M_{dry}}{V_{dry}} \tag{2.1}$$

In terms of experimental methods, they may be split into two broad categories. One is to characterize the hygroscopic behavior or bending of bi-layered as a whole, utilizing methodologies such as Warpage Measurement of Bi-material Beams or image analysis of the bilayer using the beam cantilever bending curvature, and the other is to characterize all of the controlling factors that impact the process, specifically hygroscopic strain, saturation concentration, and diffusion coefficient. Table 2. 3 summarizes the most recent research on the characterization of hygroscopic behavior for the use of self-actuators, as well as fundamental investigations in microelectronics.

Table 2. 3. A summary of the experimental techniques adopted for the characterization of hygroscopic behavior as reported in literature

Field	**Material**	**Diffusion Coefficient**	**Concentration at saturation**	**Hygroscopic Expansion**	**Hygroscopic Expansion Coefficient**	**Ref.**
Sensors Development	PEDOT:PSS					24
	Polypyrrole		QCM			18
	cellulose nanocrystal	DVS	DVS	DIC		20
	CNF		TGA/DTA			16
	CNF					27
	CNF					12
	PEDOT:PSS		QCM		Image analysis	28
Product Design	Bacillus			SEM		52
	Natto cells			AFM	Image analysis	11
	Escherichia coli cells			AFM		10
Microelectronics	EMC*		Weighing	Moire´ interferometry		53
		Sorption Analyzer	TGA	DMA		54
			TGA	TMA	Warpage	55
		Weighing	Weighing	DIC		56
				DIC		57
		Weighing	TGA	DMA		58
					Warpage	59
Other	CFRP		Weighing	Laser interferometry		60
	Bamboo			DIC		42
	Cellulose		DVS			61

*EMC = Epoxy molding compound, AFM: Atomic Force Microscopy, QCM: Quartz Crystal Microbalance, DVS: Dynamic Vapor Sorption, DIC: Digital Image Correlation, TMA: Thermomechanical Analysis, TGA: Thermogravimetric Analysis.

Regarding the most suitable method for the determination of the material properties defining its coefficient of hygroscopic expansion, there has been considerable debate and contradiction between the researchers [62]. The main methods used to determine the material moisture concentration at saturation (C_{sat}) and the induced hygroscopic expansion (ε_{hygro}) are here reported.

- ***The evaluation of moisture concentration at saturation (C_{sat})*** has been investigated using a variety of techniques including Themmogravimetric Analysis (TGA) [16,54,55,58] , Quartz Crystal Microbalance (QCM) [18,28] , Dynamic Vapor Sorption (DVS) [20,61], and weighing [53,56,60] .

  Thermogravimetric Analysis (TGA) is one of the most extensively used method to determine the absorbed moisture mass, where the weight loss of a saturated sample due to moisture desorption at a constant temperature is quantified. The sample geometry constraints imposed by equipment requirements make it difficult to link TGA measurements with those of hygroscopic strains. Therefore, in some studies as an alternative for TGA, a finite element analysis of the desorption process is used for the mass loss calculation during the desorption[38,55].

  A Quartz Crystal Microbalance was used by Okuzaki et al. [18] to evaluate mass increase due to moisture sorption in a dry PPy polymerized on the balance gold electrode and exposed to ambient air (RH = 40%) at room temperature. An instantaneous mass uptake was detected which reached the equilibrium value of 4.3% within 3 minutes.

  Dynamic Vapor Sorption (DVS) has been used to characterize the kinetics of moisture sorption by employing a parallel exponential kinetics (PEK) [61] model or simply comparing the durations of sorption until the saturation [20,61]. This approach is appropriate for very sensitive materials with a fast response like cellulose. Balances have been widely used to characterize materials with a slower rate of moisture absorption, such as epoxy molding compounds, which achieve saturation in months [53,56,58].

- ***Hygroscopic expansion (ε_{hygro})*** evaluation have been performed using different techniques including the Thermomechanical Analysis (TMA) [38,55], the Atomic Force Microscopy (AFM) [10,11], the Scanning Electron Microscopy (SEM) [52], through methods based on interferometry [53,60], or Digital Image Correlation (DIC) analysis [20,56,57].

  Thermomechanical analysis is one of the most often used technique for hygroscopic strain determination via measurement of the dimensional changes of a saturated material sample during the heating induced desorption. In some cases, to differentiate the impacts of thermal expansion and hygroscopic shrinkage (hygrothermal deformation) during desorption, a dry sample must be specified as a reference, allowing the pure hygroscopic strain to be extracted from the hygrothermal deformation [55]. Then, this result will be accompanied by a parallel TGA (concentration characterization) analysis using the same thermal history to determine the coefficient of hygroscopic expansion from the slope of a fitted line to the curve of hygroscopic strain as a function of concentration [38,55]. The coefficient of hygroscopic expansion determined it this manner demonstrated to be in the same order of magnitude as the value determined using the warpage analysis [55]. When the drying temperature exceeds the material's glass transition temperature, the results must be carefully evaluated due to a considerable change in the material's stiffness. Moreover, due to the great difference in sample geometries for TGA and TMA tests, correlating these two data seems to be problematic [55,56,62–65].

Interferometry is another technique used to assess the in-plane displacements produced by moisture absorption, particularly in epoxy molding compounds used in microelectronics [53,60]. Because of its capacity to overcome the constraints of conventional point-measurement methods, this methodology can be an excellent tool to reach a high degree of accuracy in hygroscopic swelling assessment for materials with low rate of moisture absorption or desorption. Despite the complicated specimen preparation and measurement technique, it often substitutes thermomechanical analysis for the characterization of hygroscopic expansion. However, strain measurement in thin films using this technique requires careful attention to the applied external force since it might produce an unexpected deformation [53,57].

Digital Image Correlation (DIC) analysis uses a random pattern for the correlation of two images before and after deformation. Changsoo et al. [57] developed an experimental setup to use this technique for the measurement of hygroscopic strain in microelectronic packaging, specifying the measures to be taken with regard to the paint type and application of speckles in order to generate a suitable pattern for the test. The Atomic Force Microscopy (AFM) and Scanning Electron Microscopy (SEM) techniques, on the other hand, were employed to determine the volumetric expansion of a single cell or bacterium in the equipment with a controlled relative humidity chamber [10,11,52].

- Other methods for the holistic characterization of hygroscopic behavior are: measurements based on Archimedes principle where the volume and weight of the sample in two conditions of saturation in moisture and after baking at high temperature are measured [38], Flex sensor [48] placed between the two layers to obtain the induced bending curvature, and silicon-based microforce sensors [23] for the determination of the blocking force applied by the actuator on one end are reported in literature too.

The video recording of specimens exposed to several environment conditions differing in the relative humidity in a controlled setting until they reach the equilibrium has been widely adopted to define the bending curvature of a bi-layer composite. In this simple method, images perpendicular to the specimen are acquired. A polynomial curve or an arc of a circle is used to fit the bending boundary. The bending curvature will be calculated by the formula for the bending cantilever of beams [9,25,29–31,33,47,48]. Software such as Grasshopper and Firefly have been also used for the analysis of pictures obtained and for tracking the reaction and to monitor the response of specimens [31,34,48].

In particular, warpage measurement of bi-material beams is used to evaluate the direct impact of the hygroscopic swelling on the plastic packages at elevated temperatures. A rectangular bi-material beam is manufactured in a similar manner to that of semiconductor packing. It is necessary to employ an empirical approach to explore the so-called "stress-free" temperature of the package, which is determined by measuring the warpage of the beams at increased temperatures. When the bi-material beams are subjected to a humid environment, their warpage is seen to alter as a result of moisture absorption. Cure shrinkage and the Coefficient of Hygroscopic Expansion (*CHE*) are calculated using warpage measurements and a viscoelastic FE analysis [38,55,59]. This method , however, is not appropriate for materials with non-reversible hygroscopic expansion or bi-layered composites without a certain adhesion properties, where moisture absorption might induce micro-cracks or delamination between two layers [55,62,63].

2.6 Descriptive models

The model developed by Berry and Pritchet [37] for the bending movement caused by the deformation of a hygroscopic layer in a bi-layered structure has been adapted from Timoshenko's [35] model for the bending of bimetal strips, relying on the discoveries of Stoney [36] for in-plan stress induced by thermal variation in bimetal strips. Consequently, the computational models for this phenomenon have fallen into three main paths: in-plane stress in the bi-layered, leveraging analogies between heat transfer and diffusion kinetics, and the analytical model known as bending cantilever. Apart from these main categories, some individual personalized built-in codes[34], scripts in the Grasshopper and Firefly plugins[48], and nonlinear spring-based simulation model with ANSYS [33] have been investigated as well.

The direct reference to the conventional Stoney formula for in-plane tension has been used for the description of the behavior of bi-layered products that utilized humidity-sensitive cells as active layers [10,52]. Similarities between the governing equations of heat transfer and diffusion, on the other hand, have been used for many years as a computational analysis solution for the prediction of hygroscopic behavior of epoxy molding compounds in microelectronics [38,66]. This method makes use of heat transfer codes, that are already accessible in commercial softwares such as Abaqus (SIMULIA™ by Dassault Systèmes®) to simulate hygroscopic behavior replacing the thermal conductivity (k), temperature (T), and coefficient of thermal expansion (β) by a constant diffusion coefficient (D), equilibrium moisture concentration (C_{sat}), and coefficient of hygroscopic expansion (α), respectively (see Equation (2.2)), where q and J are the heat and moisture flux respectively).

$$q = -k\nabla T \ \rightarrow \ J = D\nabla C_{sat} \tag{2.2}$$

The bending cantilever model is mentioned within several papers in literature as an analytical paradigm for the design and description of bi-layered objects bending [9,23,25,28–30,32]. This model can be used to describe the moisture absorption-induced bending of a bilayer composite containing a hygroscopic material layer [37] if the hypotheses of Timoshenko [35] and Stoney's models [36] still holds. These hypotheses are related to: (i) layers' geometry where the thickness of the active layer has to be lower than the passive one ($h_a < h_p << R$); (ii) composite materials characteristics (they have to be homogeneous, isotropic and show a linear elastic behavior), and (iii) loading conditions in-plane stress state, negligible twist curvature, constant stress and curvature should be assured.

Equation (2.3) estimates the bending radius (R) generated by a change in relative humidity by substituting Coefficient of Hygroscopic Expansion (α) and moisture concentration variation (ΔC) for Coefficient of Thermal Expansion (CTE) and temperature variation, respectively.

$$\frac{1}{R} = \kappa = \frac{\Delta\alpha\ \Delta C\, f(m,n)}{h_{tot}}\ ,\ f(m,n) = \frac{6(1+m)^2}{3(1+m)^2 + (1+mn)(m^2 + \frac{1}{m})} \tag{2.3}$$

In this equation, $\Delta\alpha$ is the difference between the coefficient of hygroscopic expansion of the two layers ($\Delta\alpha = \alpha_a - \alpha_p \neq 0$) and h_{tot} is the total thickness of the bi-layered composite ($h_{tot} = h_a + h_p$), where the subscripts a and p refers to active (hygroscopic material) and passive, respectively. C is the moisture concentration of the active layer which depends on the level of relative humidity and f is a function of the thickness ratio ($m = h_p / h_a$) of the layers and the stiffness ratio ($n = É_p/É_a$, where $É_p = \frac{E_p}{(1-\upsilon_p)}$ and $É_a = \frac{E_a}{(1-\upsilon_a)}$) of the materials. Therefore, the induced bending curvature of a bi-layered composite is a function of environment Relative Humidity (RH, affecting C), of the materials' characteristics (coefficient of hygroscopic expansion and Young's modulus), and composite geometry (layers' thicknesses).

In 2015, COMSOL Multiphysics ® (5.1) included this feature as a subnode in the structural mechanics' interfaces, which allows to evaluate the deformations and stresses induced by varying moisture concentrations in solids. Although COMSOL Multiphysics ® has been used to simulate the hygroscopic behavior of wood in literature [49], the multiphysics feature of linking the concentration and the relevant mechanical deformation has not been considered, to the author's knowledge.

2.7 Project framework

Material selection for this project benefits from the lesson learned by comparing the advantages and drawbacks of the three main material categories addressed in this chapter as potential hygroscopic materials serving as a guide for the development of humidity-responsive self-actuators with the most suitable material for the purpose of this project. Despite the fact that wood is the most sustainable material among the categories presented here, the significant variation in hygroscopic behavior of wood from one species to another, as well as the variation in direction and location of wood veneer within a single specimen, places this material at the bottom of the selection list. Furthermore, the combination of wood veneers and textile does not appear to be a viable answer for the goal of this project, originally aimed at the improvement of emergency tents performance. In the case of conductive polymers, the large difference in absorption and desorption tendencies, as well as the requirement of using an electrical circuit for moisture desorption and recovery of the initial form, make this category the second choice of the list, given the limited availability of electricity in the context of emergency camps. As a result, cellulose-based materials resulted to be a preferable option for the goal of this project due to their low cost and autonomous self-actuation.

In terms of ***thin bilayer composite manufacturing***, we must anticipate the appropriate approach for the application of cellulose-based materials as a thin layer added to the currently available textiles for emergency shelters. Considering the mechanical (flexibility) and safety (nontoxic) requirements, as well as controlling the applied thickness of the adhesive, using adhesives to couple a thin film of a cellulose-based material with the textiles does not seem appropriate. The printing technique, on the other hand, is not suitable for mass production on an industrial scale. The dispersion method is suitable for the production of multi-responsive mono-layer. Coating technologies appear to be the most appropriate method in the context of this project, since they are applicable on an industrial size as well as on a small scale of application. Another type of coating that hasn't been looked into so far in the studies that have been cited in this chapter is a type of coater that uses a solution of the coating material and applies it as a wet lamina. This coater is available for both industrial and research laboratory scales. Given that the initial step toward using hygroscopic materials as an active layer in humidity-responsive products is the characterization of a stand-alone homogeneous hygroscopic thin film, this technique appears to be the best fit for the project's goals.

As presented in this chapter, the ***characterization of the hygroscopic behavior*** of materials have followed a different direction in different industries. Given that the interaction between the material and the water molecules is the cause of hygroscopic behavior for all hygroscopic materials, a deep understanding of this phenomenon and the parameters that govern it is the priority. The hygroscopic behavior of a material is responsible for a product dimensional variation as the results of moisture absorption or desorption from and to the environment. This notion emphasizes two major phenomena: one, mechanical deformation, and the other, the amount of moisture in the material, which caused the relevant deformation. Therefore, the measurement of the moisture content in a material and the associated induced strain is required for the characterization of the hygroscopic behavior. Consequently, techniques such as warpage, image analysis of a bending curvature, Archimedes-based methods, or flex sensor that characterize this behavior in a holistic scale are not suitable for this research.

The lesson learnt from various methodologies for characterization of these material properties is that selecting the most appropriate technique depends on factors such as subjected material, equipment limits, and even manufacturing process requirements. Apart from the limitation of each approach, regardless of the method used, both the hygroscopic strain (ε_{hygro}) and the moisture concentration at saturation (C_{sat}) are often evaluated throughout a moisture desorption process by comparing the starting (humid) and final (dry) values of a body mass and dimensions, assuming identical hygroscopic behavior during the absorption and desorption process. But, if the diffusion kinetic has to be taken into account, as for the diffusion coefficient measurement, it has been demonstrated that the diffusion kinetics for the moisture absorption and desorption processes often are different [67–69]. Given the complexities of moisture absorption/desorption processes, overlapping data from experiments based on various approaches based on different assumptions sometimes results in measurements with significant inaccuracies, especially, for thin films of highly hygroscopic materials during the absorption.

Since one of the goals of this study is to design a self-actuator containing a layer of cellulose acetate and to characterize its behavior in response to variations in relative humidity over time, beside the ***evaluation of moisture concentration at saturation*** at different relative humidity values, the characterization of cellulose acetate diffusion kinetic is of interest. Referring to the techniques above reported, for the aim of this thesis thermogravimetric analysis (TGA) equipped with controlled humidity would be required for complete characterization of cellulose hygroscopic behavior. Although Quartz Crystal Microbalance (QCM) can provide accurate quantitative results for mass variation, the samples must be deposited as a thin film on the quartz slab before measurements, which is inconvenient for the cellulose acetate films considered in this project that are obtained by solvent evaporation from casted solution. Balances, on the other hand, are available in any laboratory, is not dependent on sample preparation, and does not require a certain shape or form of sample. It can be used to measure the weight variation of a sample if placed in a controlled humidity environment. Despite the fact that weighing is time-consuming, and that multiple measurements may be necessary to provide an acceptable error margin depending on the precision and reliability of the balance, it appears to be the best technique for this project.

The diversity of methodologies to ***measure the hygroscopic strain*** is more. Moreover, being interested just in the evaluation of hygroscopic strain in a moisture-saturated material, the expansion kinetics do not need to be characterized. Interferometry techniques could provide a reliable method for determination of hygroscopic expansion; however, it would not be appropriate for cellulose-based materials that respond quickly to changes in relative humidity, because the material gains or loses moisture during the test and is no longer at equilibrium. Furthermore, because a hygroscopic layer sample is in the shape of a thin film, some unintended force may interfere with the test findings. The digital image correlation technique shares the same drawbacks of the interferometry technique for the cellulose-based material. A sophisticated SEM, working in humidity-controlled conditions, would be required for a proper microscopy evaluation of moisture induced expansion of a thin film. Having a thermomechanical analyzer available for this project, the characterization of cellulose acetate hygroscopic strain was carried with a TMA.

Regarding the ***descriptive model***, none of the models briefly described in this chapter appear to be adequate. The traditional Stoney model for in-plan tension and the cantilever beam bending model offer no insight into the kinetics of deformation. In the case of highly hygroscopic materials, relying on the heat transfer governing equation instead of diffusion does not seem appropriate, as these materials do not follow Fickian behavior for diffusion. Herein, we aim to develop a detailed and well-structured computational model that not only predicts the behavior of hygroscopic materials as the relative humidity changes, but it also describes the bending of humidity-responsive self-actuators containing a hygroscopic material as active layer bend as a function of environment relative humidity.

Figure 2. 5 displays the choices taken to proceed with this research in terms of hygroscopic materials selection, thin-film fabrication technology, and experimental procedures for the evaluation of material characteristics of which are utilized as inputs to a computational model. Cellulose acetate, a cellulose-based polymer, has been selected for this study. Solution preparation and solvent evaporation, have been chosen for the manufacturing of cellulose acetate membranes. The weighing technique will be used to estimate the diffusion coefficient (D) and moisture concentration of the membrane at saturation (C_{sat}) will be evaluated through weight measurements on a balance in a humidity controlled environment. The thermomechanical analysis will be used

to evaluate the hygroscopic strain (ε_{hygro}) induced in the cellulose acetate. Uniaxial tensile tests will be used to determine the membrane's Young's modulus. Finally, all measured properties, as well as other parameters, will be entered into the COMSOL Multiphysics ® software to describe the hygroscopic behavior of cellulose acetate membranes. Furthermore, the bending curvature of the humidity responsive self-actuator, made using cellulose acetate membrane as active layer, will be predicted by the numerical model and compared to tests and the bending cantilever analytical model.

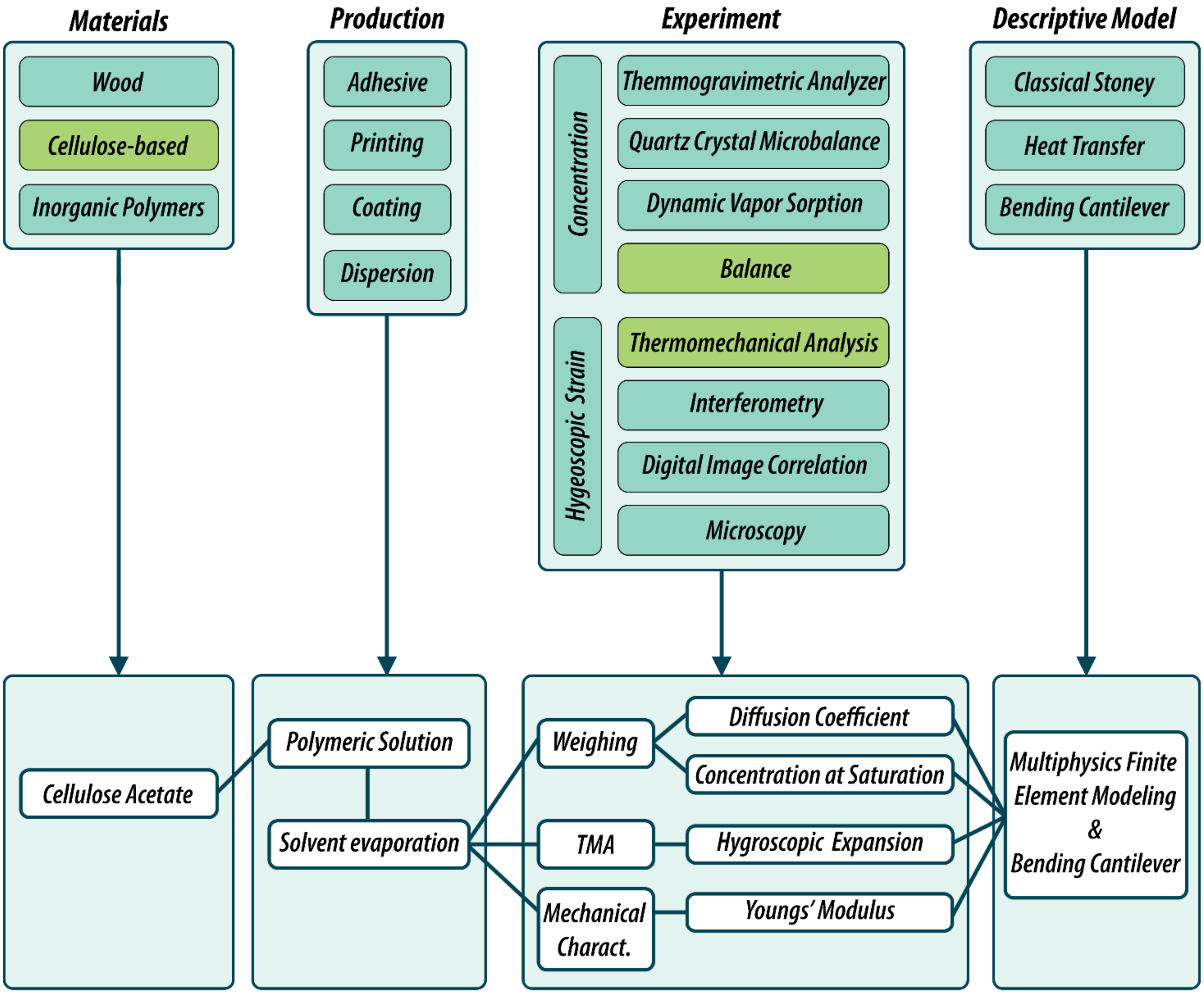

Figure 2. 5. Project framework

References

1. Berthold J, Rinaudo M, Salmeń L. Association of water to polar groups; estimations by an adsorption model for ligno-cellulosic materials. *Colloids Surfaces A Physicochem Eng Asp*. 1996;112(2-3):117-129. doi:10.1016/0927-7757(95)03419-6

2. Bridgens B, Holstov A, Farmer G. Architectural application of wood-based responsive building skins. In: *In Proceedings of the 12th International Conference on Advanced Building Skins*. ; 2017:2-3. https://www.researchgate.net/publication/320244562%0AArchitectural

3. Ramirez-figueroa C, Hernan L, Guyet A, Dade-robertson M. Bacterial Hygromorphs: Experiments into the integration of soft technologies into building skins. In: *ACADIA 2016 - Posthuman Frontiers*. Association for Computer Aided Design in Architecture; 2016:244-253. http://2016.acadia.org

4. Menges A, Reichert S. Performative Wood: Physically Programming the Responsive Architecture of the HygroScope and HygroSkin Projects. *Archit Des*. 2015;85(5):66-73. doi:10.1002/ad.1956

5. Simonson CJ, Olutimayin S, Salonvaara M, Ojanen T, O'Connor J. Potential for hygroscopic building materials to improve indoor comfort and air quality in the canadian climate. *Therm Perform Exter Envel Whole Build*. Published online 2004.

6. Xie H, Gong G, Wu Y, Liu Y, Wang Y. Research on the Hygroscopicity of a Composite Hygroscopic Material and its Influence on Indoor Thermal and Humidity Environment. *Appl Sci*. 2018;8(3):430. doi:10.3390/app8030430

7. Holstov A, Farmer G, Bridgens B. Sustainable materialisation of responsive architecture. *Sustain*. 2017;9(3). doi:10.3390/su9030435

8. Holstov A, Morris P, Farmer G, Bridgens B. Towards Sustainable Adaptive Building Skins with Embedded Hygromorphic Responsiveness. In: *Proceedings of the International Conference on Building Envelope Design and Technology - Advanced Building Skins*. ; 2015:57-67. https://www.researchgate.net/publication/278901137_Towards_sustainable_adaptive_building_skins_with_embedded_hygromorphic_responsiveness

9. Correa D, Papadopoulou A, Guberan C, et al. 3D-Printed Wood: Programming Hygroscopic Material

Transformations. *3D Print Addit Manuf*. 2015;2(3):106-116. doi:10.1089/3dp.2015.0022

10. Wang W, Yao L, Cheng C-Y, et al. Harnessing the hygroscopic and biofluorescent behaviors of genetically tractable microbial cells to design biohybrid wearables. *Sci Adv*. 2017;3(5):e1601984. doi:10.1126/sciadv.1601984

11. Yao L, Ou J, Cheng C-Y, et al. bioLogic:Natto Cells as Nanoactuators for Shape Changing Interfaces. In: *Proceedings of the 33rd Annual ACM Conference on Human Factors in Computing Systems*. Vol 2015-April. ACM; 2015:1-10. doi:10.1145/2702123.2702611

12. Rivadeneyra A, Marín-Sánchez A, Wicklein B, et al. Cellulose nanofibers as substrate for flexible and biodegradable moisture sensors. *Compos Sci Technol*. 2021;208:108738. doi:10.1016/j.compscitech.2021.108738

13. Zhu P, Liu Y, Fang Z, et al. Flexible and Highly Sensitive Humidity Sensor Based on Cellulose Nanofibers and Carbon Nanotube Composite Film. *Langmuir*. 2019;35(14):4834-4842. doi:10.1021/ACS.LANGMUIR.8B04259/SUPPL_FILE/LA8B04259_SI_001.PDF

14. Vazquez E, Gürsoy B, Duarte JP. Formalizing shape-change: Three-dimensional printed shapes and hygroscopic material transformations. *Int J Archit Comput*. 2019;18(1):67-83. doi:10.1177/1478077119895216

15. Wang Y, Zhang L, Zhou J, Lu A. Flexible and Transparent Cellulose-Based Ionic Film as a Humidity Sensor. *ACS Appl Mater Interfaces*. 2020;12(6):7631-7638. doi:10.1021/acsami.9b22754

16. González del Campo MM, Darder M, Aranda P, et al. Functional Hybrid Nanopaper by Assembling Nanofibers of Cellulose and Sepiolite. *Adv Funct Mater*. 2018;28(27):1703048. doi:10.1002/ADFM.201703048

17. Castaldo R, Lama GC, Aprea P, et al. Humidity‐Driven Mechanical and Electrical Response of Graphene/Cloisite Hybrid Films. *Adv Funct Mater*. 2019;29(14):1807744. doi:10.1002/adfm.201807744

18. Okuzaki H, Kuwabara T, Funasaka K, Saido T. Humidity-Sensitive Polypyrrole Films for Electro-Active Polymer Actuators. *Adv Funct Mater*. 2013;23(36):4400-4407. doi:10.1002/adfm.201203883

19. Wang DH, McKenzie RN, Buskohl PR, Vaia RA, Tan L-S. Hygromorphic Polymers: Synthesis, Retro-

Michael Reaction, and Humidity-Driven Actuation of Ester–Sulfonyl Polyimides and Thermally Derived Copolyimides. *Macromolecules*. 2016;49(9):3286-3299. doi:10.1021/acs.macromol.6b00250

20. Shrestha S, Diaz JA, Ghanbari S, Youngblood JP. Hygroscopic Swelling Determination of Cellulose Nanocrystal (CNC) Films by Polarized Light Microscopy Digital Image Correlation. *Biomacromolecules*. 2017;18(5):1482-1490. doi:10.1021/acs.biomac.7b00026

21. Ochoa M, Chitnis G, Ziaie B. Laser-micromachined cellulose acetate adhesive tape as a low-cost smart material. *J Polym Sci Part B Polym Phys*. 2013;51(17):1263-1267. doi:10.1002/polb.23337

22. Weng M, Zhou P, Chen L, et al. Multiresponsive Bidirectional Bending Actuators Fabricated by a Pencil-on-Paper Method. *Adv Funct Mater*. 2016;26(40):7244-7253. doi:10.1002/adfm.201602772

23. Taccola S, Greco F, Sinibaldi E, Mondini A, Mazzolai B, Mattoli V. Toward a New Generation of Electrically Controllable Hygromorphic Soft Actuators. *Adv Mater*. 2015;27(10):1668-1675. doi:10.1002/adma.201404772

24. Greco F, Zucca A, Taccola S, et al. Ultra-thin conductive free-standing PEDOT/PSS nanofilms. *Soft Matter*. 2011;7(22):10642. doi:10.1039/c1sm06174g

25. Abdelmohsen S. HMTM : Hygromorphic-Thermobimetal Composites as a Novel Approach to Enhance Passive Actuation of Adaptive Façades. *18th CAAD Futur 2019 Int Conf*. 2019;(June). Accessed December 14, 2021. https://www.researchgate.net/publication/332604413_HMTM_Hygromorphic-Thermobimetal_Composites_as_a_Novel_Approach_to_Enhance_Passive_Actuation_of_Adaptive_Facades

26. Heibeck F, Tome B, Della Silva C, Ishii H. uniMorph:Fabricating Thin-Film Composites for Shape-Changing Interfaces. In: *Proceedings of the 28th Annual ACM Symposium on User Interface Software & Technology*. ACM; 2015:233-242. doi:10.1145/2807442.2807472

27. Syrový T, Maronová S, Kuberský P, et al. Wide range humidity sensors printed on biocomposite films of cellulose nanofibril and poly(ethylene glycol). *J Appl Polym Sci*. 2019;136(36):47920. doi:10.1002/app.47920

28. Dingler C, Müller H, Wieland M, Fauser D, Steeb H, Ludwigs S. From Understanding Mechanical Behavior to Curvature Prediction of Humidity-Triggered Bilayer Actuators. *Adv Mater*. 2021;33(9).

doi:10.1002/ADMA.202007982

29. Holstov A, Bridgens B, Farmer G. Hygromorphic materials for sustainable responsive architecture. *Constr Build Mater*. 2015;98:570-582. doi:10.1016/j.conbuildmat.2015.08.136

30. Reyssat E, Mahadevan L. Hygromorphs: from pine cones to biomimetic bilayers. *J R Soc Interface*. 2009;6(39):951-957. doi:10.1098/rsif.2009.0184

31. Abdelmohsen S, Adriaenssens S, Gabriele S, Olivieri L, El-Dabaa R. Hygroscapes: Innovative shape shifting façades. In: *Lecture Notes in Civil Engineering*. Vol 24. Springer, Cham; 2019:675-702. doi:10.1007/978-3-030-03676-8_26

32. Wood D, Vailati C, Menges A, Rüggeberg M. Hygroscopically actuated wood elements for weather responsive and self-forming building parts – Facilitating upscaling and complex shape changes. *Constr Build Mater*. 2018;165:782-791. doi:10.1016/j.conbuildmat.2017.12.134

33. Reichert S, Menges A, Correa D. Meteorosensitive architecture: Biomimetic building skins based on materially embedded and hygroscopically enabled responsiveness. *Comput Des*. 2015;60:50-69. doi:10.1016/j.cad.2014.02.010

34. Grönquist P, Wittel FK, Rüggeberg M. Modeling and design of thin bending wooden bilayers. Johnson C, ed. *PLoS One*. 2018;13(10):e0205607. doi:10.1371/journal.pone.0205607

35. Timoshenko S. Analysis of Bi-Metal Thermostats. *J Opt Soc Am*. 1925;11(3):233. doi:10.1364/JOSA.11.000233

36. Stoney GG. The tension of metallic films deposited by electrolysis. *Proc R Soc London Ser A, Contain Pap a Math Phys Character*. 1909;82(553):172-175. doi:10.1098/rspa.1909.0021

37. Berry BS, Pritchet WC. Bending-cantilever method for the study of moisture swelling in polymers. *IBM J Res Dev*. 1984;28(6):662-667. doi:10.1147/rd.286.0662

38. Wong CP. *Moisture Sensitivity of Plastic Packages of IC Devices*. (Fan XJ, Suhir E, eds.). Springer US; 2010. doi:10.1007/978-1-4419-5719-1

39. Dinwoodie J. *Timber: Its Nature and Behaviour*.; 2000. Accessed January 3, 2022. https://books.google.com/books?hl=en&lr=&id=K02uDwAAQBAJ&oi=fnd&pg=PP1&ots=SY60

U12wOe&sig=4IlDtWcukBKOEOEPbM7lBKzKDDQ

40. Park T, Kim N, Kim D, et al. An Organic/Inorganic Nanocomposite of Cellulose Nanofibers and ZnO Nanorods for Highly Sensitive, Reliable, Wireless, and Wearable Multifunctional Sensor Applications. *ACS Appl Mater Interfaces*. 2019;11(51):48239-48248. doi:10.1021/acsami.9b17824

41. Anju VP, Jithesh PR, Narayanankutty SK. A novel humidity and ammonia sensor based on nanofibers/polyaniline/polyvinyl alcohol. *Sensors Actuators, A Phys*. 2019;285:35-44. doi:10.1016/j.sna.2018.10.037

42. Alexander SLM, Korley LTJ. Tunable hygromorphism: structural implications of low molecular weight gels and electrospun nanofibers in bilayer composites. *Soft Matter*. 2017;13(1):283-291. doi:10.1039/C6SM00749J

43. Okuzaki H, Kunugi T. Adsorption-induced bending of polypyrrole films and its application to a chemomechanical rotor. *J Polym Sci Part B Polym Phys*. 1996;34(10):1747-1749. doi:10.1002/(SICI)1099-0488(19960730)34:10<1747::AID-POLB5>3.0.CO;2-N

44. Zhou J, Anjum DH, Chen L, et al. The temperature-dependent microstructure of PEDOT/PSS films: insights from morphological, mechanical and electrical analyses. *J Mater Chem C*. 2014;2(46):9903-9910. doi:10.1039/C4TC01593B

45. Plomp M, Carroll AM, Setlow P, Malkin AJ. Architecture and Assembly of the Bacillus subtilis Spore Coat. Dague E, ed. *PLoS One*. 2014;9(9):e108560. doi:10.1371/journal.pone.0108560

46. Chen X, Goodnight D, Gao Z, et al. Scaling up nanoscale water-driven energy conversion into evaporation-driven engines and generators. *Nat Commun*. 2015;6(1):7346. doi:10.1038/ncomms8346

47. Vailati C, Bachtiar E, Hass P, Burgert I, Rüggeberg M. An autonomous shading system based on coupled wood bilayer elements. *Energy Build*. 2018;158:1013-1022. doi:10.1016/j.enbuild.2017.10.042

48. Abdelmohsen, Sherif; Massoud, Passaint; El-Dabaa, Rana; Ibrahim, Aly; Mokbel T. A Computational Method for Tracking the Hygroscopic Motion of Wood to develop Adaptive Architectural Skins. In: *Proceedings of the 36th International Conference on Education and Research in Computer Aided Architectural Design in Europe*. Vol 2. ; 2018:253-262. Accessed December 21, 2021. http://ecaade.org/downloads/eCAADe-2018-Volume2.pdf

49. Abdelmohsen S, Adriaenssens S, El-Dabaa R, Gabriele S, Olivieri L, Teresi L. A multi-physics approach for modeling hygroscopic behavior in wood low-tech architectural adaptive systems. *Comput Des.* 2019;106:43-53. doi:10.1016/j.cad.2018.07.005

50. Menges A, Krieg OD, Reichert S. HygroSkin: Meteorosensitive Pavilion | achimmenges.net. Accessed December 29, 2021. http://www.achimmenges.net/?p=5612

51. Schroeder HA. Shrinking and Swelling Differences Between Hardwoods and Softwoods. *Wood Fiber Sci.* Published online 1972:20-25. Accessed January 24, 2022. https://wfs.swst.org/index.php/wfs/article/view/2030

52. Chen X, Mahadevan L, Driks A, Sahin O. Bacillus spores as building blocks for stimuli-responsive materials and nanogenerators. *Nat Nanotechnol.* 2014;9(2):137-141. doi:10.1038/nnano.2013.290

53. Stellrecht E, Han B, Pecht M. MEASUREMENT OF THE HYGROSCOPIC SWELLING COEFFICIENT IN MOLD COMPOUNDS USING MOIRE INTERFEROMETRY. *Exp Tech.* 2003;27(4):40-44. doi:10.1111/j.1747-1567.2003.tb00122.x

54. Xiaosong Ma, Jansen KMB, Ernst LJ, van Driel WD, van der Sluis O, Zhang GQ. A new method to measure the moisture expansion in plastic packaging materials. In: *2009 59th Electronic Components and Technology Conference.* IEEE; 2009:1271-1276. doi:10.1109/ECTC.2009.5074174

55. Shirangi MH, Muller WH, Michel B. Effect of nonlinear hygro-thermal and residual stresses on the interfacial fracture in plastic IC packages. In: *2009 59th Electronic Components and Technology Conference.* IEEE; 2009:232-238. doi:10.1109/ECTC.2009.5074022

56. Park S, Haojun Zhang, Xin Zhang, Siu Lung Ng, Ho Chong Lee. Temperature dependency of coefficient of hygroscopic swelling of molding compound. In: *2009 59th Electronic Components and Technology Conference.* IEEE; 2009:172-179. doi:10.1109/ECTC.2009.5074012

57. Changsoo Jang, Yoon S, Bongtae Han. Measurement of the Hygroscopic Swelling Coefficient of Thin Film Polymers Used in Semiconductor Packaging. *IEEE Trans Components Packag Technol.* 2010;33(2):340-346. doi:10.1109/TCAPT.2009.2038366

58. He Y. In-situ characterization of moisture absorption-desorption and hygroscopic swelling behavior of an underfill material. In: *2011 IEEE 61st Electronic Components and Technology Conference (ECTC).* IEEE;

2011:375-386. doi:10.1109/ECTC.2011.5898541

59. Song R, Tajeddini V, Muliana A. Modeling and Simulation of Thin Layered Composites Under Non-mechanical Stimuli. *Front Mater*. 2020;7(April):1-15. doi:10.3389/fmats.2020.00097

60. Poenninger A, Defoort B. Determination of the coefficient of moisture expansion (CME). *Eur Sp Agency, (Special Publl ESA SP*. 2003;2003(540):567-572.

61. Lovikka VA, Rautkari L, Maloney TC. Changes in the hygroscopic behavior of cellulose due to variations in relative humidity. *Cellulose*. 25. doi:10.1007/s10570-017-1570-9

62. Jiang Zhou, Lahoti SP, Sitlani MP, Kallolimath SC, Putta R. Investigation of non-uniform moisture distribution on determination of hygroscopic swelling coefficient and finite element modeling for a flip chip package. In: *EuroSimE 2005. Proceedings of the 6th International Conference on Thermal, Mechanial and Multi-Physics Simulation and Experiments in Micro-Electronics and Micro-Systems, 2005*. Vol 2005. IEEE; 2005:112-119. doi:10.1109/ESIME.2005.1502784

63. Shirangi MH, Wunderle B, Wittler O, Walter H, Michel B. Modeling cure shrinkage and viscoelasticity to enhance the numerical methods for predicting delamination in semiconductor packages. *2009 10th Int Conf Therm Mech Multi-Physics Simul Exp Microelectron Microsystems, EuroSimE 2009*. Published online 2009:1-8. doi:10.1109/ESIME.2009.4938412

64. Shirangi H, Auersperg J, Koyuncu M, Walter H, Muller WH, Michel B. Characterization of dual-stage moisture diffusion, residual moisture content and hygroscopic swelling of epoxy molding compounds. In: *EuroSimE 2008 - International Conference on Thermal, Mechanical and Multi-Physics Simulation and Experiments in Microelectronics and Micro-Systems*. IEEE; 2008:1-8. doi:10.1109/ESIME.2008.4525009

65. Zhang H, Park S, Hong S. Hygroscopic swelling behavior of molding compound at high temperature. In: *2010 12th IEEE Intersociety Conference on Thermal and Thermomechanical Phenomena in Electronic Systems*. IEEE; 2010:1-7. doi:10.1109/ITHERM.2010.5501272

66. Yoon S, Han B, Wang Z. On Moisture Diffusion Modeling Using Thermal-Moisture Analogy. *J Electron Packag*. 2007;129(4):421-426. doi:10.1115/1.2804090

67. Crank J. *The Mathematics of Diffusion*. Oxford university press; 1979.

68. Mensitieri G, Scherillo G. Environmental Resistance of High Performance Polymeric Matrices and

Composites. In: *Wiley Encyclopedia of Composites*. John Wiley & Sons, Inc.; 2012. doi:10.1002/9781118097298.weoc074

69. De Wilde WP, Shopov PJ. A simple model for moisture sorption in epoxies with sigmoidal and two-stage sorption effects. *Compos Struct*. 1994;27(3):243-252. doi:10.1016/0263-8223(94)90085-X

3 Cellulose Acetate Membrane

This chapter will provide a comprehensive introduction of the structural and physical features of cellulose-based materials, with a focus on cellulose acetate (CA). The optimum experimental approach for producing pure cellulose acetate membrane from powder is described. The produced membrane's morphological properties are shown. The characterization of thermal and mechanical properties are reported as well.

3.1 Cellulose-based materials

Cellulose is the world's most abundant source of renewable polymer. Although the principal source of cellulose is wood, other plant components, agricultural leftovers, water plants, grasses, and even certain bacteria contain cellulose (Figure 3. 1). Cellulose and its derivatives' structure and characteristics are greatly reliant on the cellulose's source [1]. Bacterial cellulose, for example, has an exceptional ultra-fine network structure with high crystallinity and a significant proportion of water that is rather stable contained in the structure [2,3]. While, the structure and properties of plant-based cellulose vary depending on factors such as soil, climate, cultivation conditions, or even harvesting batch for the same species [1,3].

For commercial cellulose synthesis, wood and cotton are the most often used raw materials. Cellulose may be transformed into a plethora of derivatives with various functions, which can contain esters of organic acids such as acetates, inorganic acids such as nitrates, ionic or nonionic ethers, or even a mix of these functional groups from the same (e.g., acetate/propionate and acetate/butyrate), or distinct (e.g., ether and ester like carboxymethyl cellulose acetate butyrate) chemical classes [1]. As previously stated, the cellulose-based material under investigation in this work is a cellulose acetate. Hence, a brief overview of some structural features of this material would be beneficial in the context of its hygroscopic behavior.

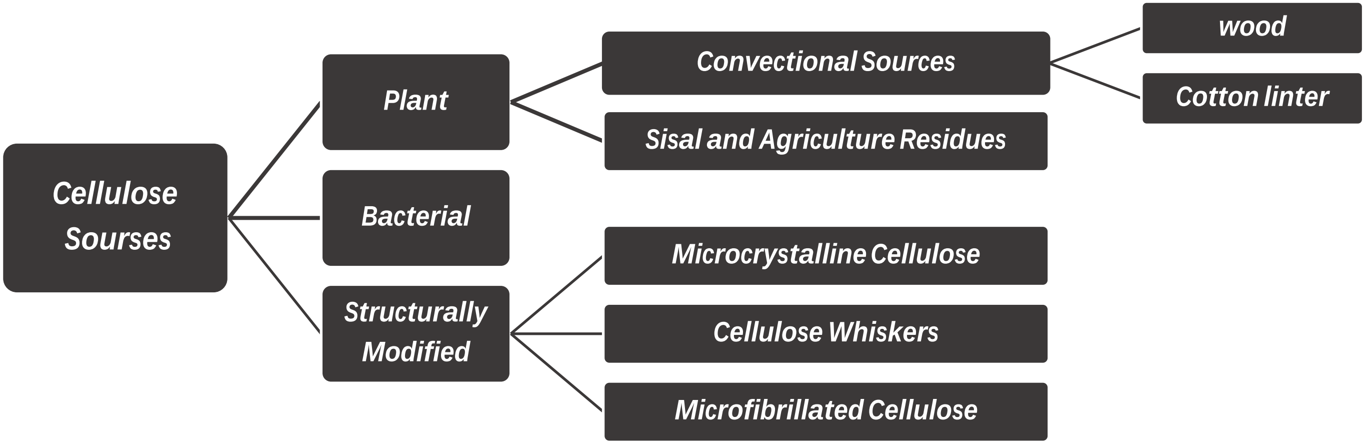

Figure 3. 1. Resources for different cellulose-based materials

Any acetate ester of cellulose, often cellulose diacetate, is referred to as cellulose acetate. Cellulose can be totally acetylated, which indicates that all three hydroxyl groups in the monomeric unit of the cellulose chain are acetylated, or partially acetylated if only one or two hydroxyl groups in the monomeric unit are engaged in the esterification reaction.

The cellulose acetate is typically obtained by reacting the functional hydroxyl groups in the monomer units of cellulose chains with acetic anhydride in either homogeneous or heterogeneous conditions [4]. The quantity of hydroxyl groups or acetyl groups that have replaced the hydroxyl groups is the most important factor in the hygroscopic behavior of cellulose-acetate, as hydroxyl side groups have a higher affinity for water than acetyl groups [4,5]. Therefore, the cellulose acetate's hygroscopic characteristics decrease as the number of acetyl groups increases. It must be mentioned that, in literature, the number of acetyl groups for cellulose acetate is given by different terminology, such as the Degree of Substitution (DS) or the acetyl group content or the acetyl acid content in percentage. Zugenmaier presented a table that converted the values for these terminology for the most often discussed cellulose acetates [6].

Due to the semi-crystalline structure of cellulose, cellulose acetate with a Degree of Substitution less than 2.9 are not manufactured directly [1]. Therefore, cellulose is always entirely transformed first to cellulose triacetate and subsequently to cellulose acetates with modest degrees of esterification by hydrolysis. The method used for the esterification or hydrolysis of cellulose has an impact on the characteristics of the produced cellulose acetate, such as its glass transition (T_g) and melting temperatures (T_m), as well as its solvent solubility [1]. For example, cellulose acetate with a degree of substitution ranging from 2.8 to 3 is only soluble in chloroform. Acetone and 2-methoxy-ethanol, on the other hand, are effective solvents for cellulose acetate with DS values of 2.2 - 2.7 and 1.2-1.8, respectively [7].

Mazzucchelli 1849 S.p.A. generously supplied the material used in this study, which is a powder of cellulose acetate made from cotton linter cellulose with 53.3 % acetic acid content. According to Zugenmaier's conversion table [6], this substance has a degree of substitution between 2 and 2.5. As a result, it can be dissolved in solvents such as acetone, according to the solubility categorization described by Heinze et al. [7].

3.2 Membrane Preparation

A substantial amount of literature reporting on cellulose membrane production has been analyzed in detail: the type of the adopted solvent, the use of additive materials (secondary solvent or plasticizer), the casting procedure, the type of substrate as well the solvent drying method and the adopted drying conditions (

Table 3. 1). Since the hygroscopic behavior of cellulose acetate has been seen historically as a flaw, the great majority of these studies utilized a plasticizer to minimize the impact of material hygroscopic behavior on the generated membrane performance. Consequently, the suitable solvent to obtain the solution of cellulose acetate in the presence of plasticizers is not dominated by acetone. Instead, the appropriate solvent is selected in relation to the intermolecular interaction between the cellulose acetate and the adopted plasticizers.

In terms of cellulose acetate concentration in solution, a range of 3% [8] to 17.5% [9] in weight has been recorded in relation to the quantity of the plasticizer. The viscosity of the solution, on the other hand, has a significant impact on the casting procedure. Solutions with a concentration of cellulose acetate lower than 10 % have been cast by pouring the liquid solution on the selected substrate [10–14]. While for solutions with higher viscosity, CA concentration 10-17.5 %, casting knife [9,15,16] or Doctor Blade [17] have been used.

Because of cellulose acetate's poor interfacial bonding/adhesion, due to its high wettability and naturally low surface energy [1], the selection of a suitable substrate is controlled by surface morphology rather than its constituent material. As a result, any smooth substrate that does not form a mechanical adhesion with the cellulose acetate solution can be used.

A systematic experimental arrangement was established to evaluate the effect of various factors on the CA membrane fabrication process (Figure 3. 2). Two solvents with different evaporation rates, namely acetone (high volatility) and ethyl lactate (very low volatility), were taken into consideration. Using each of the aforementioned solvents, the concentration of cellulose acetate in the solution was narrowed down to 10, 15, and 20 % w/w. Initial attempts to mix the powder and solvent, introducing the powder to the solvent immediately, resulted in very fast sedimentation of the particles and a prolonged mixing time. As a result, all the solutions were made by gradually adding cellulose acetate powder to the stirring solvent.

Table 3. 1. Details of publications in building construction area exploring hygroscopic materials

Solvent	Additive materials	Casting method	Substrate	Drying method and condition	Ref.
Aqueous NaOH	glycerin	pouring	paper	solvent evaporation	10
Acetone	Dioxane Acetic acid Methanol	Doctor Blade	glass	phase inversion	17
Tetrahydrofuran		casting knife	glass	solvent evaporation (RT*) phase inversion (water bath 5 or 25 °C)	15
Dichloromethane			glass	phase inversion	8
Acetone	polyaniline		glass	solvent evaporation (air oven 60 °C- 48 h)	18
Aniline	$K_2S_2O_8$ HCl			closed chamber (air oven- 60 °C- 48 h)	
1-Methyl-2-pyrrolidone	polyethylene glycol	casting knife	glass	phase inversion	9
Acetone		pouring	glass	solvent evaporation (RT)	11
Dimethylformamide	PA-6 nanofiber		Aluminum foil	solvent evaporation (Vacuum- 25 °C-24 h)	19
Acetone	organoclay suspension	pouring	glass	solvent evaporation (Oven-40 °C - 4 h)	12
Acetone	ε- caprolactone-trimethylolpropane	pouring	PTFE	solvent evaporation (Desiccator- RT)	13
Acetone	AgNO3 /water	electrospinning			20
Acetone, Dimethylformamide	polyurethane	roller machine		solvent evaporation (hot water- 70-90 °C)	21
N,N-dimethylformamide	polyethylene glycol	pouring	glass	phase inversion (water bath, RT)	14
methyl- (S)-lactate	LiCl - CaCl2	casting knife	glass	phase inversion (water bath, RT)	16

* RT: Room Temperature

A magnetic stirrer (IKA ® RCT basic IKAMAG™) was used for the mixing. The procedure for preparing the solution differed depending on the solvent and the concentration of cellulose acetate. Regarding the influence of solution concentration, a more diluted solution required less time for the mixing, as expected. Even though electrospinning is used for membrane production, it was not considered in this study, because it produces a layer not sufficiently homogenous and containing a significant amount of pores [20,22]. The method of pouring and using Doctor Blade coating were employed. Pouring was explored for casting solution with a 10 % concentration. For the application of a more viscous solution (15 and 20 % of concentration), a Doctor Blade with controlled velocity casting knife was employed. Regarding the substrates, in addition to a PVC, other substrates suggested in literature were tested.

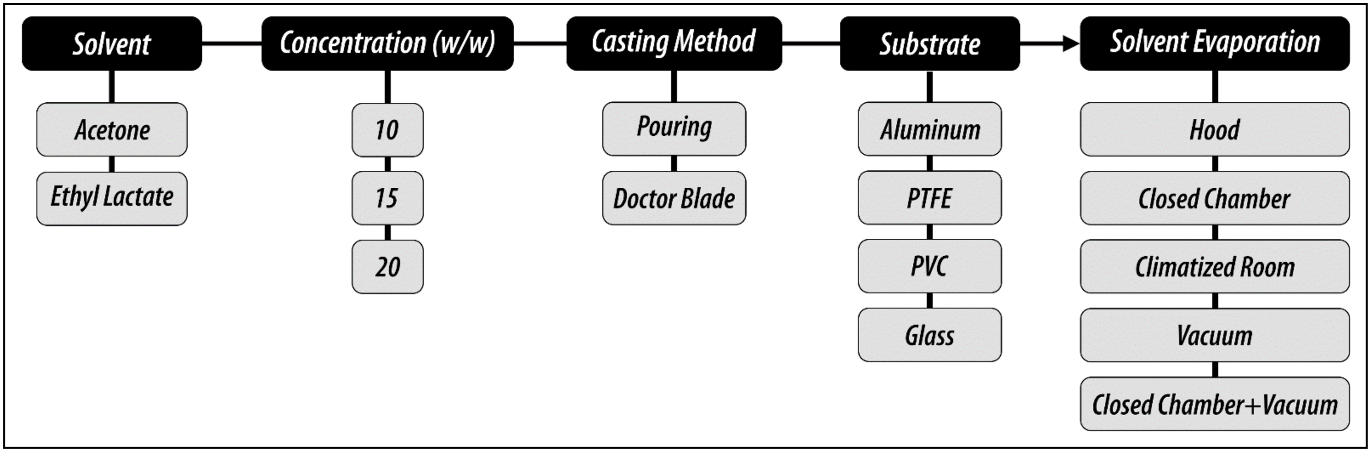

Figure 3. 2. Designed experimental layout for the optimization of membrane preparation procedure

Despite the outcome presented in literature [9,15–17], several attempts to employ phase inversion with cold, room temperature, and hot coagulation baths resulted in immediate plasticization of the membrane, color change, extreme arbitrary deformation, and delamination of the membrane from the substrate. This is due to a lack of plasticizer in the solution, which affects the interactions between cellulose acetate and water molecules. Therefore, a proper solvent evaporation method was selected. Initially, a solvent evaporation in the oven at temperatures below the boiling points of the solvents, 50 °C for acetone solutions and 100 °C for ethyl lactate solutions, was contemplated but the formation of bubbles trapped through the thickness after solvent evaporation was observed. Therefore, other drying procedures were considered: a slower solvent evaporation was performed at ambient temperature under various environments, including under a hood, in a closed chamber, in a climatized room, and in a vacuum oven. The systematic study performed highlighted how each of the considered parameters related to the solvent evaporation process affects the quality of the obtained membrane, evaluated simply by a visual analysis.

- ***Solvent and solution concentration:*** The significant difference in evaporation rates of the solvents (1.9 for acetone and 60.5 for ethyl lactate on the European scale that means the evaporation rate is normalized with respect to that of diethyl ether evaporation [23]) had a direct impact on the solution preparation process as well as the drying time of the membranes. Since acetone dissolves cellulose acetate faster than ethyl lactate, for a constant concentration of CA in the solution, the mixing time for the solution using acetone was nearly half that of the solution using ethyl lactate as the solvent. However, experimental problems due to the high volatility of acetone were encountered during the casting process. When a CA/Acetone solution with a concentration of 10% w/w was poured into a Petri dish (poured thickness of 500 μm), the surface of the membrane dried immediately and prevented the evaporation of the solvent underneath layers. Lower applied thicknesses resulted in a very thin and fragile layer, making membrane peeling difficult.

  This draw back observed for casting of CA/Acetone solutions with higher concentration (15 and 20 %) by Doctor Blade as well. After pouring the solution in front of the casting knife, the upper surface dried instantly and transferred to the bottom layer (in contact with the substrate) by the movement of the knife, causing immediate delamination and bubbles. Furthermore, acetone-based solutions are considerably more fluid than ethyl lactate-based solutions, and after casting a specified thickness using a Doctor Blade, the cast solution would spread laterally, resulting in a considerably lower ultimate thickness. Overall, cellulose acetate acetone-based solutions are better suited for industrial applications requiring a high-speed automated coating process.

  Ethyl Lactate, on the other hand, required more time and a more sophisticated dissolving operation, particularly for solutions containing 20% cellulose acetate. Initially, the time required for ethyl lactate to dissolve the cellulose acetate was approximately 6 hours of stirring at 200 rpm at room temperature for a 10% concentration solution, increasing to 10 hours for a 20% concentration solution. To speed up the dissolving process, the mixing temperature was raised to 80 °C (boiling point of ethyl lactate 154 °C). As a result, the dissolving time for 10% and 20% concentration solutions was reduced to 1.5 and 3 hours, respectively. Among the ethyl lactate-based solutions (10, 15, and 20% w/w concentration of cellulose acetate), only the solution of 20 % concentration resulted to be suitable for casting. The following is the optimized procedure adopted for preparing a 20 % concentration in weight solution of cellulose acetate in ethyl lactate:

(i) heating 80 gr of ethyl lactate (≥98% purity, purchased from Sigma-Aldrich) to 80° C;
(ii) stirring the solvent at 300 rpm (RCT basic IKAMAG™ magnetic stirrer);
(iii) adding gradually 20 gr of cellulose acetate powder to the stirring solvent;
(iv) closing the container to avoid solvent evaporation;
(v) stirring the mixture at 300 rpm for 90 minutes;
(vi) reducing the stirring speed to 200 rpm and stirring for 90 minutes;
(vii) cooling the solution to room temperature over the night.

- ***Casting method:*** Pouring as a casting procedure has various disadvantages. The main one is that to minimize spreading of the liquid (low viscosity of 10% concentration solutions) and regulate the thickness, the utilized substrate must have vertical barriers, such as a Petri dish. Due to the adhesion of the solution to the border, after evaporation of the solvent, the final membrane was thicker around the border and thinner in the center (concave cross-section), resulting in a non-uniform thickness. As a result, utilizing a Doctor Blade that allows to adjust the thickness and casting velocity appears more suitable.

- ***Substrate:*** Although the low surface energy of cellulose acetate was noted as a benefit for substrate selection, certain downsides were found throughout the experimental procedure of casting on PTFE substrate. Since the cohesive force between solution molecules was greater than the adhesive force between the solution and the substrate, the mixture shrunk and generated droplets after pouring. Aluminum foil was found to be insufficiently thin and delicate as a substrate, as the residual stress due to solvent evaporation induces deformation in the membrane throughout the drying process, resulting in a non-planar membrane. PVC substrate, on the other hand, demonstrated resistance to residual stress deformation. It also displayed adequate adhesion qualities during the casting process. During the drying process, however, the membrane peeled off from the substrate. Since none of these concerns were encountered while employing glass as the substrate, it was selected as the best alternative.

- ***Solvent evaporation:*** With temporal monitoring of the membrane weight, the time required for complete evaporation of the solvent in air was determined as the time when the no significant change in weight was recorded any more starting from a 500 μm thick of cast solution. Attempts to dry the membrane in a vacuum oven were unsuccessful since the vacuum condition promoted the formation of bubbles, resulting in a non-homogeneous membrane. Figure 3. 3 depicts the weight loss of a 500 μm thick film of the applied solution (20% concentration) as a function of time, normalized to its value at time zero, for the different drying methods listed in the experimental framework (Figure 3. 2). For the mentioned solution (20% concentration w/w), the membrane can be regarded dry when the applied solution has lost 80% of its original weight (corresponding to solvent content). Given that the Doctor Blade controlled thickness for the cast solutions was 500 μm, a thickness of maximum about 100 μm is expected for the dried membrane.

As can be observed, the two solvent evaporation conditions of the closed chamber and the climatized room, show the same trend which is very slow. The membranes lost only roughly 65% of their initial weight after 72 hours. The solvent evaporation slows as the membrane dries and hardens at the surface, therefore the dry state (when the weight of the membrane is 20% of the applied solution) in these two environments would be unsuitable. The membrane dried in the climatized room and closed chamber were considered dry after reaching 22.5% (170 hours) and 24% (230 hours) of their initial weight, respectively. Starting from applied solution thickness of about 500 μm, dry membranes of approximately 75 μm were obtained in both situations, with a significant scatter of 17 μm. Moreover, a rough surface was obtained on membranes dried in the climatized room, see Figure 3. 4 (a). Membranes dried in a closed chamber, on the other hand, had a smooth surface.

The membrane dried under a hood lost about 76% of its weight during the first four hours. Then, the weight loss rate leveled off and after 8 hours of drying the membrane the normalized weight reached the plateau value of 21.5 %. The obtained dry membrane had a thickness of 69 μm with a considerable scatter of 10 μm. In addition, it seems that the hood's air flow had a significant impact on the surface morphology of this membrane (Figure 3. 4 (b)).

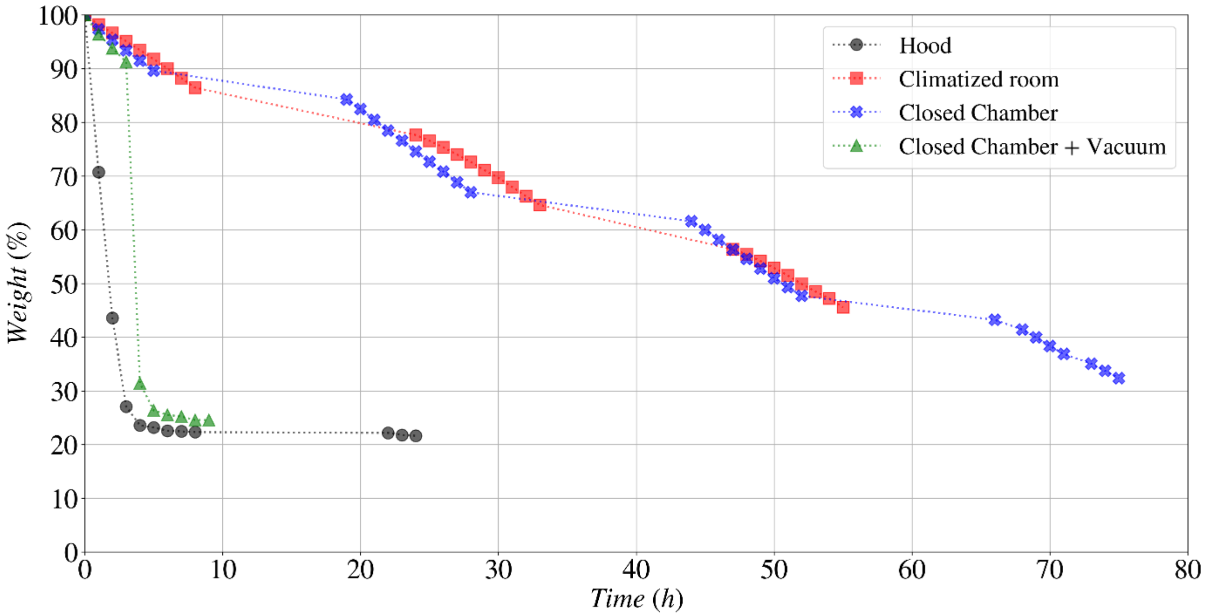

Figure 3. 3. Variation in time for membranes weight, normalized to its value at time zero

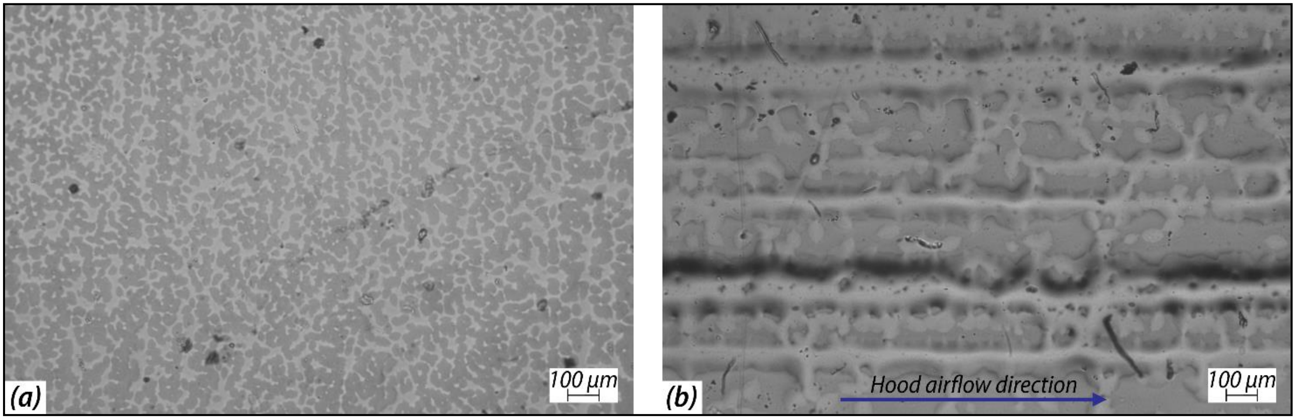

Figure 3. 4. Microscope image of dried membrane, a) in climatized room, b) under hood, (microscope: Olympus BX-60 equipped with Infinity 2 camera)

The last drying technique used was based on the lesson learnt from the disadvantages of drying by vacuum and closed chamber. The production of large bubbles during vacuum drying suggested that the applied solution includes air bubbles that were not detectable by the naked eye. On the other hand, if the membrane's surface dries quickly, bubbles may be trapped beneath. As seen in the curves for the closed chamber and climatized room (Figure 3. 3), the applied solution loses approximately 2% of its weight every hour.

A combination of these two drying conditions will be appropriate for optimizing membrane homogeneity and production time. First, the membrane was placed in a closed chamber for 3 hours to slow down solvent evaporation rate at the beginning of the drying process, giving time to micro-bubbles to reach the surface and burst while the surface is still fluid. Then, it was dried in a vacuum oven at room temperature for 4 hours to accelerate the solvent evaporation (Figure 3. 3 (a) triangle symbol). Using this procedure, membrane with thickness of 70 ± 4 μm was produced, with a final weight of 24 % of the initial weight. The satisfactory scatter of 4 μm across the thickness of the obtained membrane made this method the most appropriate for the next step of investigation.

To assess the repeatability of the chosen drying procedure (closed chamber and vacuum), three different thicknesses of the casted solution (400, 500, and 600 μm) were employed and two specimens were tested per each thickness. Although it is reasonable to expect a decrease in drying time as the applied thickness is decreased, neither the normalized weight nor the time for drying were affected by the film thickness in this range. The average normalized weight plotted versus time and the standard deviation for six membranes dried using the closed chamber and vacuum method are presented in Figure 3. 5. A drying time reduction has been observed instead in extremely thin thickness (lower than 100 μm) that was completely dry after one hour in vacuum. The dry membrane thickness, on the other hand, as expected, resulted to be dependent on the cast solution applied thickness. Dry membrane thicknesses of 66 ± 2, 70 ± 4, and 84 ± 3 μm were obtained for the applied cast solution thicknesses of 400, 500 and 600 μm, respectively.

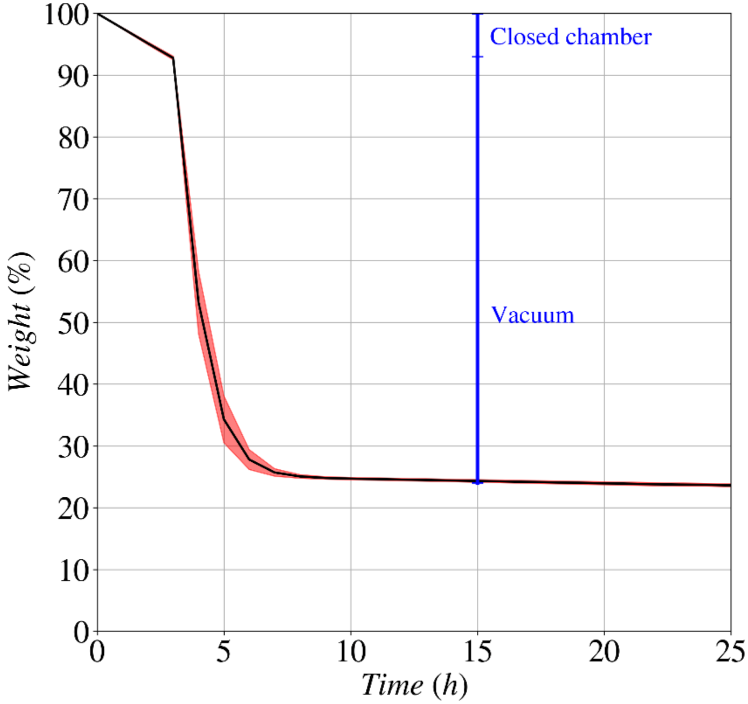

Figure 3. 5. Mean value of the normalized weight as a function of time and standard deviation for six membranes dried for 3 h in a closed chamber and then under vacuum

A major drawback of this membrane production process was a rolling of the membrane after its peeling from the substrate. This effect could be related to internal stresses originated by solvent evaporation and solution solidification. During the solvent evaporation process, the applied membrane loses solvent from all the surfaces exposed to the air. Therefore, not only does it shrink through the thickness due to solvent evaporation, but it also shrinks across the latter. As it is constrained from one end to the glass substrate, shrinkage along length and width is limited, which causes an internal stress in the membrane [24,25]. After the membrane has been separated from the substrate, it is free to deform, resulting in rolling of the obtained membrane where the top surface that was dried first compresses, putting tension on the side of the latter that was in contact with the glass substrate. Furthermore, as previously stated, the membrane has reached 24 % of its initial weight at this point, indicating that the solvent did not evaporate completely. Therefore, a 24-hour thermal treatment at 125 °C (lower than both the boiling point of ethyl lactate, equal to 154 °C, and the glass transition temperature of cellulose acetate equal to 175 °C, as show in Figure 3. 8) was considered.

After comparing all the experimental results and taking into account the contribution of the various parameters presented in the framework (Figure 3. 2), the optimal procedure for preparation of the cellulose acetate membranes for experimental investigations is (Figure 3. 6):

(i) pouring the prepared solution on a glass substrate at room temperature;

(ii) casting a solution film (10 × 24 mm^2) with thickness of about 500 μm with a K Control Coater at the lowest velocity (3 mm/s);

(iii) keeping the solution film in a closed chamber (isolated from air flow) for 3 hours to assure a slow solvent evaporation and thus to avoid formation of bubbles;

(iv) putting the membrane for 4 hours in vacuum oven (Vuototest Mazzali) to accelerate the solvent evaporation;

(v) peeling the membrane from the glass substrate;

(vi) putting the membrane between two metal frames with dimension of about 8 × 18 mm^2 (equal exposure of surface to air);

(vii) drying in air oven (Mazzali Thermair) for 24 hours at 125 °C (thermal treatment).

Membranes with thicknesses ranging from 66 ± 1.5 to 70 ± 4.5 μm were produced. Membranes with thicknesses between 145 ± 2 and 200 ± 10.5 μm, on the other hand, have been obtained performing the above detailed procedure from step (i) to step (iv) using the CA membrane at step (iv) as the substrate instead of glass. To avoid any unintended influence of the clamping system of the metal frame, the central part of each membrane, at a distance of 1 cm from the metal frames, was considered the eligible area to cut the specimens.

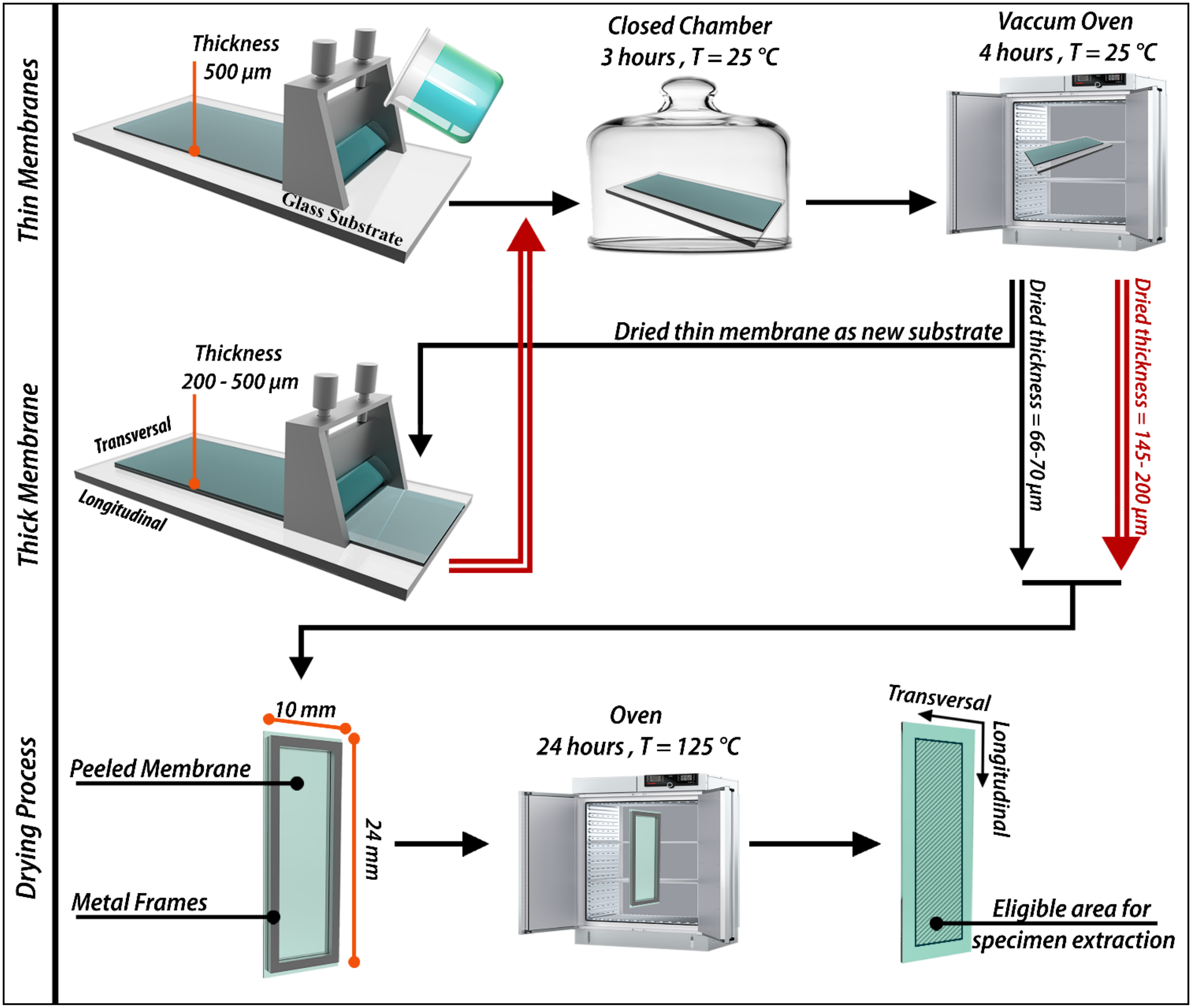

Figure 3. 6. Schematic representation of the optimized procedure for membrane production and drying process

3.3 Scanning Electron Microscopy (SEM)

One of the most important aspects of the membrane is its surface morphology. In the context of this research, the surface morphology not only emphasizes the homogeneity of the fabricated membrane, but it also highlights the ability of interaction with water molecules. Since no specific drawbacks were observed under the microscope for the membrane produced by the optimized procedure for membrane preparation (Figure 3. 6), the surface morphology investigation was carried out on a smaller scale using scanning electron microscopy (SEM). Figure 3. 7 shows SEM images of the membrane with a thickness of 147 ± 4 μm (measured with micrometer) obtained by applying the second layer of 500 μm of solution on a dry cellulose acetate membrane casted on a glass substrate. Specimen was cut with a cutter. A SEM Zeiss Evo 50 EP in high vacuum configuration was used to obtain the image.

As shown in Figure 3. 7 (a) the membrane has a smooth surface, and this justifies the low scatter in the membrane's thickness measurement equal to 4 μm. Since the membrane was applied in two steps, a line along the thickness, dividing the section into two layers, could've been expected. However, no separation line is visible along the membrane thickness. This implies that the ethyl lactate in the second layer of the applied solution may have dissolved the cellulose acetate in the top layer of the dried membrane, resulting in a proper interaction and adhesion with the underneath layer at the interface. This suggests that such a thick membrane can be considered as a homogenous body and the delamination between two layers of the membrane induced by hygroscopic strain caused by moisture absorption from one of the latter is not an issue.

Figure 3. 7 (b) portrays a section of the membrane that is without pores. This result confirms the efficacy of the optimized procedure for membrane preparation, which produces a homogeneous membrane in comparison to those in the literature [22]. This is a significant benefit for the hygroscopic behavior of cellulose acetate membranes. When a porous membrane of a hygroscopic material is exposed to higher humidity levels, the water molecules first fill the pores without engaging in intermolecular interactions. After filling the pores, they diffuse in the solid material, interact with the polymer molecules functional groups, causing an expansion [26]. This phenomenon has a direct effect on two aspects: the time required for the material to respond to changes in the relative humidity level by changing its dimension and the material coefficient of hygroscopic expansion. Porous hygroscopic materials have a dual stage of moisture diffusion to reach the saturated concentration; as a result, they respond to changes in humidity starts with a delay and much slower rate [26]. The measured moisture concentration in porous material includes also the moisture mass that fills the pores but does not participate in

hydrogen bonding. Being the denominator of the fraction of hygroscopic expansion coefficient ($\alpha = \frac{\varepsilon_{hygro}}{C_{sat}}$), an increase in concentration at saturation results in a decrease of the coefficient of hygroscopic expansion for a constant value of hygroscopic strain.

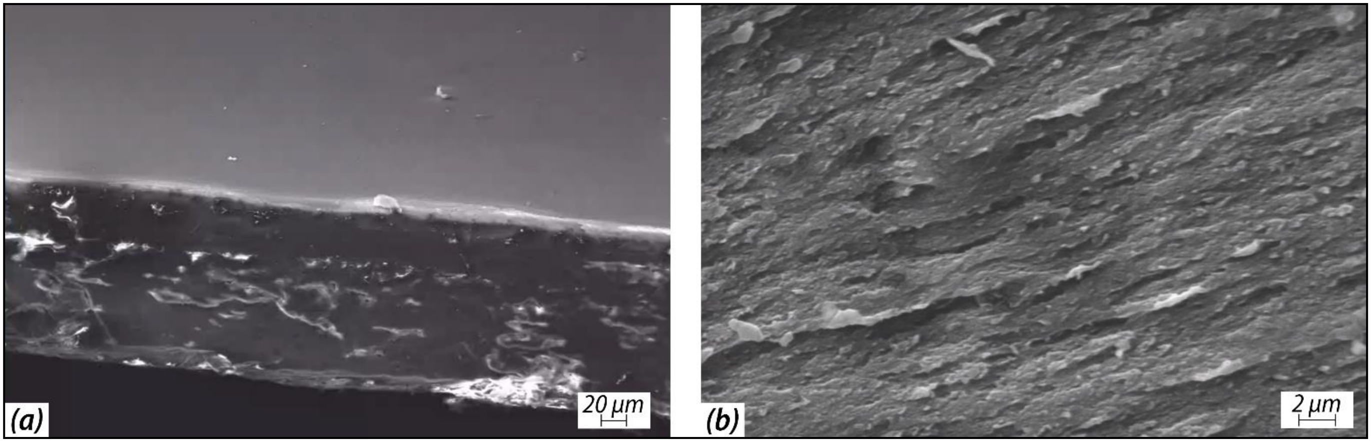

Figure 3. 7. SEM image of the membrane dried in closed chamber and vacuum a) a view of membrane surface and its cross section b) detail of the cross section.

3.4 Thermal properties

3.4.1 Differential Scanning Calorimetry (DSC)

Since the hydroxyl content in cellulose derivatives has a large influence on the glass transition and melting temperature [27], a comparison between the cellulose acetate tested in this research and the results provided in literatures with a different degree of substitution would not bring to light any aspect. Comparing the differential scanning calorimetric of CA powder and the membrane produced with the optimized drying technique, on the other hand, can offer information about the understudy cellulose acetate, influence of the membrane preparation procedure, and thermal limitations for further experiments.

Differential scanning calorimetry analysis was carried out by DSC3 - METTLER TOLEDO. Specimens weighing around 5 - 6 mg of powder or membrane were placed in 40 µl aluminum pans. The specimens were heated in Nitrogen atmosphere (60 ml/min. furnace flux) at a rate of 10 °C/min from -50 °C to 330 °C and 240 °C for powder and membrane, respectively. Previous attempts to heat the CA membrane to 330 °C were unsuccessful, as specimen pyrolysis was detected with onset at 260 °C. Thus, the maximum temperature for testing the membrane was set at 240 °C when a second heating ramp was carried out to compare the response of the dry material to that of the material equilibrated to a relative humidity of 50 %

Figure 3. 8 depicts the results of DSC on the mentioned specimens. Within the temperature range of 25 °C and 150 °C, all specimens exhibit an endothermic peak, that has been already observed for other cellulose derivatives membranes as well [15,22]. The disappearance of this peak in the second heating curves (not presented in the graph) indicates that this phenomenon was driven by water evaporation. Compared to the CA powder, the domain of this endothermic peak for CA membranes shifts to a lower temperature range. For the CA powder, the onset temperature of water evaporation is 52 °C and the peak temperature is of 96 °C. These values are reduced to 27 °C and 74 °C for CA membranes, respectively. With the same approach as the reported literature [15,22], glass transition midpoint temperature of approximately 212 °C was measured for CA powder, but this value drops to 175 °C for cellulose acetate membrane. The melting peaks of CA powder and membrane were found to be 280 °C and 190 °C, respectively.

It is important to highlight that the amorphous fraction of the semi-crystalline CA (3.1) is responsible for water absorption. Therefore, a research on the degree of crystallinity may be of interest in the case of distinct types of cellulose acetate generated using different derivation methods. However, in this study, the cellulose acetate and the membrane fabrication procedure are fixed, and the characterization of this element would not be necessary in this context.

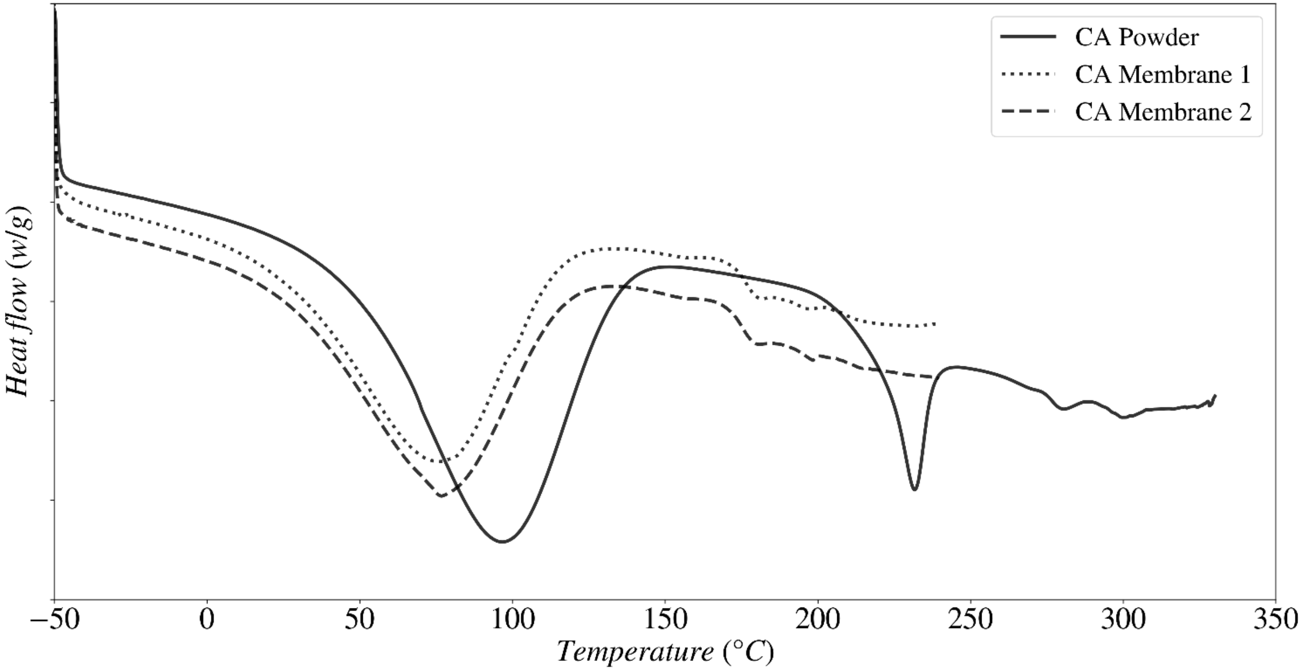

Figure 3. 8. Differential Scanning Calorimetry thermograms of CA powder and membranes

3.4.2 Thermogravimetric Analysis (TGA)

Thermogravimetric analysis allowed to provide information about the material's moisture absorption and its degradation temperature. A TA Instruments TGA Q500 analyzer with Alumina furnace was used for thermogravimetric measurements. CA powder and membrane specimens, with a weight between 6 and 16 mg, were first conditioned for 72 hours at a relative humidity of 51% (T = 25 °C). Then, they were put in 50 µl platinum pans and immediately after, weighed using the TGA balance to evaluate their initial weight. They were then heated from ambient temperature to 600 °C at a rate of 10 °C/min in Technical air (Air 0), with gas flow of 40 ml/min to the balance, constantly recording their mass.

Figure 3. 9 (a) illustrates the normalized residual mass of both CA powder and membrane (averaged on three specimens for each) as a function of temperature. The mass loss presented in this graph can be divided into three main stages. The first stage is from room temperature to 150 °C where both specimens showed a mild mass loss of about 4.5 %. This step is entirely consistent with the peak observed in DSC curves, and is correlated to the evaporation of physically bound water as well of water tightly bound to cellulose acetate hydroxyl groups. The second and the third stage of mass loss are attributed to a dual decomposition step in both specimens, with the same trend stated in the literature [22,27]. The second stage is associated with CA chain breakdown and corresponds to the primary heat decomposition event. This stage for CA powder runs between 290 °C and 400 °C, whereas for CA membrane it initiates at a lower temperature of about 200 and continues up to 400 °C, causing a mass reduction of about 80% for both powder and membrane CA. The decomposition starting temperature depends again on the degree of the substitution of cellulose acetate (chemical structure) and the preparation method of the membranes [1]. The TGA curve for the CA membrane is consistent with the intensive degradation at about 260 °C mentioned commenting the differential scanning calorimetry results. The third stage of decomposition (the ultimate step of mass loss) from 400 to 600 °C is linked to sample carbonization, after which no material residue is present.

Figure 3. 9 (b) depicts the mean value of the normalized mass loss due to water desorption in low temperature range, along with the standard error. At first glance, it is clear that the loss curves do not begin at exactly 100 %, due to the rapid response of the cellulose acetate. Even though all of the specimens were maintained for 72 hours in a climatized chamber under specific conditions (RH=51 percent and T=25 °C), the absorbed water begins to evaporate between the initial weight measurement of the specimen with TGA instrument balance and the beginning of the test. Furthermore, due to instrument cooling limitations, the test in air could not begin at 25 °C. As a result, beginning from the temperatures shown in the graph (34.2 °C for CA powder and 35.7 °C for CA membrane), the cellulose acetate has already desorbed some moisture before starting the test data acquisition. In contrast to what observed in DSC test, TGA indicates that the CA powder dries faster than the membrane. This is related to the greater surface area exposed to air of the cellulose acetate powder, and the center of each grain achieve the intended temperature faster than a membrane with a thickness of roughly 150 μm. Therefore, it would be reasonable if the CA powder loses the moisture easier than the membrane.

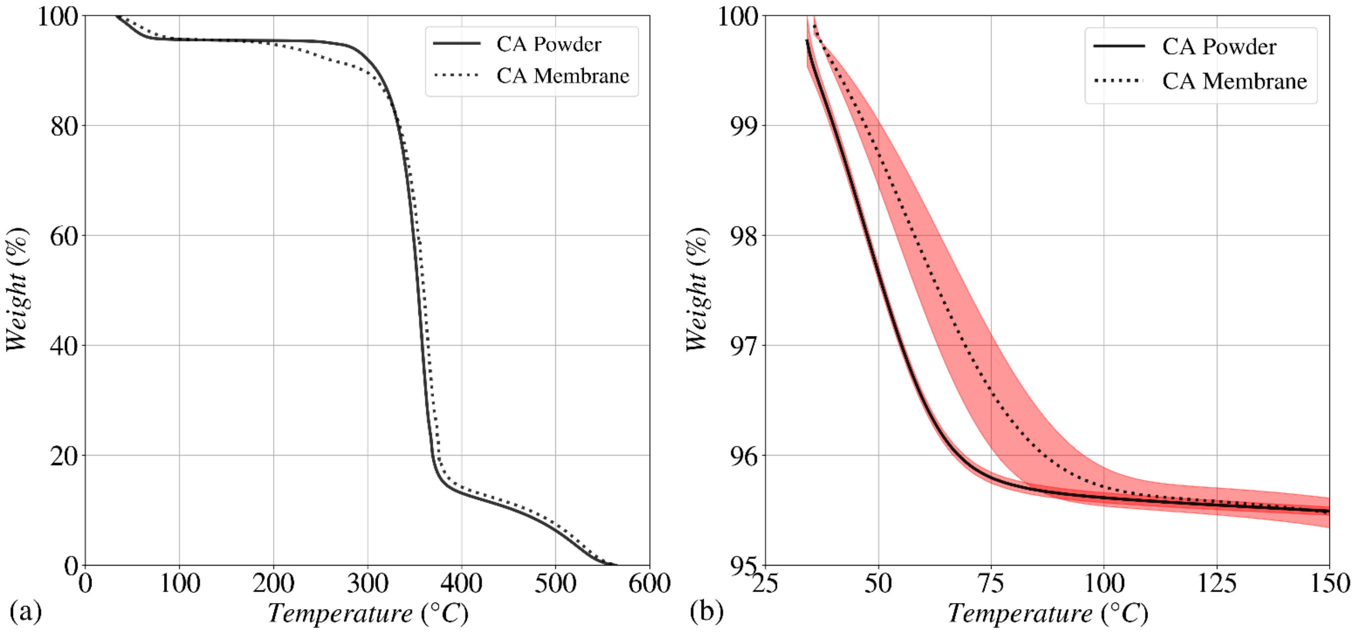

Figure 3. 9. Thermogravimetric analysis, a) the average normalized residual mass of CA powder and membrane (three specimens each), b) Detail of the normalized mass loss caused by water desorption together with standard error (semi-transparent area).

3.5 Mechanical characterization

In accordance with the project framework (Figure 2. 5), Young's modulus is one of the material's properties that must be used as an input for the numerical finite element model. Within the context of this research, two aspects of cellulose acetate membranes should be considered for the tensile mechanical behavior characterization. The first concerns the verification of an anisotropic behavior resulting from the membrane production procedure. Although the minimum velocity of casting knife movement was considered throughout the casting process of solution on glass with Doctor Blade (Figure 3. 6), yet, some unintended orientation may be possible. The second consideration, on the other hand, is related to the material's properties. Given that hygroscopic materials absorb moisture from their surroundings and that water molecules can plasticize polymeric materials [28–30], the humidity dependency of Young's modulus must be considered.

To verify any unintended anisotropy, tensile tests were performed on specimens cut out from the membrane along two mutually perpendicular directions, parallel and perpendicular to the direction of movement of the Doctor Blade knife. At least four rectangular specimens of 30×5 mm^2 were taken from the eligible region of the membranes in longitudinal and transverse direction. The thickness of the specimens varied in the range of 100 to 130 µm. A Dynamic Mechanical Analyzer (Ares RSA III, TA instruments®, 35 N cell) in tensile quasi-static mode was used to perform the tests. A gauge length of 10 mm has been considered for the tests. A constant linear displacement rate of 1 µm/s has been applied. Tests were conducted at 25 °C and at an almost constant relative humidity (RH = 38 ± 3 %). The load cell capacity of instrument is 35 N, tests were terminated when the axial force reached the value of 30 N which was before specimen failure as well.

Figure 3. 10 depicts the results of uniaxial tensile testing in longitudinal and transversal directions. For elongation more than 3%, a slight variation between the two directions can be observed. Within the 2 % elongation range in which the material behavior is linear, Young's modulus of 1.16 ± 0.06 GPa for the longitudinal direction and of 1.17 ± 0.09 GPa for the transversal direction has been determined.

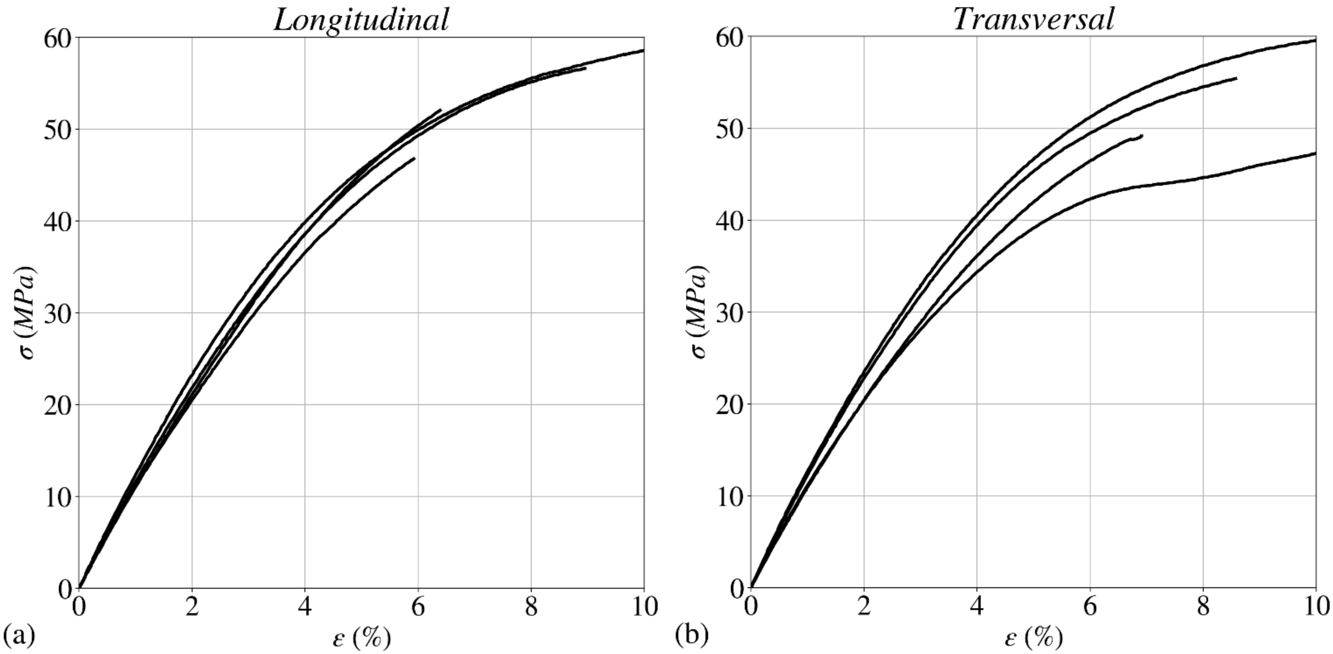

Figure 3. 10. Uniaxial tensile test of cellulose acetate membranes (RH=38%)

For the purpose of determining the effect of relative humidity on Young's modulus, a transparent polymethylametacrylate home-made water bath was used, which allows keeping the specimens immersed in water during the experimental procedure without interfering with the testing process. Specimens cut from membranes in two directions, transversal and longitudinal, were preliminarily submerged in distilled water at 25 °C for 24 hours, to let them to reach their saturation level of absorbed water. They were then placed between the jaws, which were immersed in distilled water. The uniaxial tensile tests were carried out at 25 °C at the same rate (1 μm/s).

Figure 3. 11 reports the average of four curves for the uniaxial tensile test, together with the standard error (semi-transparent shading), for cellulose acetate membrane in two conditions: saturated in water and in equilibrium at a relative humidity of 38%, in both directions (longitudinal and transversal). There is a distinct variation in trend of the behavior from the test in room relative humidity to the test performed in water. The membrane saturated at RH = 38% exhibits a brittle behavior. While, after 24 hours of immersion in distilled water, due to the plasticization of the membrane by water molecules, the mechanical properties of the

membrane change dramatically. The effect of material anisotropy is more visible in the water saturated membrane. Within the same strain range consider for the tensile tests in 38% relative humidity (2 %), the membrane's Young's modulus reduces to 0.75 ± 0.04 GPa in the longitudinal direction and 0.55 ± 0.3 GPa in the transverse direction.

The material anisotropy which is more evident in the results of the test performed in is the consequence of the membrane production procedure. Even though the casting knife of the Doctor Blade operated at the slowest possible speed, it seems the polymer chains aligned in the direction of the knife movement. This impact was not observed for the test in room condition. When membranes are saturated in water, they absorb the water; that plasticize the polymer leading to the observed loss of mechanical stiffness and strength. However, in this scenario, the water molecules change the distance between two polymer chains rather than modifying their conformation. As a result, the transversal modulus is smaller than the longitudinal one. Moreover, after 2% elongation, the plasticized membranes exhibit a long necking effect in both the longitudinal and transversal directions, which is explained by the orientation of the initially coiled polymer chains along the stress direction.

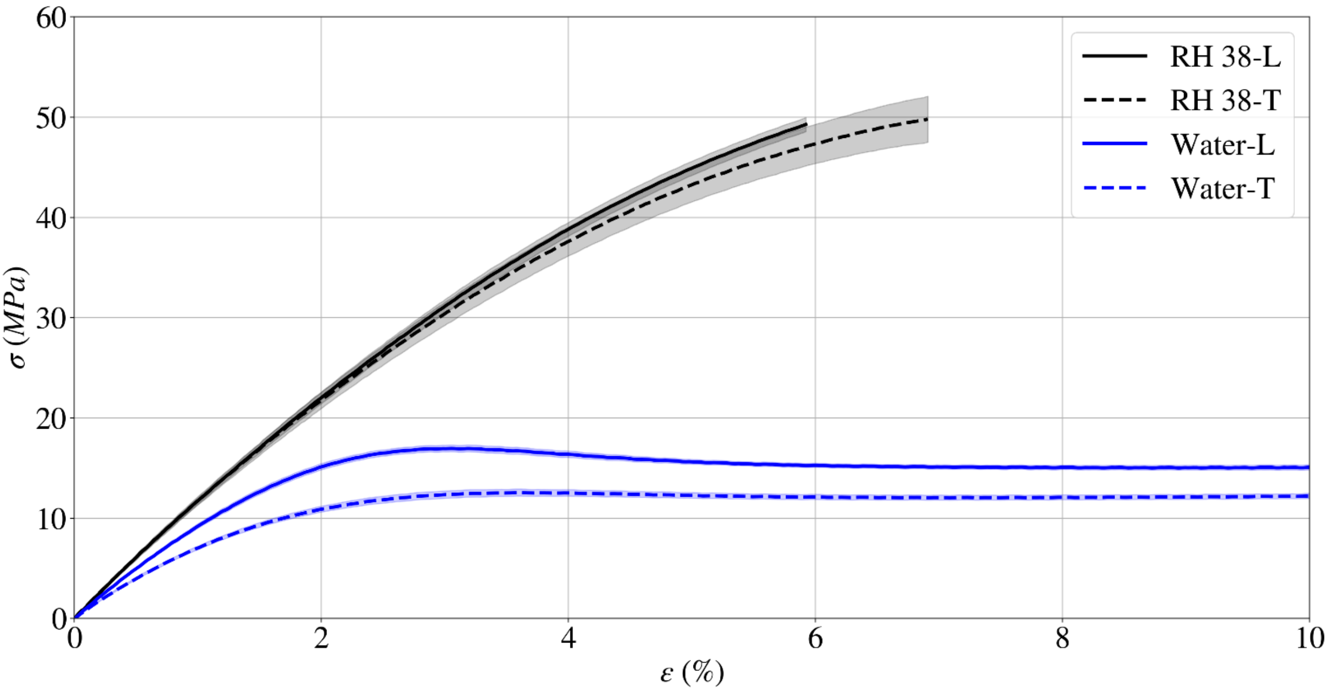

Figure 3. 11. Uniaxial tensile test of cellulose acetate membranes in different conditions (semi-transparent area indicates the standard error).

References

1. Heinze T, El Seoud OA, Koschella A. Cellulose Derivatives. Published online 2018. doi:10.1007/978-3-319-73168-1

2. Jonas R, Farah LF. Production and application of microbial cellulose. *Polym Degrad Stab*. 1998;59(1-3):101-106. doi:10.1016/S0141-3910(97)00197-3

3. Tarchevsky IA, Marchenko GN. *Cellulose: Biosynthesis and Structure*. Springer Berlin Heidelberg; 1991. doi:10.1007/978-3-642-75474-6

4. Zhou X, Lin X, White KL, et al. Effect of the degree of substitution on the hydrophobicity of acetylated cellulose for production of liquid marbles. *Cellulose*. 2016;23(1):811-821. doi:10.1007/s10570-015-0856-z

5. Crofton DJ, Pethrick RA. Dielectric studies of cellulose and its derivatives: 3. Glycerol in cellulose acetate. *Polymer (Guildf)*. 1982;23(11):1615-1618. doi:10.1016/0032-3861(82)90181-1

6. Zugenmaier P. 4. Characteristics of cellulose acetates 4.1 Characterization and physical properties of cellulose acetates. *Macromol Symp*. 2004;208(1):81-166. doi:10.1002/masy.200450407

7. Heinze T, Liebert T, Koschella A. *Esterification of Polysaccharides*. Springer-Verlag; 2006. doi:10.1007/3-540-32112-8

8. Candido RG, Godoy GG, Gonçalves A. Characterization and application of cellulose acetate synthesized from sugarcane bagasse. *Carbohydr Polym*. 2017;167:280-289. doi:10.1016/j.carbpol.2017.03.057

9. Saljoughi E, Sadrzadeh M, Mohammadi T. Effect of preparation variables on morphology and pure water permeation flux through asymmetric cellulose acetate membranes. *J Memb Sci*. 2009;326(2):627-634. doi:10.1016/j.memsci.2008.10.044

10. Kuo Y-N, Hong J. A new method for cellulose membrane fabrication and the determination of its characteristics. *J Colloid Interface Sci*. 2005;285(1):232-238. doi:10.1016/j.jcis.2004.10.043

11. De Carvalho Eufrásio Pinto M, David Da Silva D, Amorim Gomes AL, et al. Film based on magnesium

impregnated biochar/cellulose acetate for phosphorus adsorption from aqueous solution. *RSC Adv*. 2019;9(10):5620-5627. doi:10.1039/c8ra06655h

12. Rodríguez FJ, Galotto MJ, Guarda A, Bruna JE. Modification of cellulose acetate films using nanofillers based on organoclays. *J Food Eng*. 2012;110(2):262-268. doi:10.1016/j.jfoodeng.2011.05.004

13. Meier MM, Kanis LA, de Lima JC, Pires ATN, Soldi V. Poly(caprolactone triol) as plasticizer agent for cellulose acetate films: influence of the preparation procedure and plasticizer content on the physico-chemical properties. *Polym Adv Technol*. 2004;15(10):593-600. doi:10.1002/pat.517

14. Bai H, Zhou Y, Wang X, Zhang L. The Permeability and Mechanical Properties of Cellulose Acetate Membranes Blended with Polyethylene glycol 600 for Treatment of Municipal Sewage. *Procedia Environ Sci*. 2012;16:346-351. doi:10.1016/j.proenv.2012.10.049

15. Murtinho D, Lagoa AR, Garcia FAP, Gil MH. Cellulose derivatives membranes as supports for immobilisation of enzymes. *Cellulose*. 1998;5(4):299-308. Accessed March 17, 2021. https://link.springer.com/article/10.1023/A:1009255126274

16. Medina-Gonzalez Y, Aimar P, Lahitte J-F, Remigy J-C. Towards green membranes: preparation of cellulose acetate ultrafiltration membranes using methyl lactate as a biosolvent. *Int J Sustain Eng*. 2011;4(1):75-83. doi:10.1080/19397038.2010.497230

17. Nolte MCM, Simon PFW, del Toro MA, Gerstandt K, Calmano W. Cellulose Acetate Reverse Osmosis Membranes Made by Phase Inversion Method: Effects of a Shear Treatment Applied to the Casting Solution on the Membrane Structure and Performance. *Sep Sci Technol*. 2011;46(3):395-403. doi:10.1080/01496395.2010.521231

18. Al-Ahmed A, Mohammad F, Zaki Ab. Rahman M. Composites of polyaniline and cellulose acetate: preparation, characterization, thermo-oxidative degradation and stability in terms of DC electrical conductivity retention. *Synth Met*. 2004;144(1):29-49. doi:10.1016/j.synthmet.2004.01.007

19. Devarayan K, Lei D, Kim H-Y, Kim B-S. Flexible transparent electrode based on PANi nanowire/nylon nanofiber reinforced cellulose acetate thin film as supercapacitor. *Chem Eng J*. 2015;273:603-609. doi:10.1016/j.cej.2015.03.115

20. Son WK, Youk JH, Lee TS, Park WH. Preparation of antimicrobial ultrafine cellulose acetate fibers with

silver nanoparticles. *Macromol Rapid Commun*. 2004;25(18):1632-1637. doi:10.1002/marc.200400323

21. Zavastin D, Cretescu I, Bezdadea M, et al. Preparation, characterization and applicability of cellulose acetate–polyurethane blend membrane in separation techniques. *Colloids Surfaces A Physicochem Eng Asp*. 2010;370(1-3):120-128. doi:10.1016/j.colsurfa.2010.08.058

22. Wu S, Qin X, Li M. The structure and properties of cellulose acetate materials: A comparative study on electrospun membranes and casted films. *J Ind Text*. 2014;44(1):85-98. doi:10.1177/1528083713477443

23. Solvent selector chart Active solvent a CAS number Evaporation rate Formula Dilution ratio b Blush resistance % RH @ 80°F Specific gravity @ 20°C/20°C. Published 2020. Accessed February 15, 2022. https://www.eastman.com/Brands/Eastman_Solvents/Pages/Resources.aspx

24. Ohring M. *The Material Science of Thin Films*. Aademic Press; 1992.

25. Freund LB, Suresh S. *Thin Film Materials Stress , Defect Formation and Surface Evolution*.; 2003. http://scholar.google.com/scholar?hl=en&btnG=Search&q=intitle:Thin+Film+Materials#2

26. Wong CP. *Moisture Sensitivity of Plastic Packages of IC Devices*. (Fan XJ, Suhir E, eds.). Springer US; 2010. doi:10.1007/978-1-4419-5719-1

27. Boy RE, Schulken RM, Tamblyn JW. Crystallinity in secondary cellulose esters. *J Appl Polym Sci*. 1967;11(12):2453-2465. doi:10.1002/app.1967.070111205

28. Bonnaillie L, Tomasula P. Application of Humidity-Controlled Dynamic Mechanical Analysis (DMA-RH) to Moisture-Sensitive Edible Casein Films for Use in Food Packaging. *Polymers (Basel)*. 2015;7(1):91-114. doi:10.3390/polym7010091

29. Dingler C, Müller H, Wieland M, Fauser D, Steeb H, Ludwigs S. From Understanding Mechanical Behavior to Curvature Prediction of Humidity-Triggered Bilayer Actuators. *Adv Mater*. 2021;33(9). doi:10.1002/ADMA.202007982

30. Nolte AJ, Treat ND, Cohen RE, Rubner MF. Effect of relative humidity on the Young's modulus of polyelectrolyte multilayer films and related nonionic polymers. *Macromolecules*. 2008;41(15):5793-5798. doi:10.1021/ma800732j

31. Surface Energy Data for Cellulose acetate, CAS # 9004-35-7. Accessed February 19, 2022.

http://www.accudynetest.com/polymer_surface_data/cellulose_acetate.pdf

4 Moisture Diffusion

The moisture transport in hygroscopic materials is presented in this chapter. The procedure for gravimetric measurements of moisture absorption in cellulose acetate membrane in variation of humidity level is provided. The non-Fickian sigmoidal diffusion observed in cellulose acetate is described analytically using the variable surface concentration model. Material properties such as relaxation factor (β) and moisture diffusion coefficient (D) are evaluated. The moisture concentration at saturation (C_{sat}) is determined as a function of environment relative humidity at constant room temperature. The details of a sigmoidal diffusion finite element modeling are provided.

4.1 Moisture diffusion kinetic in hygroscopic materials

As stated in Section 2.5, for the description of a material hygroscopic behavior, two key factors must be taken into consideration: the quantity of moisture absorbed by the material from the environment and the associated deformation. Herein, the fundamental aspects of moisture diffusion and concentration at equilibrium in hygroscopic materials are discussed.

The majority of studies on the mechanism of moisture diffusion in polymeric materials conducted over the last seventy years confirm that for many polymers, the concentration-dependent form of Fick's law with constant boundary conditions and diffusion coefficient is ineffective in providing an appropriate interpretation of this complex process [1]. The general solution of diffusion considers a wide range of initial and boundary conditions to simplify the mathematical and theoretical formulation required to calculate the constant diffusion coefficient. However, in some polymers, diffusive material penetration might produce chemical reactions, heat production, or alter the mobility of polymer molecules [1]. In these scenarios, the formal Fickian solution is no longer valid, and alternative forms of boundary conditions must be created by introducing new variables.

In this context, Crank and Park [2] explored several diffusion anomalies and offered analytical models to describe the experimental results, such as the diffusion process in glassy polymers with sharp observed boundaries through the thickness that occurs by vapor absorption between the glassy dried polymer and the softened polymer [1], which is related to the combination of mechanical and physical effects of the diffusive substance on the membrane. Based on the relative diffusion and polymer relaxation (induced by diffusive substance) rates, Alfrey et al. [3] categorized diffusion in polymers into three distinct behaviors: Fickian behavior, non-Fickian behavior, and Case II behavior. Mensitieri et al. [4] divided the mass transport phenomenology into four categories based on the same principles, which also defines polymer’s sorption ability.

Figure 4. 1 depicts a schematic representation of mass transport phenomena in polymers, spanning from Fickian to case II behavior presented by Mensitieri et al. [4], as well as Crank's [1] absorption and desorption trend for each phenomenology. Based on the presented phenomenology for uptake property and the plasticization effect of the absorbed moisture in glassy polymers, inducing polymer relaxation and lowering the glass transition temperature [5], the polymeric materials can be subdivided into three categories from the hygroscopic behavior point of view:

- ***Non-hygroscopic materials:*** those in which the rate of moisture diffusion in the polymer is substantially slower than the rate of polymer relaxation. Thus, after a short period of exposure to a humid environment, the material glass transition temperature, T_g, is still greater than the environment temperature ($T_g > T_{Env.}$). By completion of the diffusion process over a long period of time (reaching the saturation state over years), the T_g reaches the environment temperature or even drops below it [1,4]. These materials exhibit formal Fickian behavior with no deformation due to the moisture absorption.
- ***Moderate-hygroscopic materials:*** these materials exhibit dual-stage [6–8], or pseudo-Fickian [1] behavior, depending on the porosity of the material's structure and reversibility of the moisture absorption phenomena. They have a comparable moisture diffusion and relaxation rates, and the time required for these materials to attain saturation ranges from days to months.
- ***Highly-hygroscopic materials:*** these materials have a diffusion rate significantly higher than relaxation and a very high level of mass absorption. Moisture absorption causes an instantaneous expansion in the borders of the material's body, resulting in sigmoidal diffusion behavior [2,9]. Saturation time for these materials varies between minutes and hours.

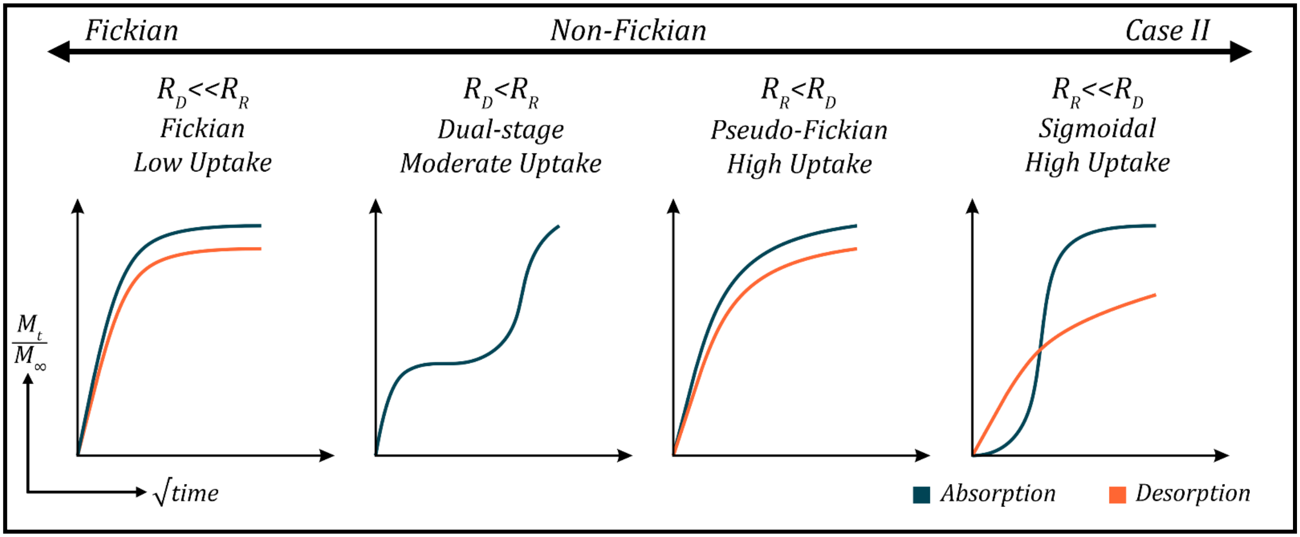

Figure 4. 1. Schematic representation of mass transport phenomenology for absorption and desorption in polymers, adapted from [1] and [4], where R_D is the diffusion rate and R_R is the relaxation rate.

It should be noted that a material's diffusion behavior is highly reliant on the diffusive substance as well. For instance, chloroform, water vapor and acetone demonstrate different absorption process by cellulose acetate. In the case of acetone, the sorption process has a two-stage diffusion as the polymer surface reached a quasi-equilibrium condition, followed by a rise in surface concentration [6]. In the case of chloroform [10] and water vapor [11,12] absorption, variations in surface concentration cause swelling at the surface. This phenomenon manifests itself as the variation (expansion) of the boundary condition of Fickian law in the context of diffusion and exhibits a sigmoidal trend. According to the presented classification and well-known hygroscopic properties of cellulose-based materials, a sigmoidal diffusion trend for moisture absorption of the cellulose acetate membranes is expected.

For a Fickian behavior, the diffusion coefficient (D) is approximated using a simplified version of the general Fickian law as $\frac{C_t}{C_\infty} = \frac{M_t}{M_\infty} = 4\sqrt{\frac{D.t}{\pi h^2}}$, $C = \frac{M}{V}$, where, M_t and M_∞ are the moisture mass at time t and at saturation, respectively. This property may be evaluated graphically by a linear fitting of the experimental data generating the $M_t\ /M_\infty$ ratio plotted as a function of the square root of the absorption time ($\sqrt{time}$), within the first half of absorption process ($\frac{M_t}{M_\infty} < 0.5$) [8]. As seen in Figure 4. 1, this strategy is ineffective when dealing with sigmoidal and dual-stage diffusion trends.

To characterize the moisture diffusion process of moisture-sensitive materials, various analytical models have been proposed. In some investigations, the kinetics of the absorption and desorption processes were believed to be the same, and the diffusion coefficient was calculated using desorption measurements and applied to the absorption process [8]. However, the kinetics of moisture absorption and desorption are fundamentally different, in particular for highly-hygroscopic materials with sigmoidal diffusion behavior, as depicted in Figure 4. 1. Employing the rate of moisture-induced molecular relaxation, Roussis [11] established a model that was able to fit the experimental results for membranes based on thickness variation. Based on both Mensitieri [4] classification and Cranks' theoretical investigations [1], De Wilde and Shopov [7] proposed a model to describe sigmoidal and dual-stage diffusion by dividing the diffusion process into short-time and long-time phenomena.

In this context, the so-called "*advancing boundaries*" [1] refers to the condition that the diffusive substance penetration (moisture in this research) generates a deformation on the surface of the membrane, which might also modify the characteristics of the material at the surface. As previously depicted in Figure 2. 1, water molecule penetration in cellulose-based materials at the molecular level affects the distance between molecules or polymer chains by forming hydrogen bonds with hydroxyl groups and disrupting the interchain connection in the polymer. The swelling of the surface layer imposes an internal stress between the plasticized surface and the membrane's dry glassy core [7]. Moreover, water molecules play the role of polymer plasticizers lowering the glass transition temperature. As the molecular mobility at the surface of the membrane increases, the mechanical characteristics of the polymer vary within the membrane thickness. The relaxation generated by moisture absorption on the surface layer, as well as the required time for polymer molecule stabilization explain the sigmoidal trend of the moisture absorption in cellulose acetate [1,2,7].

For "*advancing boundaries*" conditions, the "*strain-dependent model*" [1,2,9] offers a stepwise diffusion coefficient for the transition from a glassy state to a rubbery one in the membrane, by interpreting the diffusion process in terms of time and concentration. By assuming the same diffusion law but a different relaxation time for the material at the surface layer of the membrane in a specific initial condition of a completely dry membrane ($C_{initial} = 0$), the concentration of this layer approaching its saturation exponentially can be represented according to Equation (4.1) Where C_t , C_{sat}, and β are the concentration at time t, concentration at saturation and the relaxation factor, respectively.

$$C_t = C_{sat}\left(1 - e^{-\beta t}\right) \tag{4.1}$$

This concentration yields to the "*variable surface concentration model*" [1], presented in Equation (4.2) as detailed in literature [1,2,9] $\left(\beta \neq (2n+1)^2\left(\frac{D\pi^2}{4l^2}\right)\right)$, that describes the sigmoidal moisture diffusion of cellulose acetate membranes.

$$\frac{M_t}{2lC_{Sat}} = 1 - e^{-\beta t}\,.\sqrt{\frac{D}{\beta l^2}}\,.\tan\left(\sqrt{\frac{\beta l^2}{D}}\right) - \sum_{n=0}^{\infty}\frac{8}{\pi^2}.\frac{\exp\left(-\frac{(2n+1)^2\pi^2\,Dt}{4l^2}\right)}{(2n+1)^2\left\{1-(2n+1)^2\left(\frac{D\pi^2}{4\beta l^2}\right)\right\}} \tag{4.2}$$

In this model, M_t and l are the absorbed moisture mass per membrane unit area at time t and membranes' half-thickness $(l = h_a/2)$, respectively. It must be noted that, the constant diffusion coefficient D, here, is neither the slope of early stage of absorption nor the middle stage of absorption. For this analytical model (Equation (4.2)), a parametric analysis on the influence of each variable is provided in Appendix 4. 1 .

4.2 Gravimetric measurements

As mentioned in the project framework (Section 2.7), gravimetric measurement technique or direct weighing has been selected for the characterization of moisture absorption in CA membrane. Membranes with thickness ranging from 66 ± 1.5 to 200 ± 0.5 μm were produced via the optimized membrane preparation procedure previously described. The resultant membranes were then punched into square specimens of 30 mm ×30 mm (900 mm^2).

Even though the standard protocol for moisture content determination of un-plasticized cellulose acetate (BS EN ISO 585:1999) recommends drying cellulose acetate (regardless of its physical form) for 3 hours at 105 °C, drying has not been completed even after 6 hours in the recommended settings. Hence, each specimen, together with its container, was dried in an oven at 125 °C for 24 hours (Mazzali Thermair). The container was then sealed and kept in a desiccator (containing dried silica gels) for two hours at room temperature.

An AS310.R2 (RADWAG) balance with a resolution of 0.1 mg was used for all the gravimetric measurements. Even if the climatized room provides homogenous air conditioning with no direct airflow, the side doors of the balance were kept closed during the test to avoid further airflow influence if any. Instead, the top door of the balance was left open to maintain the humidity of the balance at the same level as the climatized chamber. To eliminate errors caused by the sample holder's weight, the dried specimens were placed directly in the middle of the balance weighing pan.

The environmental conditions for the balance (RADWAG, AS310.R2) to provide an accurate read value are a relative humidity of below 80% and a temperature within the range of 10 to 40 °C. Therefore, measurements were performed in a climatized room at 25 ± 1 °C and at constant values of relative humidity ranging between 21 and 76%. A polymethylametacrylate close chamber was designed and built to achieve a stable relative humidity beyond the range of the climatized room (RH = 40 – 50%). This closed chamber covered the balance and a container of dry silica gels (RH = 20 - 40%) or salt solutions of sodium chloride in distilled water (2/1 w/w, RH = 74 - 76%) allowed to have various relative humidity levels. The moisture mass variation of preliminarily dried cellulose acetate membranes over time was monitored.

Table 4. 1 details specimen thickness (h_a), test humidity levels (RH), and the number of dry CA specimens tested measurements for each thickness and relative humidity.

Table 4. 1. Details of gravimetric measurement specimen and condition

$RH(\%)$ $h_a\ (\mu m)$	21	30	37	38	39	40	44	50	52	53	74	75	76
66 ± 1.5	_	2	1	3	_	4	2	2	1	1	1	_	1
161 ± 7	1	_	_	_	1	_	_	_	_	1	_	1	1
171 ± 6	1	1	_	1	1	1	1	1	1	_	_	1	_
200 ± 10.5	_	1	2	_	_	2	1	1	_	1	1	_	_

Regardless of the kinetics of diffusion (Fickian, non-Fickian, mode II), the time required for a sample to get the saturation concentration is a function of sample thickness. Thinner membranes attain saturation concentration faster than thicker membranes [8]. Therefore, depending on the thickness of the specimens, the moisture absorption measurements monitoring time varied. The absorption process was regarded as completed when moisture gain rate was below 10^{-9} (g/mm^{3}s).

Figure 4. 2 shows the experimental outcomes for some gravimetric measurements to demonstrate repeatability and illustrate the influence of thickness and relative humidity. As expected, regardless of membrane thickness or humidity level, all curves follow a sigmoidal trend. The complete experimental data are available in Appendix 4. 2. The experimental results on moisture absorption in two specimens with a thickness of 66 ± 1.5 μm and a relative humidity of 40% are shown in Figure 4. 2 (a), which was repeated twice on each specimen, after drying following the same procedure described above. The absorption rate of the dry membrane's is slow for the first 50 seconds of exposure ($\sqrt{time}$ ≈ 7), but rapidly increases until 10 minutes ($\sqrt{time}$ ≈ 25) and then levels off after 15 minutes of exposure ($\sqrt{time}$ ≈ 30). Figure 4. 2 (b), on the other hand, highlights the influence of membrane thickness on the trend, which is completely consistent with the pattern shown in Appendix 4. 1 (a). The thinner the membrane, the higher the moisture content for any exposure period before saturation. The comparison of the moisture concentration between Figure 4. 2 (a) and (b) for what concerns the membrane with a thickness of 66 ± 1.5 μm suggests that, starting from dry condition, the environmental humidity does not have an impact on the amount of moisture uptake for exposure times up to around 225 seconds ($\sqrt{time}$ ≈ 15). However, by approaching the saturation state, the amount of absorbed moisture and its asymptotic value concentration at saturation increases by the relative humidity increment. For instance, the time required for this membrane to reach saturation at RH = 40 % is about 10 minutes ($\sqrt{time}$ ≈ 25) with a value of $C_{sat} = 3.2\times10^{-}$

^{5} g/mm^3, while these quantities increase to 15 minutes ($\sqrt{time} \approx 30$) and C_{sat} = 3.5×10^{-5} g/mm^3 for RH = 50 %.

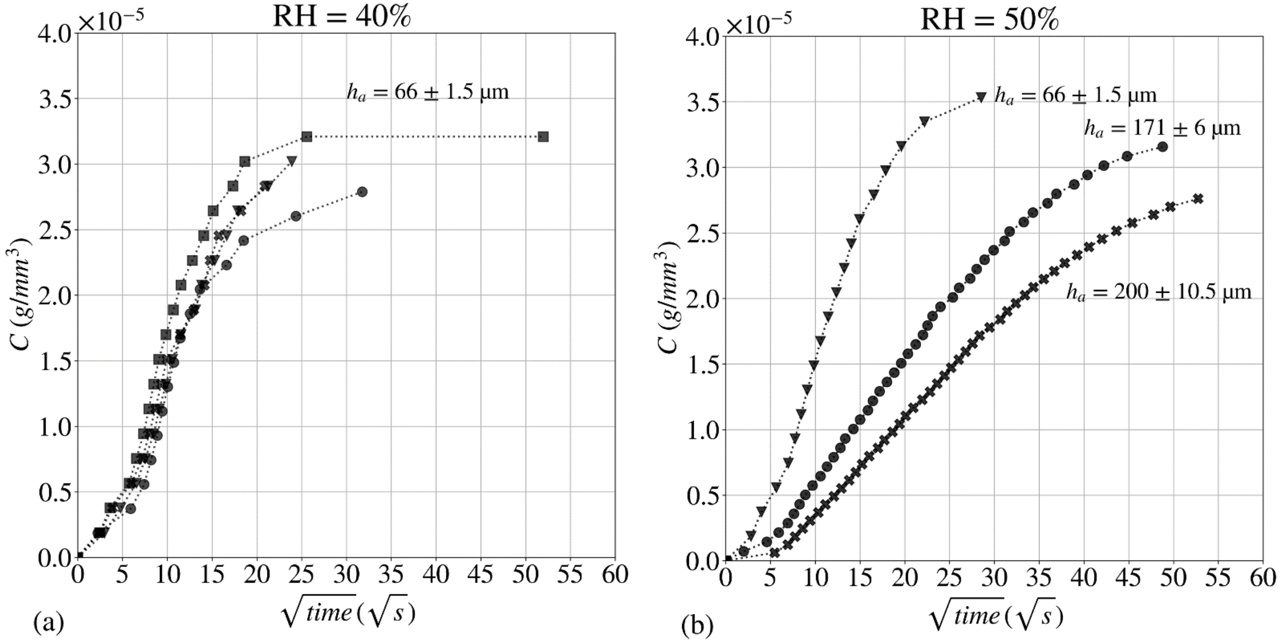

Figure 4. 2. Some experimental results for gravimetric measurements a) Repeatability of moisture absorption for a membrane with a thickness h_a = 66 ± 1.5 µm at 40 % relative humidity, b) The membrane's moisture absorption at 50 % RH for various thicknesses.

4.3 Analytical model

The so-called "*variable surface concentration*" model presented by Crank [1] (Equation (4.2)) is used to analyze the sigmoidal diffusion of moisture in cellulose acetate membranes. An algorithm using the least squared technique was developed to determine the parameters C_{sat}, β , and D using the best fitting of the gravimetric experimental data by the analytical model (Equation (4.2)), see Appendix 4. 3 . The fitted model's accuracy was assessed using the "*R-scored*" approach (R^2). The optimal parameters of C_{sat}, β, and D with $R^2 > 0.95$ were determined by the best fitting of the analytical model to all the experimental data.

Figure 4. 3 depicts the evolution of moisture concentration vs. the square root of time, resulted from the best fitting of the analytical model to the experimental data for the specimens presented in Figure 4. 2 (b). Although there is a slight discrepancy between the analytical model and the experimental data at the very early stage of the absorption process ($\sqrt{time} = 5$ √s) for the membrane with a thickness of 66 ± 1.5 μm, the analytical model accurately describes the sigmoidal trend of the absorption curve, also for other specimens. The analytical models' precise fitting can forecast a variety of aspects, including the time of the sigmoidal curve inflection point, the concentration at saturation, the time required to reach the equilibrium stage (saturation), and the slope of the long-term sorption phase (linear part).

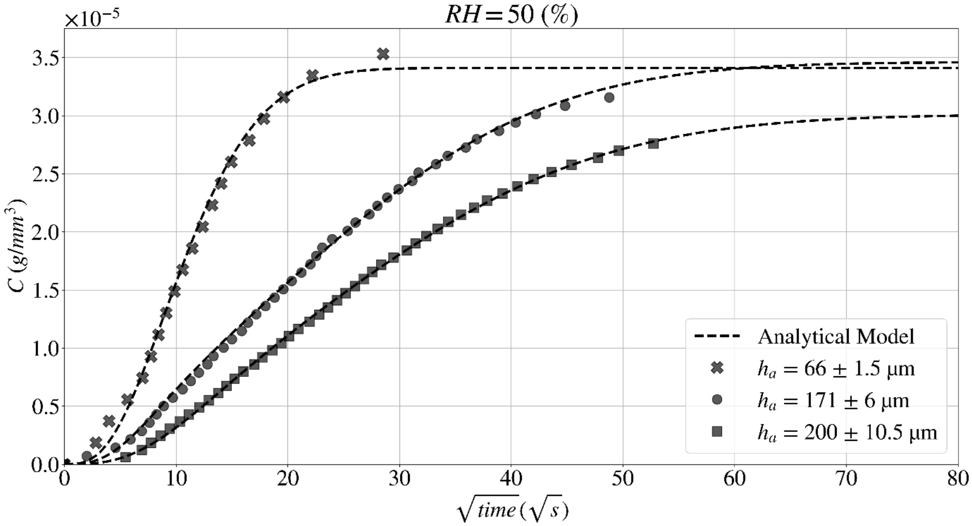

Figure 4. 3. Analytical model interpolation of moisture absorption experimental data obtained at RH=50% with three membranes different in their thickness.

Appendix 4. 4 provides a full table of the results (β, D, C_{sat}, and R^2) as a function of relative humidity and membrane thickness. Figure 4. 4 illustrates the material characteristics β and D resulted from by best fitting of the experimental data by the analytical model for each moisture absorption experiment as a function of relative humidity for different membrane thickness. The obtained values for relaxation factor (β) vary from 0.009 to 0.046 s^{-1} with a mean value of 0.026 s^{-1} and the standard deviation of 0.013 s^{-1} (Figure 4. 4 (a)). There is no discernible trend in the dispersion of the relaxation factor (β), neither in terms of thickness variation nor relative humidity. Given the negligible effect of relaxation factor variation within the range 0.01 and 0.1 s^{-1} on the early stage of the sigmoidal trend (see Appendix 4. 1 (c)), the scatter of 0.013 s^{-1} is not significant and we can consider β constant with the mentioned mean value. The obtained values for the diffusion coefficient (D), on the other hand, are in a tighter fluctuation region than the relaxation factor (β), varying within the range of 1.59×10^{-6} and 4.15×10^{-6} mm^2/s. The mean value of $3.35\times10^{-6} \pm 5.45\times10^{-7}$ mm^2/s has been considered for the diffusion coefficient (Figure 4. 4 (b)).

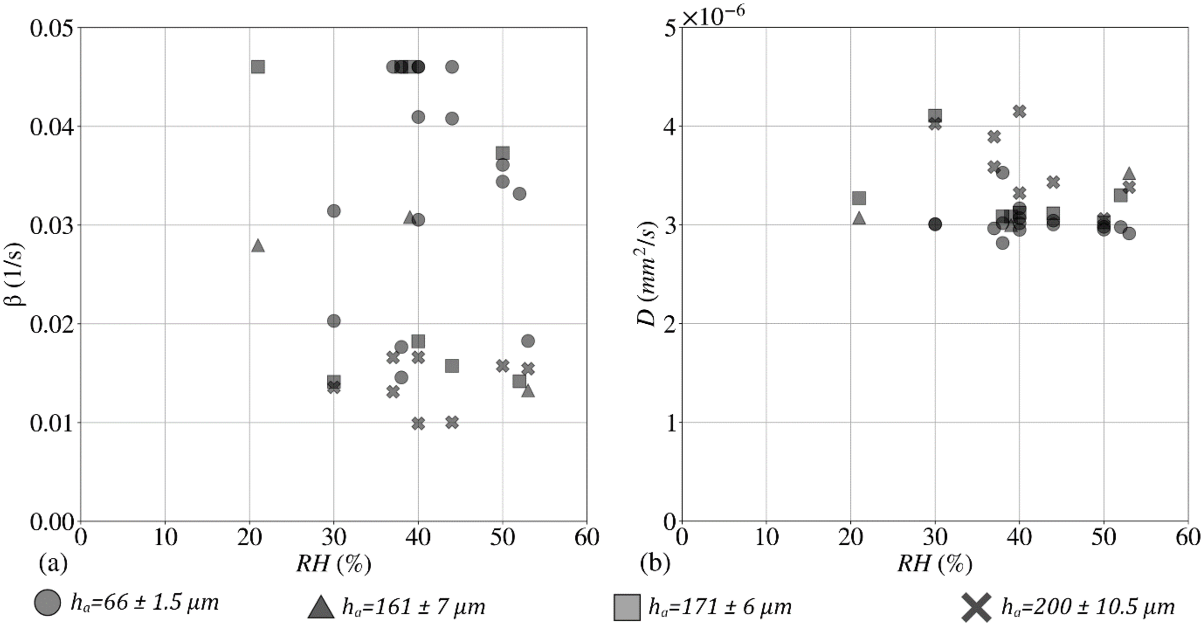

Figure 4. 4. Determined values by the best fitting of the analytical model to the experimental data for, a) Relaxation constant (β), b) Diffusion coefficient (D).

Figure 4. 5 reports the average values of moisture concentration at saturation (C_{sat}), obtained by the best fitting of the experimental data from membranes with different thicknesses, as a function of relative humidity (RH). For most materials, it is believed that, at a constant temperature, the water partial vapor pressure at saturation (p_{sat}) and the water vapor solubility (S) are not affected by the relative humidity. This means that the moisture concentration at saturation (C_{sat}) has a linear relationship with the relative humidity of the environment ($C_{sat} = (S \times p_{sat}) \times RH$) [8,13]. Figure 4. 5 shows, however, that this notion is not applicable to the cellulose acetate membranes studied.

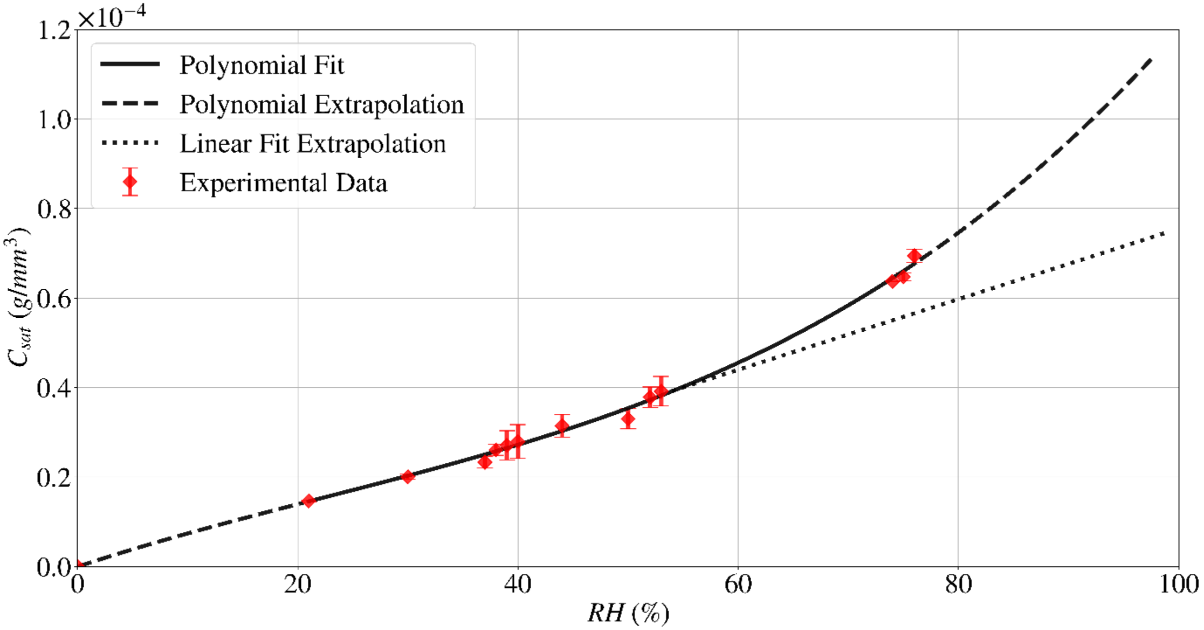

Figure 4. 5. Average moisture concentration at saturation (C_{sat}) as a function of relative humidity (RH) (bars represent the standard deviation).

According to the literature, highly hygroscopic materials [14], in particular cellulose-based materials [15–19] diverge from this linear prediction, exhibiting a significant difference at a specific threshold of relative humidity. The rise in the slope of the C_{sat} vs. RH curve and the humidity level at which this increase occurs depend on a number of factors, including the kind of cellulose and its degree of crystallinity, the acetylation process, and the presence of plasticizers or other chemical components [20]. For the considered cellulose acetate, this turning point is at a humidity level of above 53%. For instance, the concentration at saturation at a relative humidity of 76% is about 7×10^{-5} (g/mm^3), while the predicted value with the so-called linear relation estimates a value of about 5.5×10^{-5}(g/mm^3), which is a considerable underestimation.

The experimental results reveal a behavior comparable to that of other cellulose-based materials described in the literature [15–19], which can be interpolated using a polynomial function. Therefore, the experimental result presented in Figure 4. 5 was fitted by a third-order polynomial function assuming at completely dry condition (RH = 0 %) the concentration C_{sat} = 0 g/mm^3. Equation (4.3) describes the obtained function with *R-scored* value of 0.996.

$$C_{sat} = 1.19 \times 10^{-10} \times RH^3 - 7.97 \times 10^{-9} \times RH^2 + 8.09 \times 10^{-7} \times RH \tag{4.3}$$

4.4 Finite Element Modeling

Many studies, particularly those devoted to integrated circuit packaging for semiconductor device manufacturing [8], consider the diffusion process during absorption to be equivalent to the diffusion process during desorption. Consequently, the simulation of moisture diffusion is mainly confined to formal Fickian behavior. Few studies have attempted to replicate non-Fickian diffusion behavior [21,22]. They have simulated diffusion during desorption and computed residual moisture content. Despite the typical sigmoidal diffusion of cellulose-based materials, the diffusion behavior was considered as a formal Fickian [19], which resulted in a simulation with a poor degree of accuracy.

In this research, COMSOL Multiphysics ® 5.6 was used to build a finite element model. Figure 4. 6 (a) portrays the 3D prismatic geometry utilized for the discretization of three samples with dimensions of 1×1× thickness (mm^3). From the “Chemical transport interface”, the time-dependent model "Transport of Diluted Species," which is diffusion based on Fick's law, has been used.

This algorithm employs the convection transport mechanism with linear discretization of concentration and, to the best of the authors' knowledge, cannot simulate the sigmoidal non-Fickian behavior. Therefore, some values such as β = 0.026 (1/s) and D = 3.35×10^{-6} (mm^2/s) obtained by fitting the experimental findings using the analytical model and C_{sat} (g /mm^3) were employed as parallel inputs in the global definition [23].

The initial value of moisture concentration in the membrane was set to zero (C_0= 0) since the experiments was started from a fully dry membrane. The concentration at saturation C_{sat} was defined as function of relative humidity (RH) according to Equation (4.3). The no flux boundary condition was applied to the membrane's four thickness surfaces, and the concentration boundary condition was applied to the membrane's two lateral surfaces. As previously stated in this chapter, the effect of sigmoidal behavior derives from the immediate expansion of the surface layer of the membrane by the absorption of moisture from the environment and the membrane reaches its ultimate concentration exponentially by the function of $C_t = C_{sat}\left(1 - e^{-\beta t}\right)$ (Equation(4.1)). Hence, for the simulation of sigmoidal behavior, this function was used for the concentration by referencing the parameters provided in the global definition, rather than a constant boundary condition with the value of C_{sat} like in Fickian behavior.

From one lateral surface to the other, a user-controlled, general physics sweeping mesh with quadrilateral face over a straight-line path was applied, resulting in a discretized volume with hexahedral elements. This method gave a sufficient distribution of elements, 20 along the thickness and 10×10 on the surface (total of 2000 elements), while minimizing calculation time. The thickest sample achieved the moisture concentration at saturation after roughly 90 minutes (5400 s) based on the experimental results. Therefore, the diffusion process was modelled up to 6400 s with a time increment of 2 seconds.

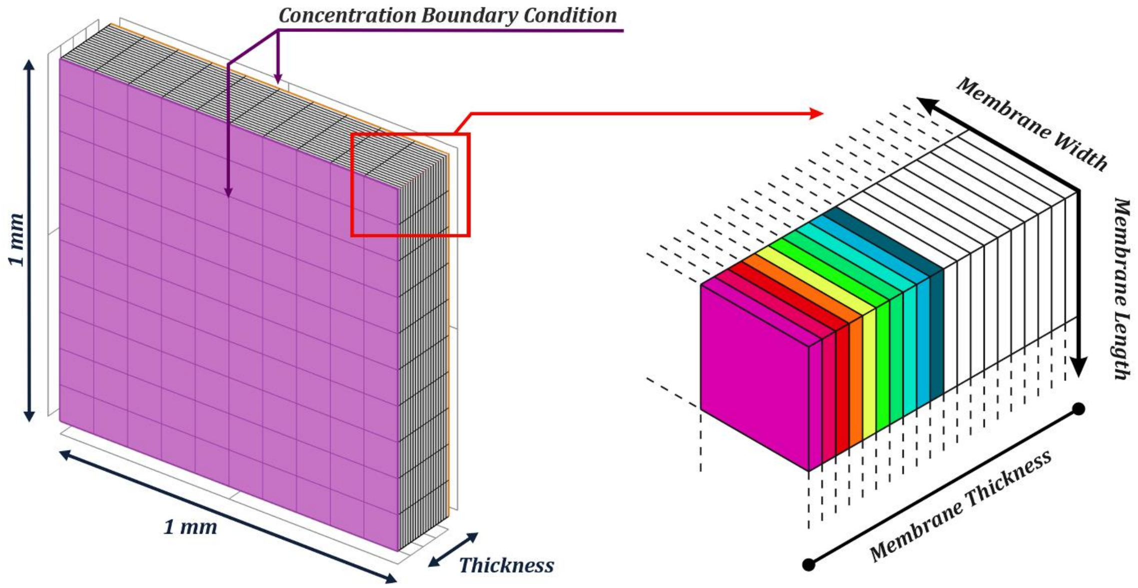

Figure 4. 6. Finite element model: (a) Specimen dimensions, discretization, and boundary conditions; (b) elements for monitoring concentration at each time increment.

The concentration at each time increment was extracted for the elements shown in Figure 4. 6 (b) to gain a better insight into the development of concentration in time along the thickness. Finally, the average concentration in volume was calculated as a function of the square root of time for each time increment.

The impact of the proposed exponential function on the diffusion process through the thickness provides a first insight into the quality of the numerical model. For this aim, a specimen with a thickness of 200 μm was simulated twice, once with Fickian behavior and once with the approach provided here for sigmoidal diffusion at a relative humidity of 50%. As the moisture diffusion is symmetric respect to the midplane, herein, the outputs were detailed using only half of the elements (10 elements), presented by the colored elements in Figure 4. 6 (b)).

The short-time absorption process for the membrane with a thickness of 200 μm, as demonstrated in Figure 4. 2 (b), is less than 100 seconds ($\sqrt{time}$ =10). Therefore, Figure 4. 7 illustrates the development of concentration versus thickness over the first 100 seconds for both Fickian and non-Fickian diffusion with 5-second time intervals. From the beginning of the moisture absorption process (t = 0 s) the surface element in the Fickian behavior simulation reaches its concentration at saturation (3.45×10^{-5} g/mm^3) immediately. As a result, moisture diffuses across the thickness beginning with this concentration at saturation. For the non-Fickian behavior simulation, at the beginning of the diffusion process the concentration is zero, as at time zero the Equation (4.1) yields zero. As can be observed, the concentration at the surface and across the thickness for non-Fickian diffusion rise concurrently with time. Even after 100 seconds, the surface element modelled with non-Fickian behavior has not reached saturation concentration. This delay has an impact on the entire process of moisture absorption and is responsible for the progressive shift in the slope of the sigmoidal curve that was seen experimentally in the first stages of the moisture absorption process. An example of the non-Fickian diffusion behavior across the membrane's thickness for different thicknesses is provided in Appendix 4. 5.

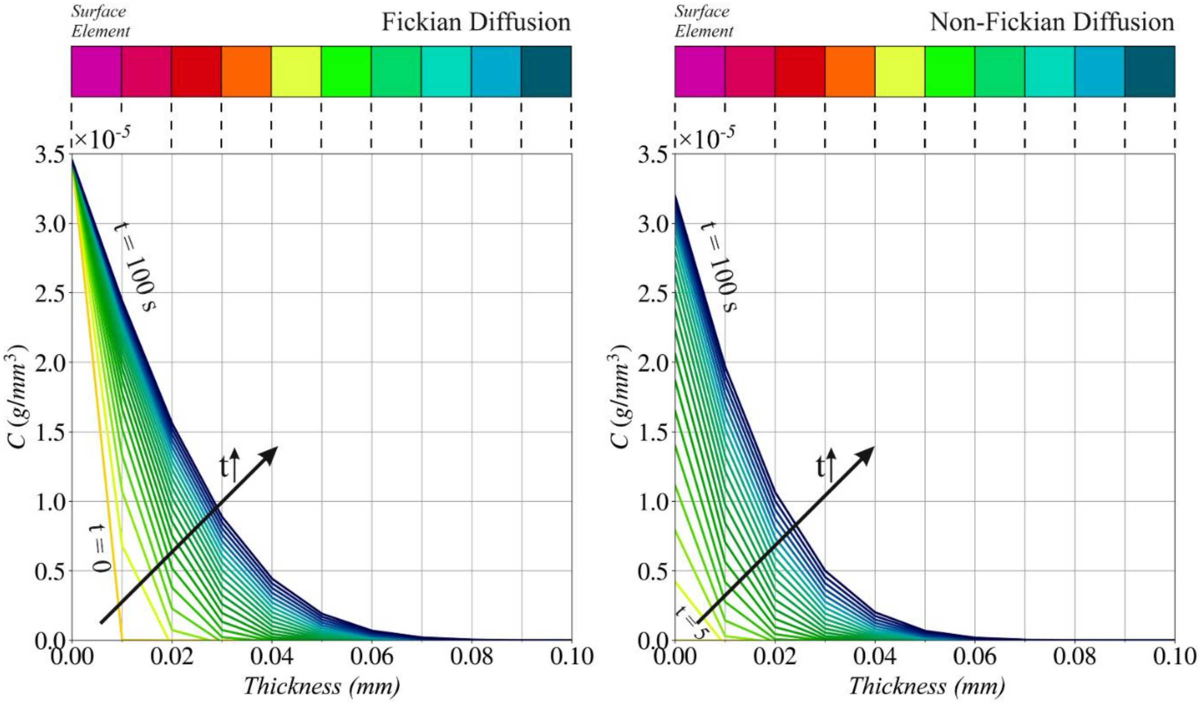

Figure 4. 7. Simulation of moisture diffusion over thickness using Fickian (left) and non-Fickian (right) behavior, each curve represents a time interval of 5 seconds.

To ensure that the developed finite element model can accurately describe the sigmoidal diffusion of cellulose acetate membranes during the moisture absorption process, three specimens whose absorption curve are shown in Figure 4. 2 (b) were simulated twice, once with a model in which the values obtained for β, D and C_{sat} from the fitting procedure for each experiment (Set 1) and once with their mean values (Set 2) evaluated across all experimental results see Table 4. 2.

Table 4. 2. Finite element simulation inputs

$RH(\%)$	$h_a\ (mm)$	$\beta\ (1/s)$	$D\ (mm^2/s)$	$C_{sat}\ (g/mm^3)$
50	0.066	0.026	3.14×10^{-6}	3.41×10^{-5}
	0.171	0.030	3.22×10^{-6}	3.46×10^{-5}
	0.2	0.011	3.55×10^{-6}	3.01×10^{-5}
	Mean Values	0.026	3.35×10^{-6}	3.45×10^{-5}

Figure 4. 8. compares the experimental and the FEM simulated moisture concentration, plotted vs the square root of time for both input sets. The FEM results based on Set 1 for different membrane thicknesses agree with the experimental findings. Simulations using mean values (Set 2) reveal some noteworthy information about each optimized value and its impact on the trend. As discussed before (and reported in Appendix 4. 1(c)), the relaxation factor (β) governs the curve's trend in the very early stages of moisture absorption. For membranes with 66 and 171 μm thickness, the two simulations (Set 2) are in good agreement with the experimental results, as their relaxation factors (β) are very close to the mean value, as shown in Table 4. 2. Despite the difference in the relaxation factor values for the 200 μm thick membrane, there was no discernible difference between the two simulations in this initial phase of absorption. This confirm again the discrepancies in Figure 4. 4 (a) and the wide scatter observed for relaxation factor are not significant within the order of magnitude.

Diffusion coefficient (D) and saturation concentration (C_{sat}), instead, are the two most important factors influencing moisture absorption in the later stages. The two simulated curves (Set 1 and Set 2) for the membrane with a thickness of 171± 6 μm are almost identical since D and C_{sat} are quite close to their mean values. The prediction ability of the FEM simulation with mean values remains excellent even for the thinnest membrane

(h_a = 66 ± 1.5 μm). A mild swing to the left may be noted in this stage due to the higher mean diffusion coefficient in comparison to the one of this thickness.

For the thickest specimen simulation results (h_a = 200 ± 10.5 μm), the mean diffusion coefficient is lower than the one for this thickness. The reduction in diffusion coefficient, as predicted by the parametric research in Appendix 4. 1 (d), should cause a rightward shift in the curve. Nonetheless, the simulation with the mean diffusion coefficient exhibits an evident shift to the left. This is mainly due to the higher value of concentration at saturation (C_{sat}) that governs this massive movement in the opposite direction.

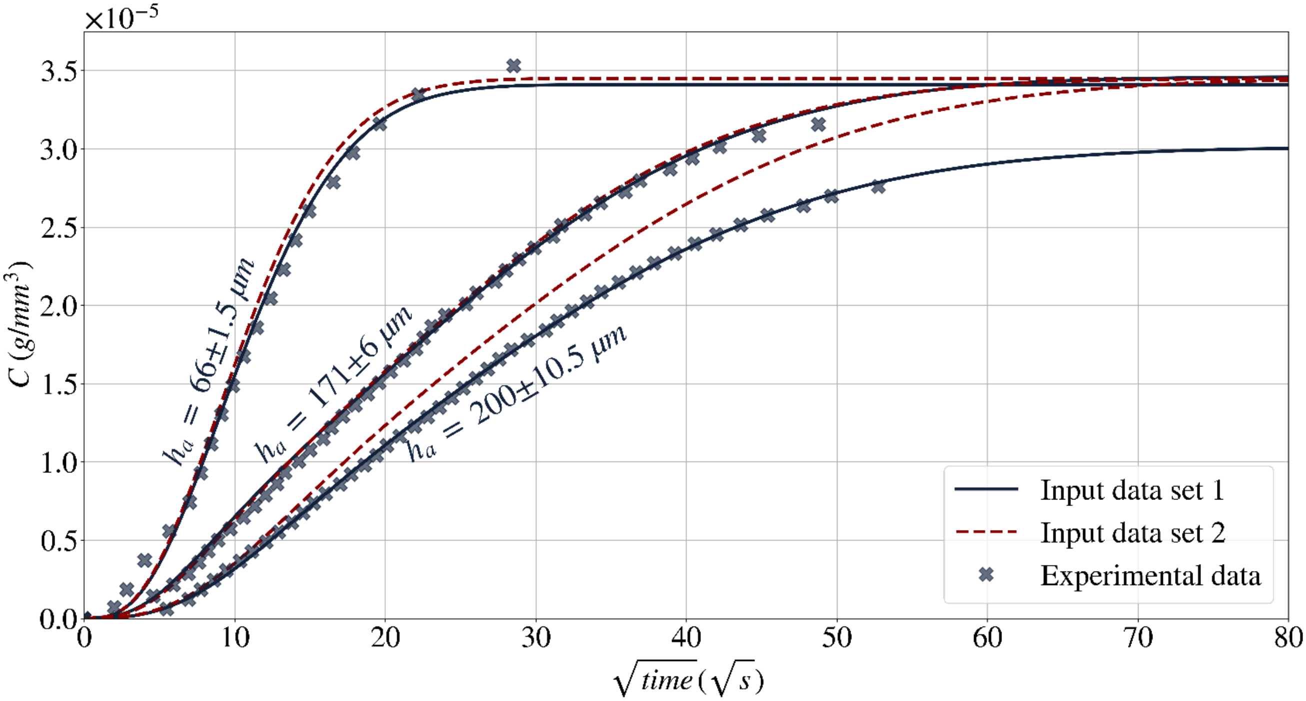

Figure 4. 8. Finite Element simulations and experimental data comparison

The next stage is to investigate the finite element model's reliability for future predictions. For this purpose, additional experimental absorption curves obtained for further two membranes with different thicknesses (h_a= 70.5 ± 3 and 145 ± 2 μm) than the ones tested in the experimental section were compared to predictions. Since the concentration at saturation was the most relevant parameter, the specimens were additionally weighted after 90 minutes of exposure to the relative humidity as well. Considering that the number of experimental data points for thin membranes (h_a < 100 µm) is nearly half that of experimental data points for thicker membranes (h_a>100 µm), tests were conducted twice for the membrane with a thickness of 70.5 ± 3 µm. The finite element simulations performed in advance for the new set of membranes together with the results of the corresponding moisture absorption experiments are depicted in Figure 4. 9. Three simulations were run for each of the two thicknesses with the β and D values (mean values from Table 4. 2) at three different relative humidity values (RH = 20, 38, and 52 %). The average values of the concentration at saturation for this set of experiment at each relative humidity value are consistent with the results shown in Figure 4. 5. For the new set of experiment, the predictions of finite element simulation are in good agreement with experimental data (R^2> 0.98). This underlines the validity of the developed numerical model for the prediction of sigmoidal diffusion in the considered cellulose acetate membrane.

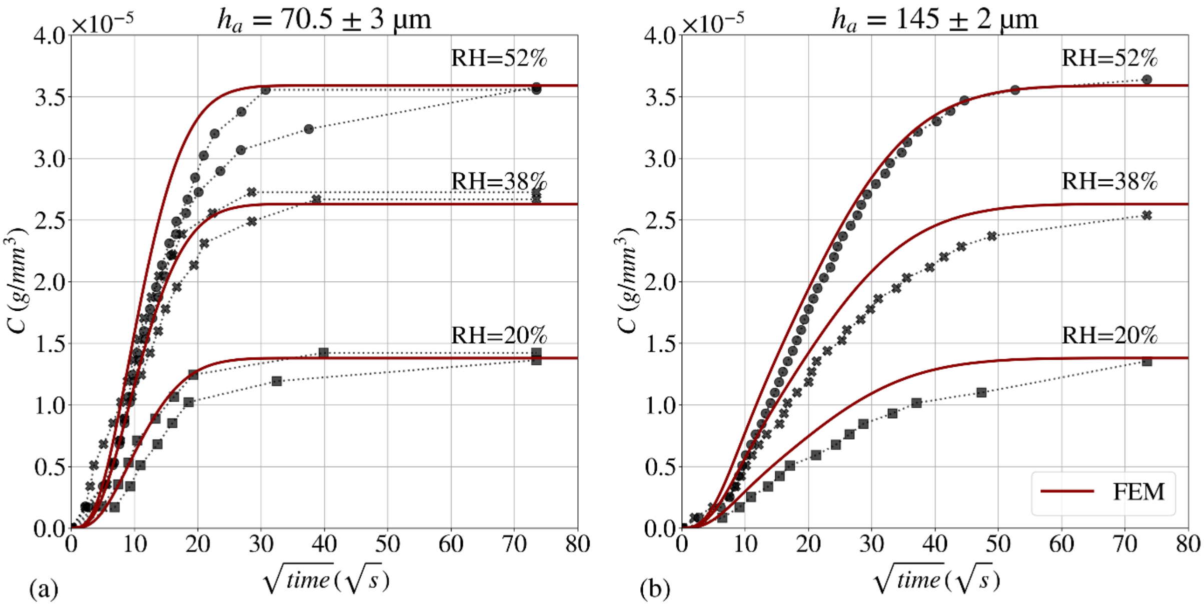

Figure 4. 9. Finite Element Modelling validation: comparison between the experimental results (symbols) of moisture absorption tests carried out on CA specimens' others than the ones used for model definition and the relevant FEM predictions (continuous lines).

References

1. Crank J. *The Mathematics of Diffusion*. Oxford university press; 1979.
2. Crank J, Park GS. Diffusion in high polymers: some anomalies and their significance. *Trans Faraday Soc*. 1951;47(1072):1072. doi:10.1039/tf9514701072
3. Alfrey Jr T, Gurnee EF, Lloyd WG. Diffusion in glassy polymers. In: *Journal of Polymer Science Part C: Polymer Symposia*. Vol 12. ; 1966:249-261.
4. Mensitieri G, Scherillo G. Environmental resistance of high performance polymeric matrices and composites. *Wiley Encycl Compos*. Published online 2011:1-25.
5. Xuejun Fan. Mechanics of moisture for polymers: Fundamental concepts and model study. In: *EuroSimE 2008 - International Conference on Thermal, Mechanical and Multi-Physics Simulation and Experiments in Microelectronics and Micro-Systems*. IEEE; 2008:1-14. doi:10.1109/ESIME.2008.4525043
6. Bagley E, Long FA. Two-stage Sorption and Desorption of Organic Vapors in Cellulose Acetate 1,2. *J Am Chem Soc*. 1955;77(8):2172-2178. doi:10.1021/ja01613a038
7. De Wilde WP, Shopov PJ. A simple model for moisture sorption in epoxies with sigmoidal and two-stage sorption effects. *Compos Struct*. 1994;27(3):243-252. doi:10.1016/0263-8223(94)90085-X
8. Wong CP. *Moisture Sensitivity of Plastic Packages of IC Devices*. (Fan XJ, Suhir E, eds.). Springer US; 2010. doi:10.1007/978-1-4419-5719-1
9. Crank J. A theoretical investigation of the influence of molecular relaxation and internal stress on diffusion in polymers. *J Polym Sci*. 1953;11(2):151-168. doi:10.1002/pol.1953.120110206
10. Crank J, Robinson C, Wilson AH. Interferometric studies in diffusion. II. Influence of concentration and orientation on diffusion in cellulose acetate. *Proc R Soc London Ser A Math Phys Sci*. 1951;204(1079):549-569. doi:10.1098/rspa.1951.0011
11. Roussis PP. Diffusion of water vapour in cellulose acetate: 1. Differential transient sorption kinetics and equilibria. *Polymer (Guildf)*. 1981;22(6):768-773. doi:10.1016/0032-3861(81)90012-4
12. Roussis PP. Diffusion of water vapour in cellulose acetate: 2. Permeation and integral sorption kinetics.

Polymer (Guildf). 1981;22(8):1058-1063. doi:10.1016/0032-3861(81)90292-5

13. Fan XJ, Lee SWR, Han Q. Experimental investigations and model study of moisture behaviors in polymeric materials. *Microelectron Reliab*. 2009;49(8):861-871. doi:10.1016/j.microrel.2009.03.006

14. Dingler C, Müller H, Wieland M, Fauser D, Steeb H, Ludwigs S. From Understanding Mechanical Behavior to Curvature Prediction of Humidity-Triggered Bilayer Actuators. *Adv Mater*. 2021;33(9). doi:10.1002/ADMA.202007982

15. Chen Q, Fang C, Wang G, et al. Hygroscopic swelling of moso bamboo cells. *Cellulose*. 2020;27(2):611-620. doi:10.1007/s10570-019-02833-y

16. González del Campo MM, Darder M, Aranda P, et al. Functional Hybrid Nanopaper by Assembling Nanofibers of Cellulose and Sepiolite. *Adv Funct Mater*. 2018;28(27):1703048. doi:10.1002/ADFM.201703048

17. Shrestha S, Diaz JA, Ghanbari S, Youngblood JP. Hygroscopic Swelling Determination of Cellulose Nanocrystal (CNC) Films by Polarized Light Microscopy Digital Image Correlation. *Biomacromolecules*. 2017;18(5):1482-1490. doi:10.1021/acs.biomac.7b00026

18. Lovikka VA, Rautkari L, Maloney TC. Changes in the hygroscopic behavior of cellulose due to variations in relative humidity. *Cellulose*. 25. doi:10.1007/s10570-017-1570-9

19. Franke B, Franke S, Schiere M, Müller A. Moisture diffusion in wood-Experimental and numerical investigations. In: *World Conference on Timber Engineering*. ; 2016.

20. Gibbons GC. 12—THE MOISTURE REGAIN OF METHYLCELLULOSE AND CELLULOSE ACETATE. *J Text Inst Trans*. 1953;44(5):T201-T208. doi:10.1080/19447025308659739

21. Shirangi H, Auersperg J, Koyuncu M, Walter H, Muller WH, Michel B. Characterization of dual-stage moisture diffusion, residual moisture content and hygroscopic swelling of epoxy molding compounds. In: *EuroSimE 2008 - International Conference on Thermal, Mechanical and Multi-Physics Simulation and Experiments in Microelectronics and Micro-Systems*. IEEE; 2008:1-8. doi:10.1109/ESIME.2008.4525009

22. Teverovsky a. A Rapid Technique for Moisture Diffusion Characterization of Molding Compounds in PEMs. *EEE Links, NASA/GSFC*. 2003;January, V(D). https://www.researchgate.net/publication/279913459%0AA

23. Khoshtinat S, Carvelli V, Marano C. Moisture absorption measurement and modelling of a cellulose acetate. *Cellulose*. 2021;28(14):9039-9050. doi:10.1007/s10570-021-04114-z

Appendix 4. 1. The "variable surface concentration model" parametric study

A parametric investigation for the provided model for sigmoidal moisture diffusion is offered here to highlight the influence of membrane's geometry (h_a), environmental condition (C_{sat}), and the material properties (D, β) on concentration evolution over time.

$$\frac{M_t}{2lC_{Sat}} = 1 - e^{-\beta t} \cdot \sqrt{\frac{D}{\beta l^2}} \cdot \tan\left(\sqrt{\frac{\beta l^2}{D}}\right) - \sum_{n=0}^{\infty} \frac{8}{\pi^2} \cdot \frac{\exp\left(-\frac{(2n+1)^2 \pi^2 \, Dt}{4l^2}\right)}{(2n+1)^2 \left\{1 - (2n+1)^2 \left(\frac{D\pi^2}{4\beta l^2}\right)\right\}}$$

For a more accurate comparison of trends, the following default values for each parameter were used:

$$h_a = 0.1\ (mm), \qquad C_{sat} = 1 \times 10^{-4}\ (g/mm^3), \qquad D = 1 \times 10^{-6}\ (mm^2/s), \qquad \beta = 0.01 (1/s)$$

Figure AP4. 1 (a) depicts the impact of thickness (h_a) variation. The default settings for β, D, and C_{sat} were used, whereas the thickness values ranged from 0.01 to 1 (mm). As expected, with a trend like Fickian behavior by variation of thickness, increases in membrane thickness lead to a decrease in slope and an increase in the amount of time required to attain saturation concentration.

The effect of the concentration at saturation (C_{sat}) is presented in Figure AP4. 1 (b). Default values for β, D, and h_a were used, whilst C_{sat} values vary within the range 2×10^{-5} to 1×10^{-4} (g/mm^3) with a step of 2×10^{-5} (g/mm^3) at a time. Since saturation concentration is proportional to relative humidity, this figure depicts the influence of relative humidity on the absorption curve trend, as well. As it can be seen, when the relative humidity is raised, both the slope and the time required to attain the saturation concentration increase.

Figure AP4. 1 (c), on the other hand, shows the influence of the Relaxation factor (β) variation. Default values for D, C_{sat}, and h_a were considered. Since a change in the order of magnitude is more effective for a clear understanding of the impact of parameter β, the values for this factor have ranged from 0.001 to 1 (1/s). As can be observed, parameter mostly influences the initial lag of the curve (short-term moisture absorption), which relates to the timeframe at which the membrane's surface level achieves saturation concentration. A huge difference between the end of the short-time absorption for the curves with β = 0.001 and β = 0.01 (1/s) can be observed ($\beta = 0.001 \rightarrow \sqrt{t} = 25$, $\beta = 0.01 \rightarrow \sqrt{t} = 10$). This disparity diminishes as β increases (β = 0.01 and 0.1(1/s)). The curves for β = 0.1 and β = 1 (1/s) exhibit a minimal difference before 100 seconds and exactly overlap above this period. Moreover, when β approaches infinity, the provided equation leads to formal Fickian law.

Finally, Figure AP4. 1 (d) portrays the influence of diffusion coefficient (D) variation. Default values for β, C_{sat}, and h_a were considered. Depending on the degree of substitution, a diffusion coefficient within the range of 1 × 10^{-6} to 1 × 10^{-5} (mm^2/s) is expected. As a result, the values for this phase of the parametric investigation have been altered in this range with an increase for each 2 × 10^{-6} (mm^2/s).

These graphs show that the diffusion coefficient has the greatest influence on the long-time of the moisture absorption process. Like Fickian behavior, the slope of the curve in long-time absorption increases as the diffusion coefficient increases.

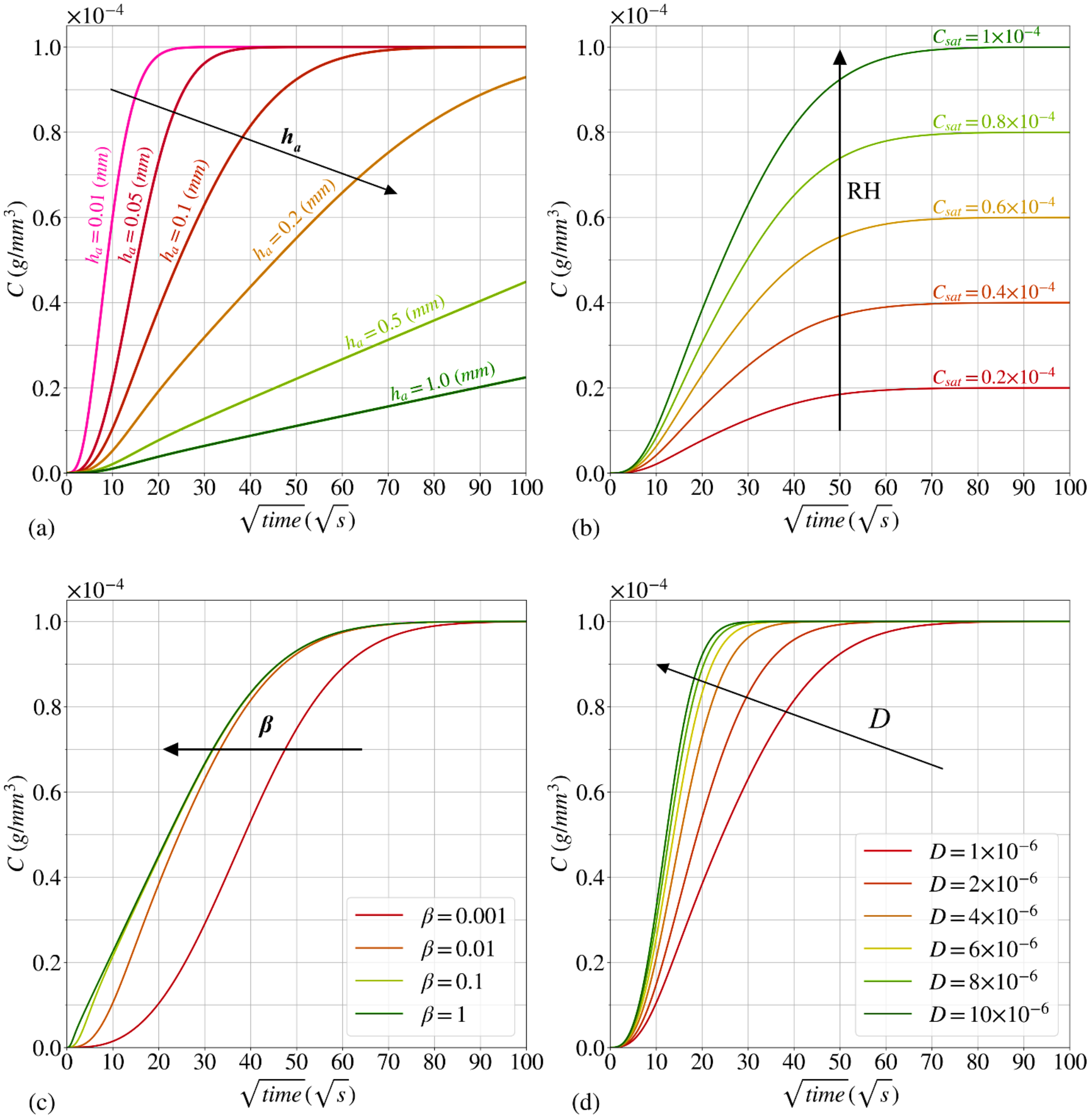

Figure AP4. 1. Parametric study of the “variable surface concentration model”

Appendix 4. 2. Complete gravimetric measurements

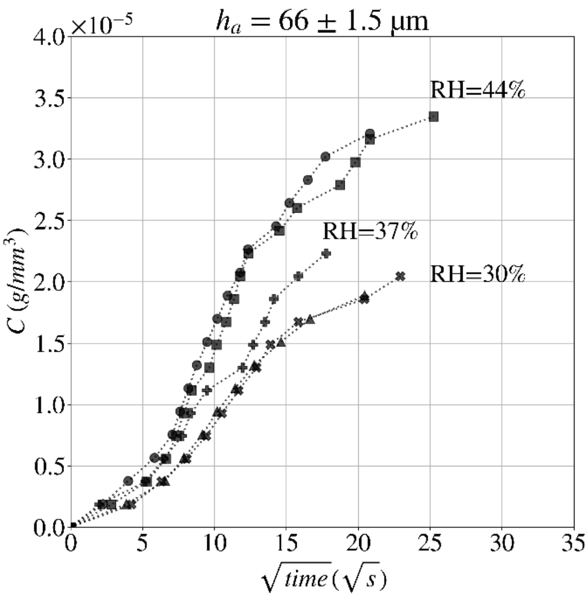

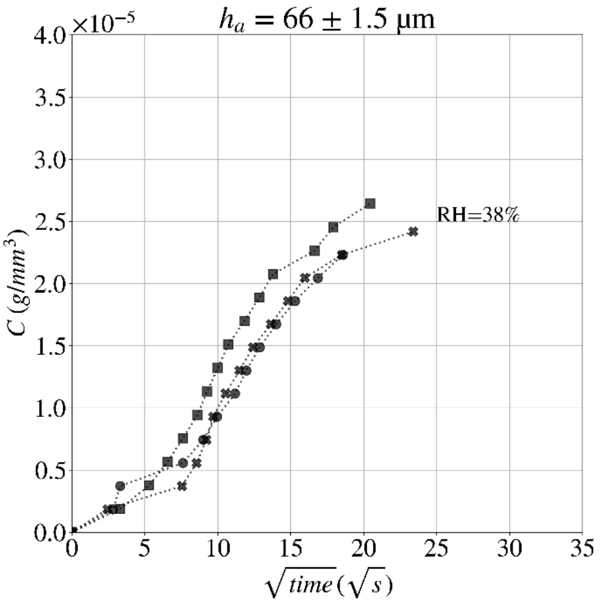

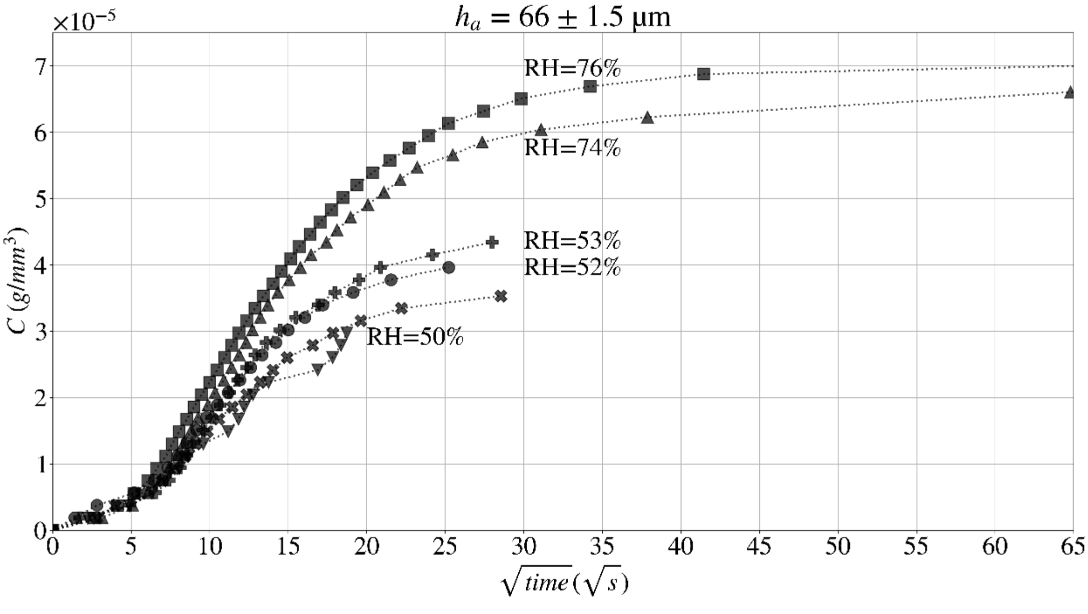

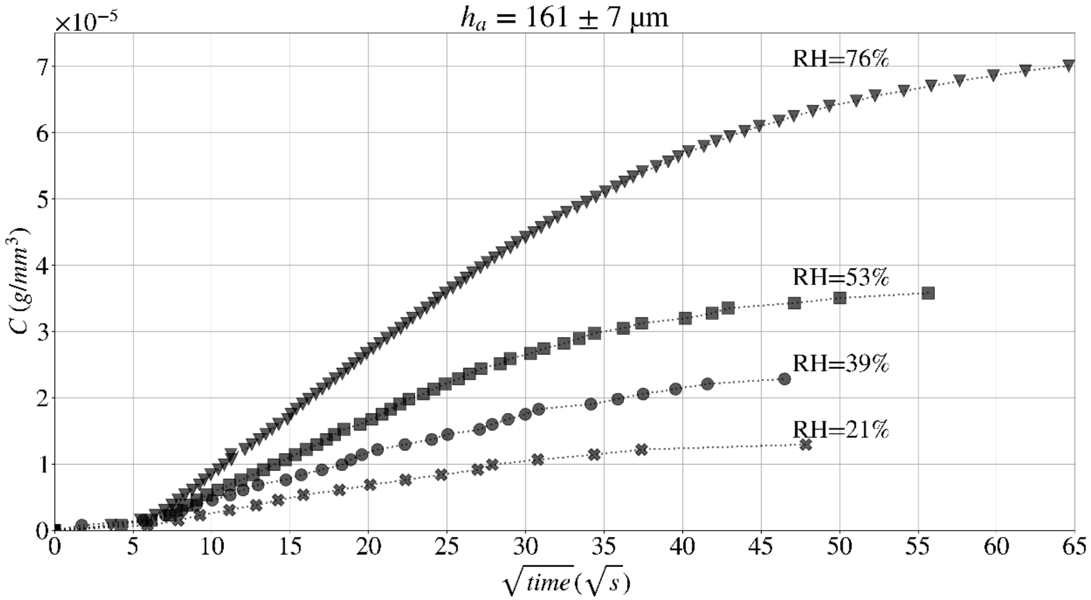
h_a = 161 ± 7 μm
×10⁻⁵
C (g/mm³)
0
1
2
3
4
5
6
7
RH=76%
RH=53%
RH=39%
RH=21%
0
5
10
15
20
25
30
35
40
45
50
55
60
65
√time (√s)

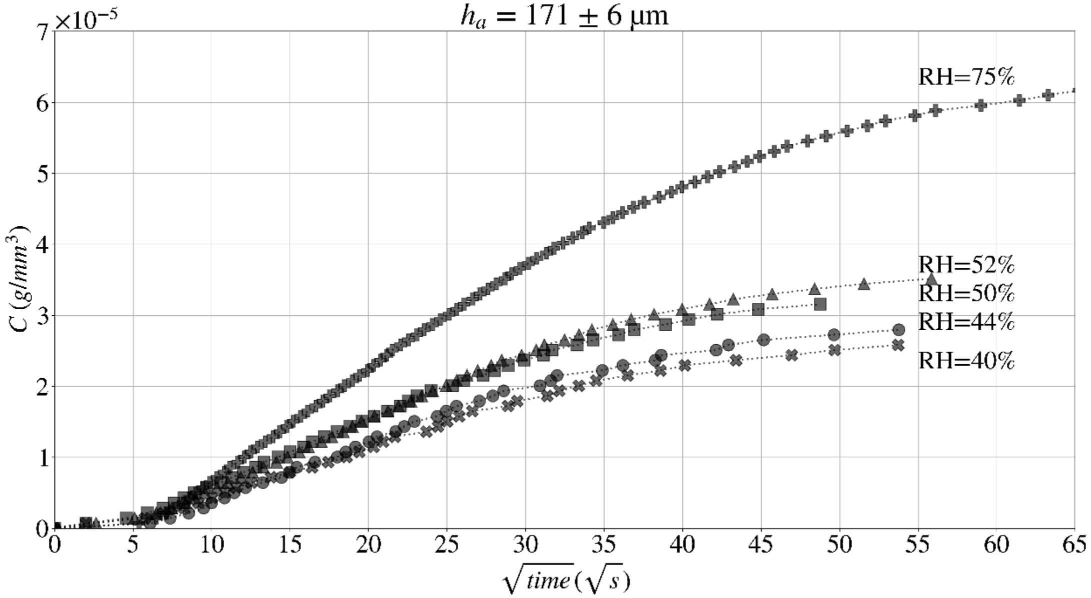
h_a = 171 ± 6 μm
×10⁻⁵
C (g/mm³)
0
1
2
3
4
5
6
7
RH=75%
RH=52%
RH=50%
RH=44%
RH=40%
0
5
10
15
20
25
30
35
40
45
50
55
60
65
√time (√s)

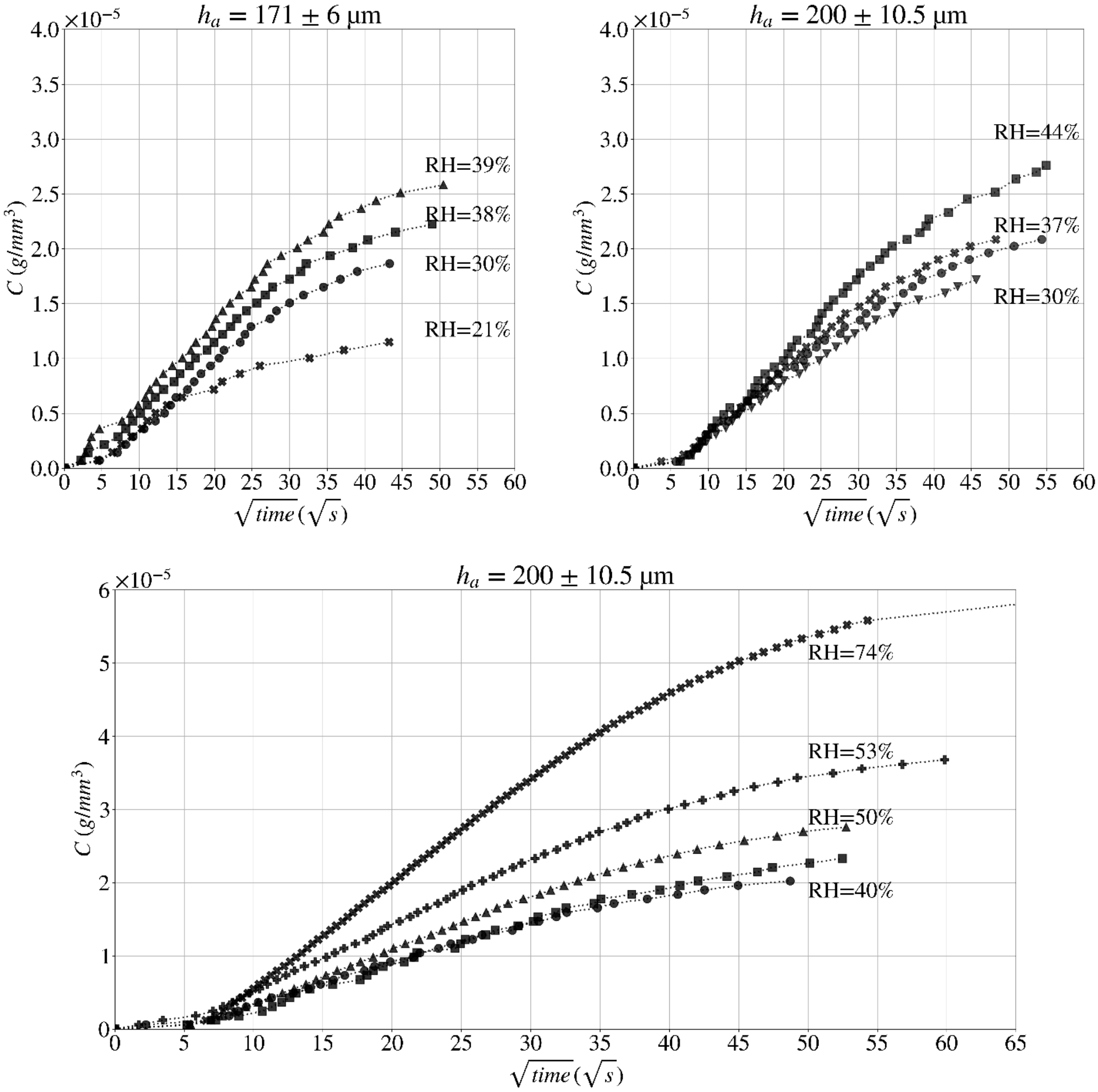

Figure AP4. 2. Complete gravimetric measurements

Appendix 4. 3. Python script developed for the best fitting of the experimental by the analytical model

❖ ***Calling modules***

```
import numpy as np
import math as mt
import matplotlib
import matplotlib.pyplot as plt
import pylab
import pandas as pd
%matplotlib inline
from pylab import *
from sklearn.metrics import r2_score
from scipy.optimize import curve_fit
```

❖ ***Importing excel file of experimental data***

```
Myfile = pd.ExcelFile(r'Experiment.xlsx')
T_list =list(Myfile.sheet_names)
def readExp(sheets):
    Test = pd.read_excel(r'Experiment.xlsx',sheet_name=sheets)
    Test = Test.ffill().fillna(0)
    list_col = Test.columns
    Test = Test.rename(columns={list_col[4]:'RH', list_col[5]:'ha',list_col[6]:'T_srf',list_col[7]:'T_Temp',
                              list_col[0]:'T_time', list_col[1]:'T_sqrt_t', list_col[3]:'T_Mt'})
        T_Temp=Test.T_Temp[0]
    ha = Test.ha[0]
    l = ha/2
    Test.T_Mt = Test.T_Mt/Test.T_srf
    Test['T_Csat'] = Test.T_Mt/Test.ha
    return Test, ha, l
Test, ha, l = readExp(T_list[5])
```

❖ *Defining the “variable surface concentration model”*

```
D = []
for sheet in T_list:

    Test, ha, l = readExp(sheet)
    print(ha)
    def sum_4_30(N,t,B,D):
        z=0
        for n in np.arange(N+1):
            don1pi2= ((2*n+1)*np.pi)**2
            Expo_4_30 = np.exp((-D*t * (don1pi2)) / (4*(l**2)))
            Makhraj_4_30 = ((don1pi2) * (1-(don1pi2)*D/(4*B*(l**2))))
            z = z+((8* Expo_4_30)/Makhraj_4_30)
        return z
    def Mt_4_30(t,B,D,C0):
        turns=100
        mt_2l_c0= 1-(np.exp(-B*t) * np.sqrt(D/(B*(l**2))) * np.tan(np.sqrt((B*(l**2))/D)))-sum_4_30(turns,t,B,D)
        mt_calc= mt_2l_c0* ha*C0
        return mt_calc

    def predict(t,B,D,C0):
        smt = []
        for temp in t:
            smt.append(Mt_4_30(temp,B,D,C0))
        return smt
```

❖ ***Best fitting of the model to the experimental data and obtaining C_{sat}, β , and D***

```
        g= [2.3e-2,3e-6,6e-6] #*Test.RH[0]
        bnds= ([0,1e-6,0],[np.inf,1e-5,np.inf])
        c,cov= curve_fit(predict,Test.T_time,Test.T_Mt,g,bounds=bnds)

        yopt= predict(Test.T_time,c[0],c[1],c[2])
        tm=np.arange(0,14401,2)
        sqrt_tm=np.sqrt(tm)
        yopt_plot= predict(tm,c[0],c[1],c[2])
        Mt2lc=yopt_plot/(Test.ha.values[0]*c[2])
        PyC=Mt2lc*c[2]
        fit=(Test.RH[0], ha,c[0],c[1],c[2],r2_score(Test.T_Mt,yopt),Test.T_Temp[0])
        print ('[\u03B2 (1/s), D (mm^2/s), Csat(gr/mm^3)]=', [c])

        from sklearn.metrics import r2_score
        print('R^2=', r2_score(Test.T_Mt,yopt))
        ymax = Test.T_Mt.max()
        yoptmax= yopt_plot[-1]
        d.append(fit)

    Fit_Output=pd.DataFrame(d,columns=('RH(%)', 'Thickness (mm)','\u03B2 (1/s)','Diffusion
(mm^2/s)','Concentration (gr/mm^3)','R^2', 'T_Temp(C)'))
```

Appendix 4. 4. Complete set of material characteristics by best fitting

RH (%)	$ha\ (mm)$	$\beta\ (1/s)$	$D\ (mm^2/s)$	$C_{sat}\ (g/mm^3)$	R^2
21	0.161	0.0280	3.07 E-06	1.45 E-05	0.9966
	0.171	0.0460	3.27 E-06	1.48 E-05	0.9444
30	0.066	0.0314	3.01 E-06	2.02 E-05	0.9926
		0.0203	3.01 E-06	2.08 E-05	0.9947
	0.171	0.0141	4.11 E-06	2.01 E-05	0.9988
	0.2	0.0136	4.03 E-06	1.93 E-05	0.9991
37	0.066	0.0460	2.97 E-06	2.46 E-05	0.9733
	0.2	0.0131	3.89 E-06	2.31 E-05	0.9988
		0.0166	3.59 E-06	2.22 E-05	0.9990
38	0.066	0.0460	3.02 E-06	2.78 E-05	0.9755
		0.0177	2.82 E-06	2.58 E-05	0.9801
		0.0146	3.53 E-06	2.51 E-05	0.9887
	0.171	0.0460	3.09 E-06	2.56 E-05	0.9941
39	0.161	0.0308	3 E-06	2.48 E-05	0.9980
	0.171	0.0460	3.08 E-06	2.94 E-05	0.9897
40	0.066	0.0305	2.95 E-06	2.99 E-05	0.9931
		0.0460	3.17 E-06	3.4 E-05	0.9778
		0.0460	3.02 E-06	2.97 E-05	0.9789
		0.0409	3.07 E-06	2.75 E-05	0.9670
	0.171	0.0182	3.12 E-06	2.7 E-05	0.9983
	0.2	0.0166	4.15 E-06	2.2 E-05	0.9991
		0.0099	3.32 E-06	2.56 E-05	0.9984
44	0.066	0.0460	3.04 E-06	3.43 E-05	0.9727
		0.0408	3.01 E-06	3.3 E-05	0.9738
	0.171	0.0157	3.12 E-06	2.94 E-05	0.9967
	0.2	0.0100	3.43 E-06	2.93 E-05	0.9981
50	0.066	0.0344	2.95 E-06	3.45 E-05	0.9894
		0.0361	2.98 E-06	3.09 E-05	0.9776
	0.171	0.0373	3.03 E-06	3.54 E-05	0.9969
	0.2	0.0157	3.06 E-06	3.14 E-05	0.9981
52	0.066	0.0332	2.98 E-06	3.95 E-05	0.9866
	0.171	0.0142	3.3 E-06	3.62 E-05	0.9993
53	0.066	0.0183	2.91 E-06	4.27 E-05	0.9967

	0.161	0.0133	3.52 E-06	3.62 E-05	0.9995
	0.2	0.0155	3.38 E-06	3.86 E-05	0.9993
74	0.066	0.0215	1.59 E-06	6.37 E-05	0.9974
	0.2	0.0092	2.86 E-06	6.37 E-05	0.9996
75	0.145	0.0111	1.85 E-06	6.53 E-05	0.9995
	0.171	0.0118	2.32 E-06	6.42 E-05	0.9992
76	0.066	0.0263	1.6 E-06	6.84 E-05	0.9991
	0.161	0.0116	2.48 E-06	7.05 E-05	0.9998

Appendix 4. 5. Simulation of the non-Fickian Diffusion for two CA membranes differing in their thicknesses

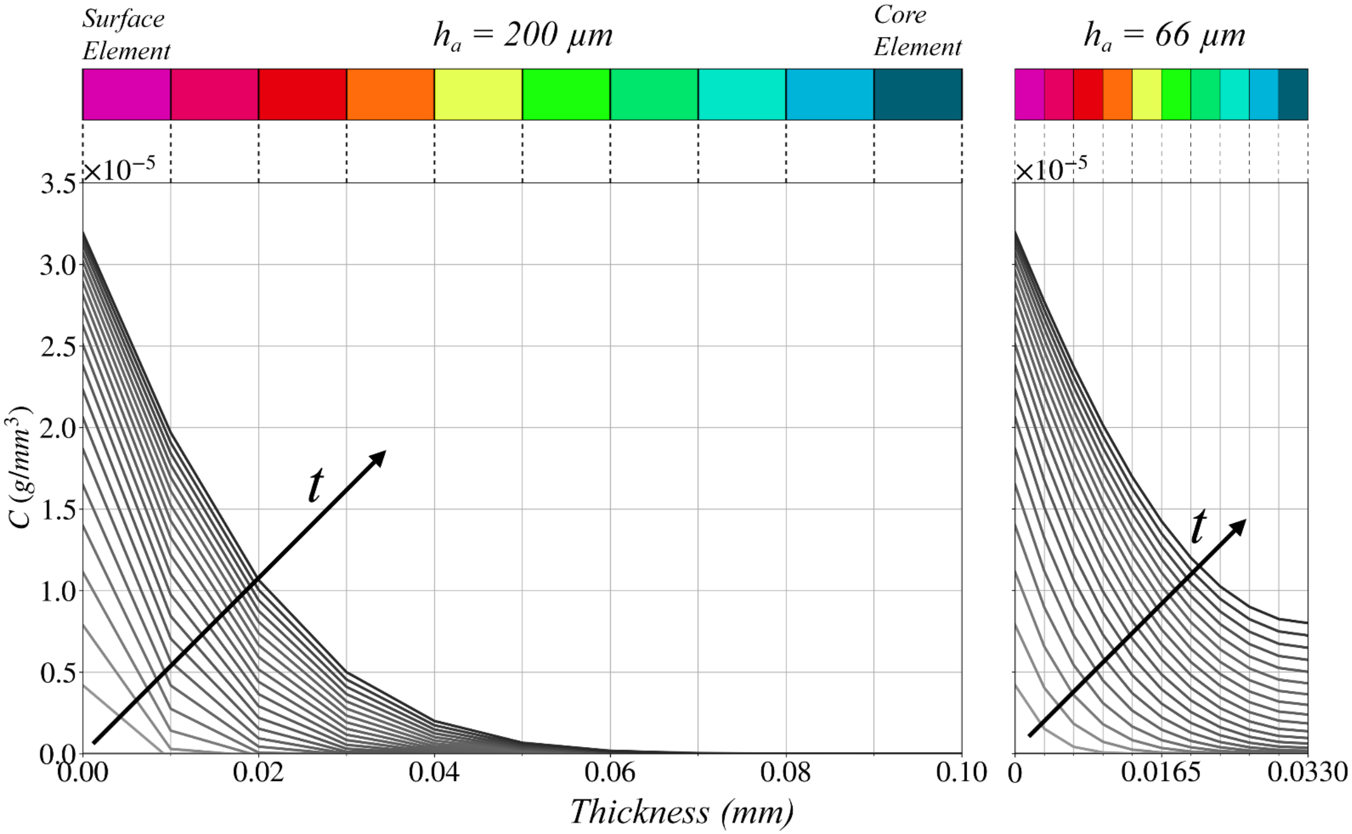

Figure AP4. 3. Finite element Simulation of the non-Fickian Diffusion for different thicknesses

5 Hygroscopic Strain and Coefficient of Hygroscopic Expansion

This chapter introduces the definition of hygroscopic expansion as well as experimental procedures for its measurement. The Thermomechanical Analysis (TMA) approach to characterize the induced hygroscopic strain (ε_{hygro}) on a cellulose acetate membrane caused by moisture absorption at different humidity level is discussed. A polynomial function is used to represent the non-linear relationship between hygroscopic strain and the environment's relative humidity. The coefficient of hygroscopic expansion (α) is determined as a function of relative humidity by the estimated moisture concentration at saturation (C_{sat}) and the related induced strain (ε_{hygro}). Numerical simulations of hygroscopic strain at various relative humidity levels are provided and compared to other approaches in the literature.

5.1 Introduction

As previously described in Section 2.5, the most significant property to characterize the hygroscopic behavior of a material is the hygroscopic expansion coefficient (α). Following the characterization of moisture diffusion and concentration at saturation (C_{sat}) for cellulose acetate membranes, the related mechanical deformation (hygroscopic strain ε_{hygro}) is detailed here.

Initially, a digital image analysis was utilized to evaluate the hygroscopic strain using the approach described by Changsoo Jang et al. [1]. Despite all efforts to maintain the membrane intact, the fast response of the cellulose acetate and the sealing procedure had an impact on the measurement, resulting in not negligible errors. Appendix 5. 1 describes the details of image analysis experiments and the obtained results the hygroscopic strain.

Referring to the definition of hygroscopic strain (Section 2.5), this property is independent of moisture absorption and diffusion when the material achieves a saturation state. Therefore, the hygroscopic strain may be calculated based on the desorption process, starting from saturated specimen at equilibrium stated and drying the specimen, using Thermomechanical Analysis (TMA) within certain circumstances. As mentioned before, when the drying temperature exceeds the glass transition temperature of the material, the parallel TMA/TGA approach is ineffective [2–7]. Given that the glass transition temperature of the cellulose acetate membranes in this study was determined to be roughly 175 °C (Section 1), at temperatures considerably lower than this level (125 °C in this study) as drying temperature during the experiments, this potential downside will not be an issue for Thermomechanical Analysis performed. Another point of concern for employing parallel TMA/TGA experiments was the overestimation of coefficient of hygroscopic expansion [8]. This drawback stems from overlapping data from Thermogravimetric analysis data during desorption, which leads to results with significant inaccuracies in relation to the absorption. Since the concentration at saturation in this research is measured by direct gravimetric measurement (weighing), this issue will not arise in the context of this study.

The characterization of hygroscopic strain for highly hygroscopic materials via Thermomechanical Analysis requires meticulous attention. In particular, for membranes with thickness lower than 500 μm, measuring the dimensional variation across the thickness using a macro-expansion probe might result in inaccurate estimates for hygroscopic strains [9]. Appendix 5. 2 presents the results of the experimental data for thermomechanical study done on membrane for hygroscopic strain characterization through the thickness utilizing a macro-expansion probe. The macro-expansion probe covers a wide area (about 30 mm^2) of a sample surface and thus provides more representative measurements. However, even when the instrument's maximum applied force is employed (1 N), out of plane deflection of the thin membrane due to moisture desorption cannot be avoided. Therefore, a tensile loading arrangement was used by a Thermomechanical Analyzer's film/fiber probe.

5.2 Thermomechanical Analysis

The Thermomechanical Analysis was performed using a Discovery TMA 450 (TA instruments®) with a film/fiber probe. 25 × 4 mm^2 specimens (suitable for the gauge length of about 11 mm) were cut in both longitudinal and transversal directions to the K Coater control blade movement direction, to analyze any anisotropy in the CA membrane caused by the production process. For at least 24 hours, the specimens were preconditioned at 25 °C in climatized cabinets and at several levels of relative humidity (RH = 31-76 %) to achieve moisture absorption saturation conditions. As mounting the specimen between the jaws required a few minutes and the material may have desorbed moisture during this time, each specimen was put between the jaws and stored for an additional hour within the climatized chamber to restore any lost moisture. It was then rapidly put in the TMA testing chamber. The entire procedure of transferring the specimen and locking the TMA cell took less than 20 seconds.

The ASTM E831-6 standard, demands for the application of a force ranging from 1 to 100 mN to ensure contact between the specimen and the probe. The applied force to each specimen was modified in each test to achieve an applied pre-stress of 1 MPa, which results in little mechanical deformation throughout the test, considering the Young's modulus of cellulose acetate membranes (1 GPa, Section 3.5). Since the goal of this study is to investigate the hygroscopic behavior of cellulose acetate membranes at room temperature (T = 25 °C), all specimens attained saturation state at this temperature and all TMA tests started and terminated at 25 °C. Before (humid condition) and after (dry condition) the TMA test, the specimen's length, width, and thickness were measured. The test procedure for Thermomechanical Analysis is as follows:

(i) initial length measurement (L_0);

(ii) applying the force to achieve a pre-stress of 1 MPa;

(iii) heating from 25 to 125 °C with 5 °C/min rate to promote moisture desorption;

(iv) maintaining isothermal conditions at 125 °C for one hour to achieve fully dried specimen;

(v) cooling from 125 to 25 °C at a rate of 5 °C/min, to restore the thermal expansion.

Figure 5. 1 (a) depicts, in the plot, an example of the specimen thermal history, and the variation of the specimen length (ΔL_{Tot}) for a specimen conditioned at relative humidity of 75 % and T = 25 °C; and above the plot, a schematic representation of the specimen in each phase of the test. The complete set of experimental results is

reported in Appendix 5. 3. The dimensional variation (ΔL_{Tot}) of the specimen in Figure 5. 1 (a) is the outcome of the superposition of three mechanisms, namely the mechanical (ΔL_{mech}), thermal (ΔL_{therm}), and hygroscopic (ΔL_{hygro}), see Equation (5.1).

$$\Delta L_{Tot} = \Delta L_{mech} + \Delta L_{therm} + \Delta L_{hygro} \tag{5.1}$$

The mechanical deformation (ΔL_{mech}) is caused by the applied force ($F \rightarrow \sigma = 1\ MPa$) at the beginning of the experiment. The value of ΔL_{Tot} at the starting point ($P0$) is zero. By initiating the test and applying the set force, instantaneous elongation can be seen ($P1$), which has been observed in all experiments. Figure 5. 1(b) shows an enlargement of mechanical deformation of this specimen at beginning of the test. The imposed force resulted in a mechanical elongation of about 4 μm for this specimen, which corresponds to a mechanical strain of about 0.03%, which is negligible.

By the beginning of the heating process ($P1$), an increase in length attributed to thermal expansion can be expected. However, a dramatic decrease in length is evidently observed here. The specimen is experiencing a hygrothermal deformation at this point, see also Figure 5. 1(b). Which is the result of a thermal expansion caused by temperature increase and a hygroscopic shrinkage caused by moisture desorption. For the first 15 minutes of the test, the hygroscopic contraction is significantly greater than the thermal expansion for the specified specimen. Therefore, the superposition of the thermal and hygroscopic deformations results in an overall shrinkage, hence a negative deformation. This trend lasted until the temperature reached 85 °C, at which point the specimen shrunk by roughly 100 μm compared to its length at $P1$. After this point, the length of the specimen starts to increase until reaching the set point temperature of 125 °C. This switch in trend indicates that thermal expansion is dominating hygroscopic shrinkage. It should be noted that the duration of the descending trend and the temperature at which the turning point occurs are both affected by the humidity level at which the specimen was equilibrated. The higher the humidity level, the longer it takes to desorb the acquired moisture from the membrane, and the turning point happens at higher temperatures (Appendix 5. 3).

A negligible difference (less than 20 nm) in elongation may be detected throughout the one-hour isothermal step at 125 °C. It implies that the specimen is totally dry and that the applied force does not cause creep in the specimen. $P2$ denotes the dry specimen under thermal expansion at 125 °C. The only deformation generated by cooling the completely dry specimen at this point from 125 °C to 25 °C is thermal contraction (ΔL_{therm}), which is equal to the thermal expansion of the dry cellulose acetate membrane from 25 °C to 125 °C (Appendix 5. 4). Finally, the point $P3$ represents the dry specimen that has been equilibrated at 25 °C.

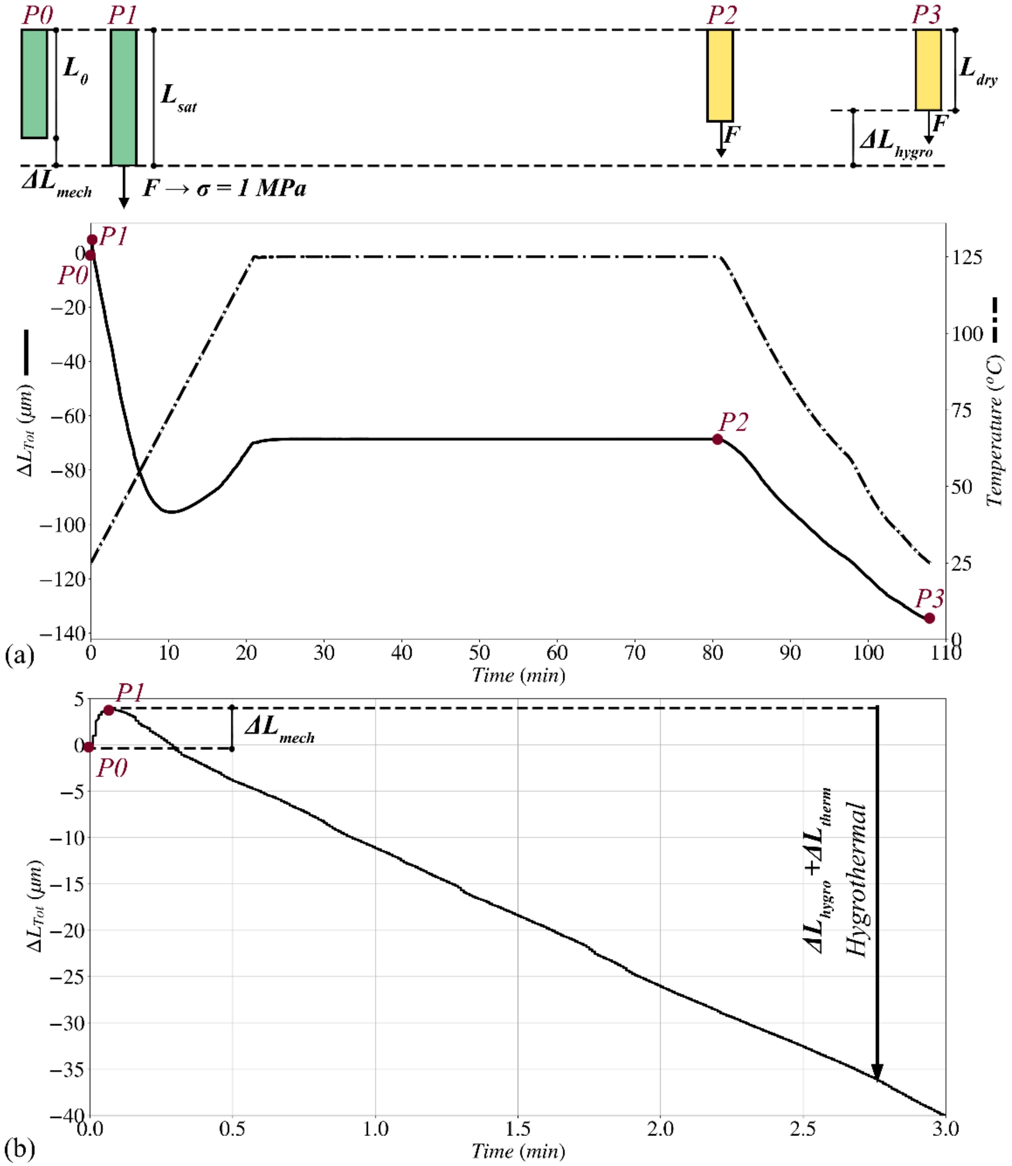

Figure 5. 1. a) Specimen thermal history and relevant length change as measured in a Thermomechanical test, b) Mechanical deformation of the membrane due to applied force at the beginning of the test

Because the whole moisture desorption process happens while mechanical load is applied in this experimental approach, the length of the specimen at $P1$ must be regarded as the length in the saturation state (L_{sat}), and the length at $P3$ as the length in dry condition (L_{dry}). The hygroscopic strain must be calculated with respect to the dry condition ($\varepsilon_{hygro} = \frac{L_{sat} - L_{dry}}{L_{dry}}$).

Figure 5. 2 depicts the hygroscopic strain (ε_{hygro}) as a function of relative humidity for tested specimens cut from a CA membrane in both transversal and longitudinal directions with respect to the Doctor Blade direction movement. The lack of orientation dependency in the experimental results validates the membrane's isotropy for the tested range of relative humidity, as observed in the membrane mechanical characterization reported in Section 3.5. Following the same relative humidity dependency pattern seen for moisture concentration at saturation (Figure 4. 5), the hygroscopic strain increases sharply when relative humidity exceeded 53%. Therefore, like C_{sat}, the hygroscopic strain function of relative humidity was fitted by a third order polynomial, yielding Equation (5.2) (R^2 = 0.997).

$$\varepsilon_{hygro} = 8.03 \times 10^{-8} \times\ RH^3 - 5.14 \times 10^{-6} \times\ RH^2 + 1.16 \times 10^{-4}\ \times\ RH \qquad (5.2)$$

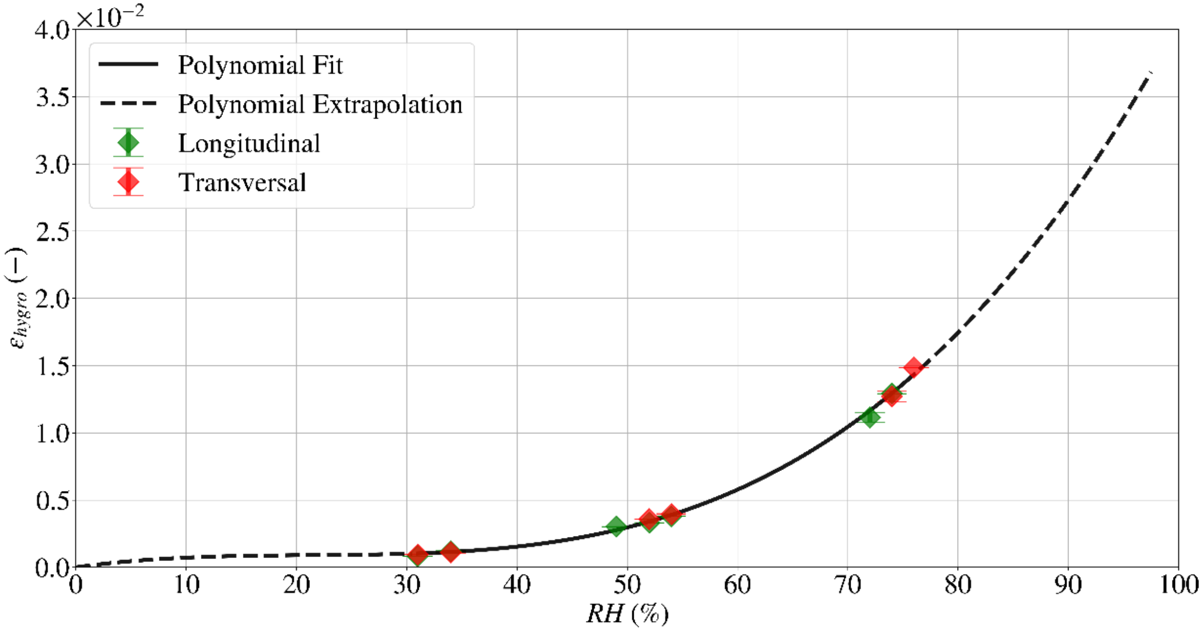

Figure 5. 2. Thermomechanical Analysis and the best-fitting polynomial for hygroscopic strain (bars represent data semi-dispersion of measurements)

5.3 Coefficient of Hygroscopic Expansion (α)

The hygroscopic expansion coefficient (α) is defined as the ratio of the relative linear expansion caused by moisture absorption in a dry material (ε_{hygro}) to the moisture concentration at saturation (C_{sat}) [10]. Many studies on hygroscopic behavior, particularly in integrated circuit packaging, assume a linear relationship between hygroscopic strain and moisture concentration as a function of relative humidity, resulting in a constant and relative humidity independent coefficient of hygroscopic expansion [1,3,7,8,11–15]. In some studies, despite an obvious non-linear trend for hygroscopic strain and moisture concentration, as well as a variable coefficient of hygroscopic expansion, a constant value has been considered for the coefficient of hygroscopic expansion [2,4].

Two polynomials were utilized in this research to describe the concentration at saturation (Equation (4.3)) and the hygroscopic strain (Equation (5.2)) as a function of the relative humidity. Figure 5. 3 (a) depicts the relative humidity dependence of hygroscopic strain and concentration at saturation as predicted by the two mentioned equations. The different trend of the moisture concentration at saturation and the relative induced hygroscopic strain with relative humidity may be explained by the membrane porosity, as discussed in literature [10]. When the relative humidity is below 40%, the moisture absorbed by the material simply fills the membrane nano-pores; no water molecules interact with the hydroxyl groups of the CA molecular chains to cause an expansion in the material. This interaction, on the other hand, occurs at greater relative humidity levels.

As a common assumption of several studies [1,3,7,8,11–15], a constant coefficient of hygroscopic expansion can be determined by the slope of the linear fitting to the graph of hygroscopic strain (ε_{hygro}) vs. concentration at saturation (C_{sat}), intercepting at zero. Figure 5. 3 (b) illustrates the mentioned graph together with experimental data available for both gravimetric and thermomechanical analysis (C_{sat} and ε_{hygro}) for the same level of relative humidity. The observed trend is similar to the behavior detailed by Teverovsky [16], Park et al. [2], and Zhang et al. [4], who however, assumed a constant value for the coefficient of hygroscopic expansion, despite the obvious trend. Considering the linear fitting in Figure 5. 3 (b) (green line), the constant value of 138 mm^3/g is obtained for α ($R^2 = 0.89$). The resulting constant value for α, with a low *R-scored* value, does not look suitable when compared to the polynomial function, which is in strong agreement with the experimental data. Therefore, this aspect will be studied further by finite element modeling of hygroscopic expansion, comparing the experimental results and finite element models by constant value of α and variable as a function of relative humidity as in Equation (5.3) and depicted in Figure 5. 3 (c).

$$\alpha = \frac{\varepsilon_{hygro}}{C_{sat}} = \frac{803 \times RH^2 - 51400 \times RH + 1.16 \times 10^6}{1.19 \times RH^2 - 79.7 \times RH + 8090} \tag{5.3}$$

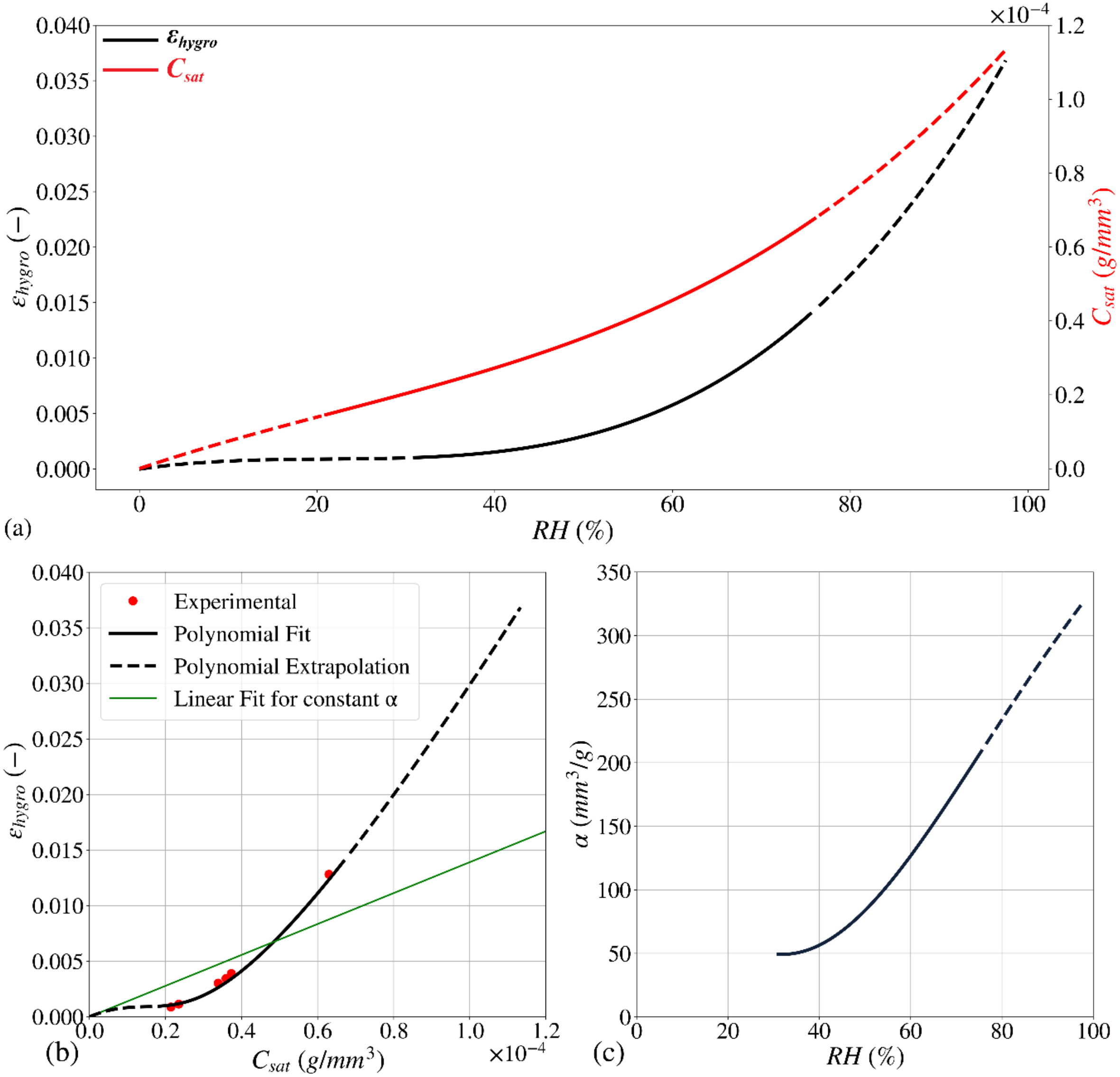

Figure 5. 3. (a) hygroscopic strain (Equation (5.2)) and concentration at saturation (Equation (4.3)) as a function of relative humidity, (the domain containing experimental data and extrapolation of the polynomial fit are shown by the continuous and dashed lines, respectively), (b) hygroscopic strain as a function of moisture concentration at saturation, (c) coefficient of hygroscopic expansion (α) as function of relative humidity

5.4 Finite Element Modeling

Finite element simulations with COMSOL Multiphysics 5.6 were used to determine the hygroscopic strain. A multiphysics approach combining transport of diluted species (diffusion) and solid mechanics (hygroscopic expansion) was applied. A time-dependent analysis for absorbed moisture concentration and subsequently a stationary analysis for mechanical behavior were implemented to reduce the computational time.

Figure 5. 4 provides a schematic representation of details of the finite element model. To discretize each specimen with the dimensions of the dry state, a 3D prismatic geometry was considered. The dry specimen length, width, and thickness (measured after the thermomechanical analysis test) were utilized to discretize one-fourth of the prism ($\frac{L_{dry}}{2} \times \frac{W_{dry}}{2} \times h_{dry}$), exploiting symmetries to reduce the computation time even further. From one lateral surface to the other, a user-controlled general physics sweeping mesh with quadrilateral face along the straight-line path has been applied, resulting in a discretized volume by 10 × 5 × 10 hexahedral components (total of 500 elements exploiting symmetries).

A user-defined material with intrinsic physical and mechanical properties of the cellulose acetate in dry condition such as, density ρ = 1.3×10^{-4} (g /mm^{3}) [17], Young's modulus E = 1.1 GPa (Section 4.3), Poisson's ratio 0.39 [17], relaxation factor (β) 0.026 1/s (Section 4.3), and a diffusion coefficient D = 3.35×10^{-6} mm^{2}/s (Section 4.3) was adapted. The relative humidity dependent coefficient of hygroscopic expansion ($\alpha_{variable}$) is defined according to Equation (5.3). The time-dependent model for non-Fickian behavior and the concentration at saturation (Csat) as function of relative humidity (RH) described in Section 4.4 was adopted. The length at humid conditions (direction X) was used to calculate the induced hygroscopic strain.

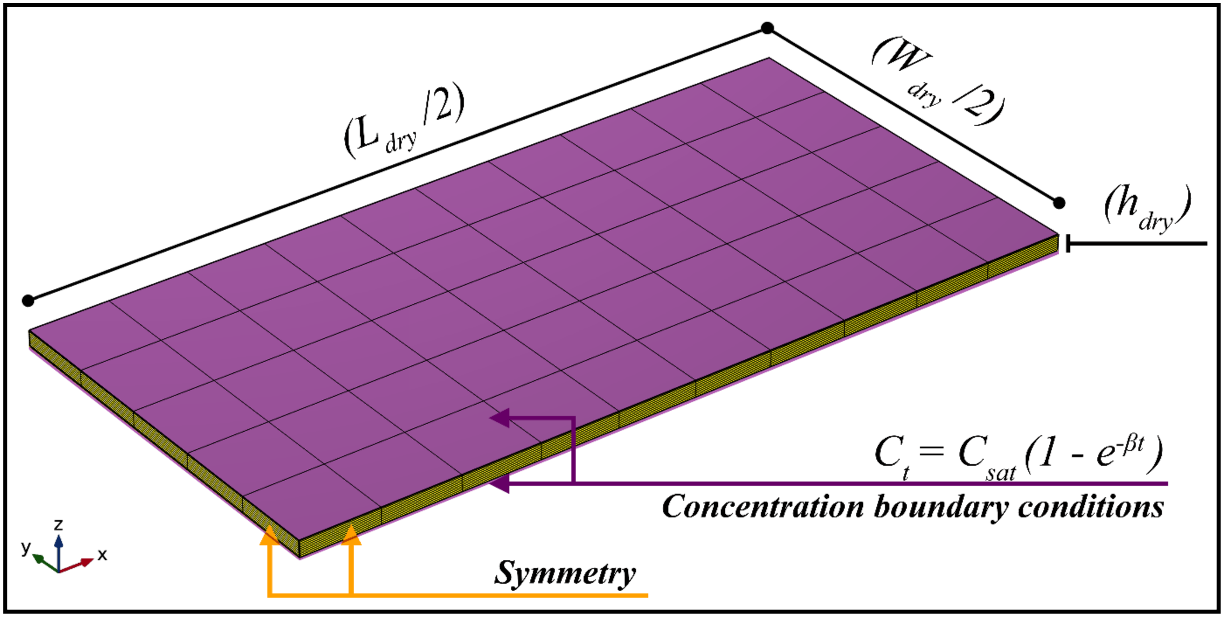

Figure 5. 4. Finite element model's details

The experimental data obtained from specimens conditioned at RH values of 31, 52, and 74% were used for comparison. The dimensions of the specimens in dry conditions (measured at the conclusion of the TMA tests) are listed in Table 5. 1. Two sets of simulations were performed. Set 1 used the variable coefficient of hygroscopic expansion coefficient (Equation (5.3)). The second set, on the other hand, considers the constant value of α = 138 mm^3/g, from Figure 5. 3 (b).

Table 5. 1. Details and input parameters of the specimens simulated by finite element model.

$RH\ (\%)$	$L_{dry}\ (mm)$	$W_{dry}\ (mm)$	$h_{dry} (mm)$	$C_{sat}\ (g/mm^3)$*	$\alpha\ (mm^3/g)$ *
31	11.054	3.9	0.116	2.1×10^{-5}	50
52	11.025	4	0.104	3.73×10^{-5}	92
74	11.886	3.8	0.110	6.44×10^{-5}	201

*) C_{sat} and α are calculated by Equation (4.3)and Equation (5.3), respectively.

Figure 5. 5 reports a comparison of the hygroscopic strain estimated via finite element modeling with both input sets and the experimental results. A very good agreement between the prediction of hygroscopic strain and the experiments is exhibited for the first input set (variable α according to Equation (5.3)). It shows that the combination of non-Fickian moisture diffusion and the resulting induced deformation by the absorption can offer a reliable estimation of the ultimate induced hygroscopic expansion as a function of environment relative humidity. Regarding the second set of simulations (constant α =138 mm^3/g), as expected, the hygroscopic strain predicted by the model shows a steady increase with the increase of the relative humidity, which leads to a considerable discrepancy with the experimental measurements. Clearly, the predicted hygroscopic strain by the constant coefficient of hygroscopic expansion matches with the real value for just one relative humidity level (RH = 62 %), where the estimated by Equation (5.3) is identical to the assessed constant α (138 mm^3 /g). All other simulations with a constant value of α result in an overestimation at relative humidity below 62 % and an underestimation for humidity level above 62%.

This comparison shows that relative humidity has a significant influence on the coefficient of hygroscopic expansion. Furthermore, it emphasizes that the coefficient of hygroscopic expansion (α) of a highly hygroscopic material, such as cellulose acetate, cannot be assumed constant or linearly dependent on relative humidity.

These results bring into light two main aspects.

(i) the precision of the finite element model by the comparison between the numerical estimation of hygroscopic strain and the experimental observations;

(ii) the inadequacy of the constant-value assumption for the coefficient of hygroscopic expansion for highly hygroscopic materials, by comparing the results of simulations done by the constant value of α to those obtained with the non-linear relative humidity dependency (Figure 5. 5)

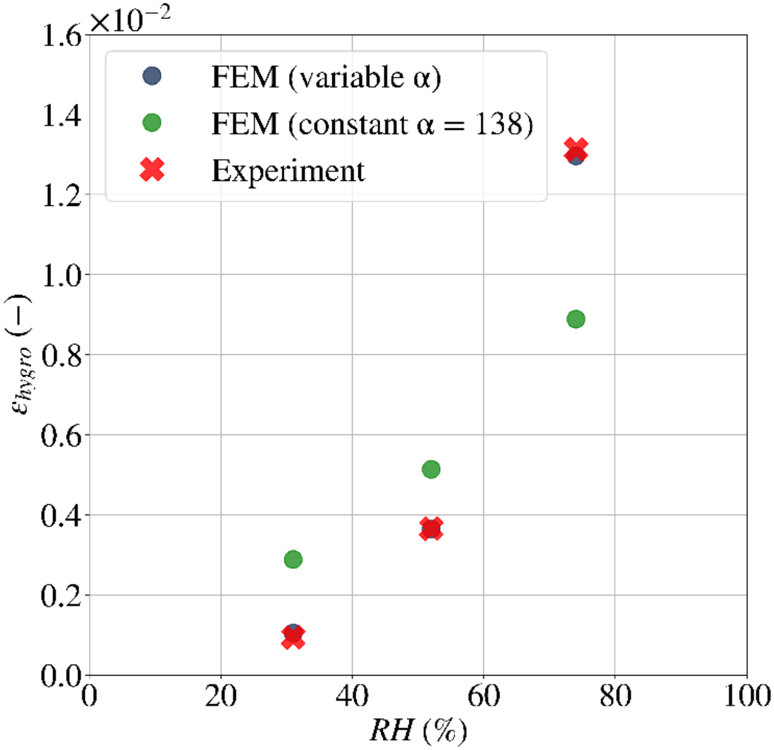

Figure 5. 5. Comparison of experimental and finite element simulation for hygroscopic strains

References

1. Changsoo Jang, Yoon S, Bongtae Han. Measurement of the Hygroscopic Swelling Coefficient of Thin Film Polymers Used in Semiconductor Packaging. *IEEE Trans Components Packag Technol*. 2010;33(2):340-346. doi:10.1109/TCAPT.2009.2038366

2. Park S, Haojun Zhang, Xin Zhang, Siu Lung Ng, Ho Chong Lee. Temperature dependency of coefficient of hygroscopic swelling of molding compound. In: *2009 59th Electronic Components and Technology Conference*. IEEE; 2009:172-179. doi:10.1109/ECTC.2009.5074012

3. Shirangi H, Auersperg J, Koyuncu M, Walter H, Muller WH, Michel B. Characterization of dual-stage moisture diffusion, residual moisture content and hygroscopic swelling of epoxy molding compounds. In: *EuroSimE 2008 - International Conference on Thermal, Mechanical and Multi-Physics Simulation and Experiments in Microelectronics and Micro-Systems*. IEEE; 2008:1-8. doi:10.1109/ESIME.2008.4525009

4. Zhang H, Park S, Hong S. Hygroscopic swelling behavior of molding compound at high temperature. In: *2010 12th IEEE Intersociety Conference on Thermal and Thermomechanical Phenomena in Electronic Systems*. IEEE; 2010:1-7. doi:10.1109/ITHERM.2010.5501272

5. Shirangi MH, Wunderle B, Wittler O, Walter H, Michel B. Modeling cure shrinkage and viscoelasticity to enhance the numerical methods for predicting delamination in semiconductor packages. *2009 10th Int Conf Therm Mech Multi-Physics Simul Exp Microelectron Microsystems, EuroSimE 2009*. Published online 2009:1-8. doi:10.1109/ESIME.2009.4938412

6. Shirangi MH, Muller WH, Michel B. Effect of nonlinear hygro-thermal and residual stresses on the interfacial fracture in plastic IC packages. In: *2009 59th Electronic Components and Technology Conference*. IEEE; 2009:232-238. doi:10.1109/ECTC.2009.5074022

7. Jiang Zhou, Lahoti SP, Sitlani MP, Kallolimath SC, Putta R. Investigation of non-uniform moisture distribution on determination of hygroscopic swelling coefficient and finite element modeling for a flip chip package. In: *EuroSimE 2005. Proceedings of the 6th International Conference on Thermal, Mechanial and Multi-Physics Simulation and Experiments in Micro-Electronics and Micro-Systems, 2005*. Vol 2005. IEEE; 2005:112-119. doi:10.1109/ESIME.2005.1502784

8. Xiaosong Ma, Jansen KMB, Ernst LJ, van Driel WD, van der Sluis O, Zhang GQ. A new method to

measure the moisture expansion in plastic packaging materials. In: *2009 59th Electronic Components and Technology Conference*. IEEE; 2009:1271-1276. doi:10.1109/ECTC.2009.5074174

9. Khoshtinat S, Carvelli V, Marano C. Characterization and modeling the hygroscopic behavior of cellulose acetate membranes. *Cellulose*. Published online February 7, 2022:1-12. doi:10.1007/s10570-022-04450-8

10. Wong CP. *Moisture Sensitivity of Plastic Packages of IC Devices*. (Fan XJ, Suhir E, eds.). Springer US; 2010. doi:10.1007/978-1-4419-5719-1

11. Zhou J. Transient analysis on hygroscopic swelling characterization using sequentially coupled moisture diffusion and hygroscopic stress modeling method. *Microelectron Reliab*. 2008;48(6):805-810. doi:10.1016/j.microrel.2008.03.027

12. Shrestha S, Diaz JA, Ghanbari S, Youngblood JP. Hygroscopic Swelling Determination of Cellulose Nanocrystal (CNC) Films by Polarized Light Microscopy Digital Image Correlation. *Biomacromolecules*. 2017;18(5):1482-1490. doi:10.1021/acs.biomac.7b00026

13. Stellrecht E, Han B, Pecht M. MEASUREMENT OF THE HYGROSCOPIC SWELLING COEFFICIENT IN MOLD COMPOUNDS USING MOIRE INTERFEROMETRY. *Exp Tech*. 2003;27(4):40-44. doi:10.1111/j.1747-1567.2003.tb00122.x

14. Xuejun Fan. Mechanics of moisture for polymers: Fundamental concepts and model study. In: *EuroSimE 2008 - International Conference on Thermal, Mechanical and Multi-Physics Simulation and Experiments in Microelectronics and Micro-Systems*. IEEE; 2008:1-14. doi:10.1109/ESIME.2008.4525043

15. Xie B, Fan XJ, Shi XQ, Ding H. Direct Concentration Approach of Moisture Diffusion and Whole-Field Vapor Pressure Modeling for Reflow Process—Part I: Theory and Numerical Implementation. *J Electron Packag*. 2009;131(3):0310101-0310107. doi:10.1115/1.3144147

16. Teverovsky A. *Moisture Characteristics of Molding Compounds in PEMs.*; 2002. Accessed July 23, 2021. https://nepp.nasa.gov/DocUploads/B9C0B2A1-4C69-4CB5-94863C560CBB0B19/Moisture Characteristics 3-part NEPP report.doc

17. Wypych G. *Handbook of Polymers: Second Edition*. Elsevier Inc.; 2016. doi:10.1016/C2015-0-01462-9

18. Khoshtinat S, Carvelli V, Marano C. Moisture absorption measurement and modelling of a cellulose

acetate. *Cellulose*. 2021;28(14):9039-9050. doi:10.1007/s10570-021-04114-z

Appendix 5. 1. Image correlation

Figure AP5. 1 depicts a schematic representation of the specimen preparation and image analysis processes. The speckles needed for image analysis were created by spraying black paint from a distance of 50 cm on one side of a specimen while it was held inplane between two metal frames. An Alkyd (Alchide) base black paint (Talken ® A0031) with high surface hardness, resistance to scratches and peelings, and strong adherence to supports, which does not dissolve the cellulose acetate membrane, was employed. To decrease any potential sources of measurement error, such as paint droppings and/or migration, the dried painted membrane was cleaned with a soft tissue to remove poorly adhered speckles.

Specimens with the dimensions of a microscope glass slide (25.4 × 76.2 mm^2) were cut from the eligible area of the membrane. Early tests revealed that analyzing the whole specimen might produce considerable errors due to image distortion (perspective) and moisture absorption near corners. Therefore, square regions of (2 × 2 mm^2) were drawn near to the center, where image distortion and the likelihood of moisture absorption are the least.

The specimens were dried for 24 hours at 125 ° C, then they were placed between two microscope glasses and sealed around the edges. The IM-5MET inverted microscope (OPTIKA ®) equipped with Optikam PRO6 was used to observe the 2×2 mm^2 area of interest. Grayscale images of 2048 × 3072 pixels with the resolution of 72 Pixels/Inch were obtained from the area of interests (drawn squares). Images were analyzed using Image J 1.48 K software. Depending on the speckles in the obtained image a "default threshold" within the range of 145 to 160 on grey level histogram was applied. The applied threshold was maintained constant for the same area of interest in dry and humid conditions, to avoid any error, caused by the analysis procedure. For each area of interest, the microscope's focus was maintained constant. At least 10 speckles for each area of interest have been considered (numbered in green in the bottom right image in Figure AP5. 1). The center of the speckles was the reference point for the calculation of the distance. The hygroscopic strain was calculated by measuring the relative change of the distance between different spackle with respect to the dry condition ($\varepsilon_{hygro} = \frac{L_{sat} - L_{dry}}{L_{dry}}$).

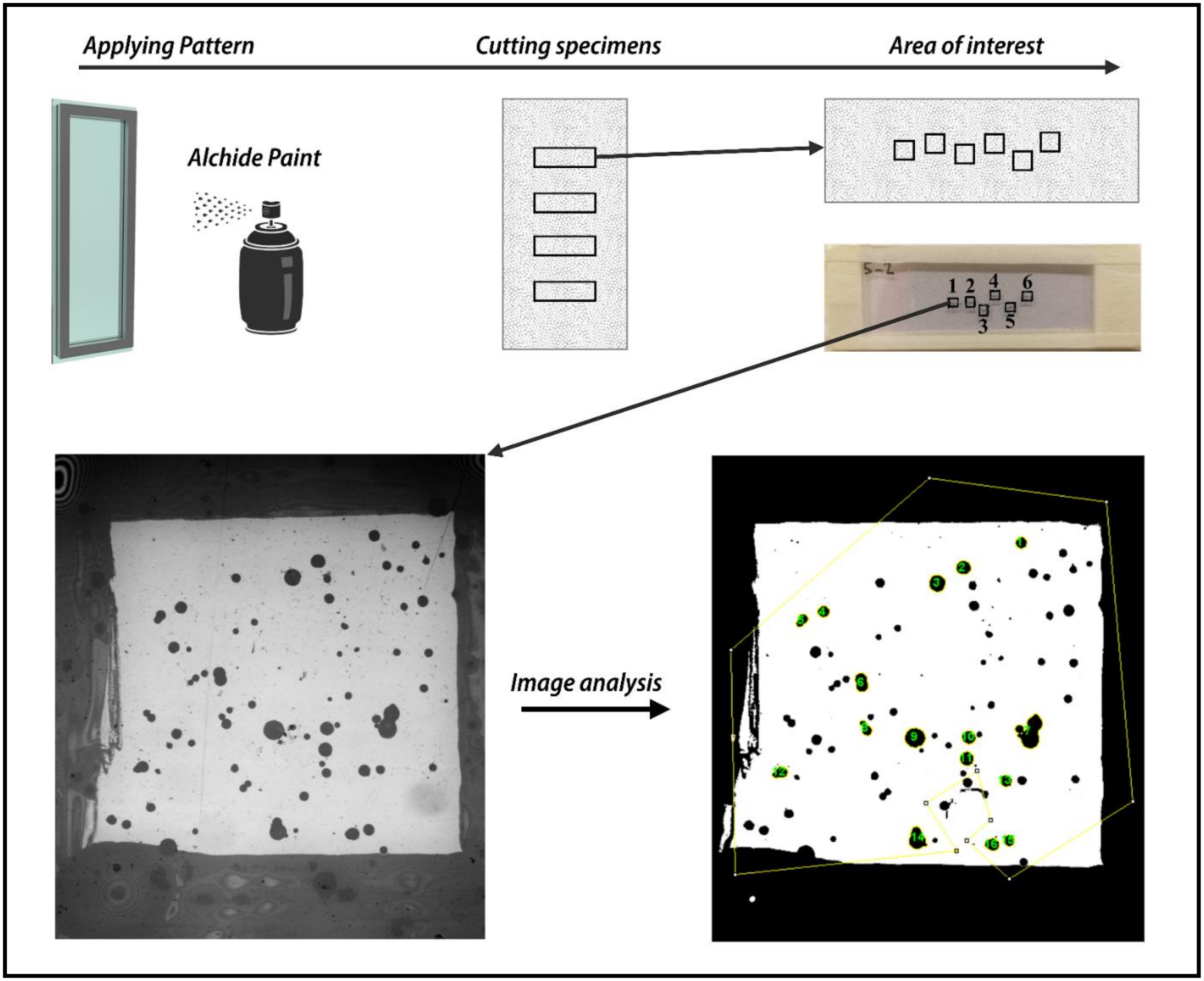

Figure AP5. 1. Illustration of the specimen preparation and image analysis procedures

Figure AP5. 2 (a) shows the results of image analysis for the determination of hygroscopic strain component, in the transverse and longitudinal directions to Doctor Blade's knife movement, for one of the specimens at relative humidity of 38%, . There has been no apparent trend in terms of orientation. As can be observed, the resulting values exhibit a high scatter with no discernible trend depending on the location toward the center or boundaries. Fifteen specimens from five different membranes, with at least six areas of interest per each specimen, have resulted in different values of strain at a constant relative humidity level.

To assess the impact of human error during the membrane sealing procedure, image analysis was performed on the same specimen three times by opening and closing the sealing. Figure AP5. 2 (b) depicts the results of these three image analyses for the same specimen at the same level of relative humidity as in Figure AP5. 2 (a). Hypothetically, by opening the seal and exposing the cellulose acetate to the room humidity level, the membrane must absorb the moisture from the environment and tend to expand. Thus, an increase from the first analysis to the third one would be expected for all the areas of interest. However, as can be seen, no substantial uniform trend is observed. The first area of interest shows a decrease in strain from the first to the third measurement. The second area, on the other hand, shows a fluctuation, while the fourth area remained almost constant. This finding suggests that by sandwiching the cellulose acetate membrane between two microscope glasses and sealing the boundary, an unforeseen force is induced in the membrane, which significantly alters the measurement's results. Moreover, the obtained results for hygroscopic strain by this technique are about two orders of magnitude below expectation for cellulose-based materials and the results for thermomechanical analysis presented in this chapter.

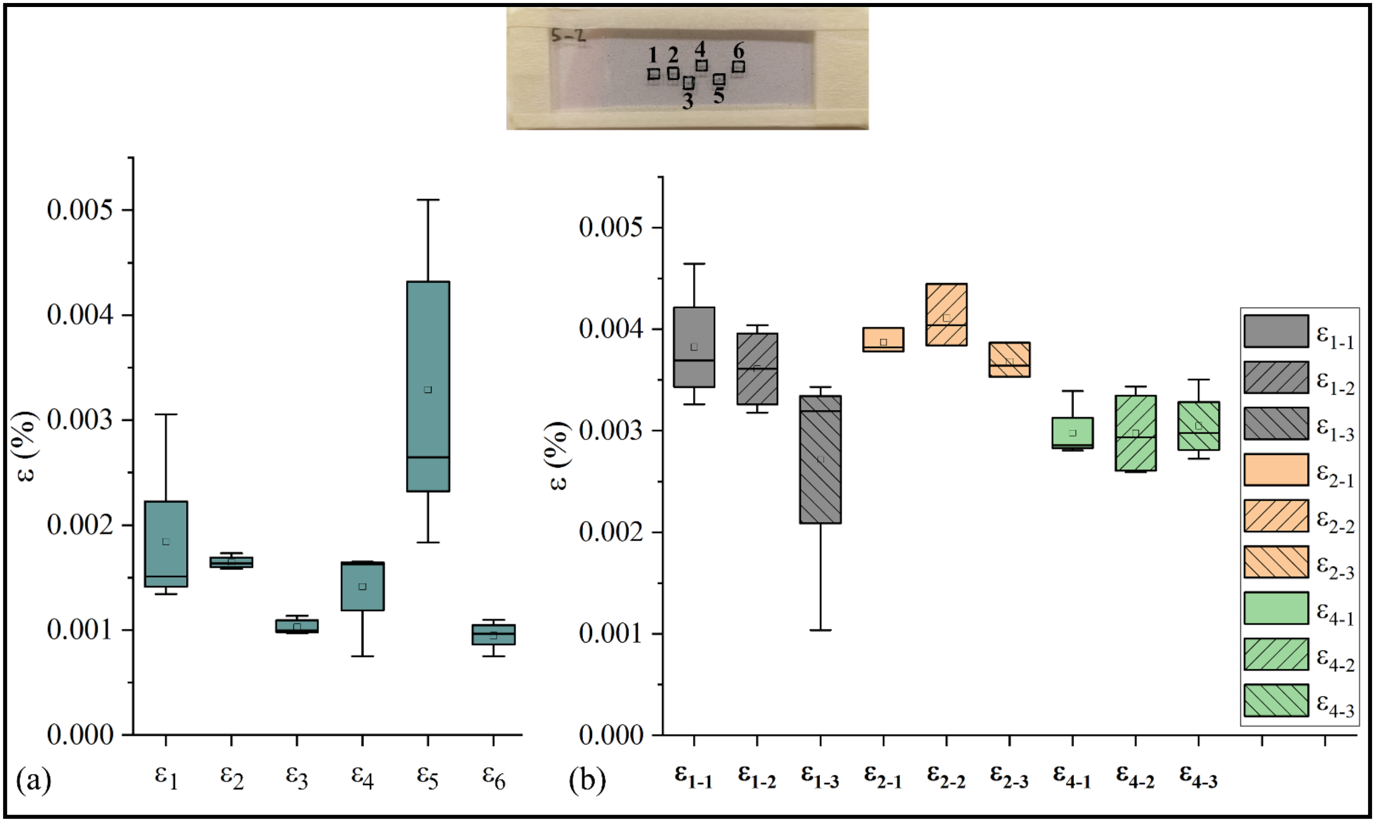

Figure AP5. 2. a) Hygroscopic strain determined by image analysis of a membrane in its dry and saturated condition reached after exposure to a relative humidity of 38 %, b) Hygroscopic strain determined by the same image analysis procedure for 3 areas of interest repeated 3 time, where the numbers in the subscript of ε refer to the number of the area and the repetition time, respectively. Hollow squares inside the boxes and the bars represent the mean value and variation range within 1.5 of the interquartile range IQR, respectively.

Appendix 5. 2. Thermomechanical analysis with macro-expansion probe

For this set of experiments, disk-shaped specimens were obtained from the CA casted membrane using a hallow punch. For 24 hours, several specimens differing in their thickness were submerged in distilled water. The thermomechanical investigation was carried out with the aid of a macro-expansion probe. As can be observed from Figure AP5. 3, each specimen's dimensional variation during the first heating ramp has a completely different trend. No trend correlated with the specimen thickness in the dimensional variation of the different specimens during the first heating ramp has been observed. Moreover, dimensional variation registered throughout the whole isothermal test period suggests that the specimens are still losing the absorbed moisture during this step of the test. The desorption process is slower than the one occurring under tensile loading conditions. This is due to the fact that the macro-expansion probe and the sample stage cover the upper and lower surfaces of the thin disk-shaped specimen, so that the moisture desorption occurs only through the lateral surface of the thin disk, taking more time.

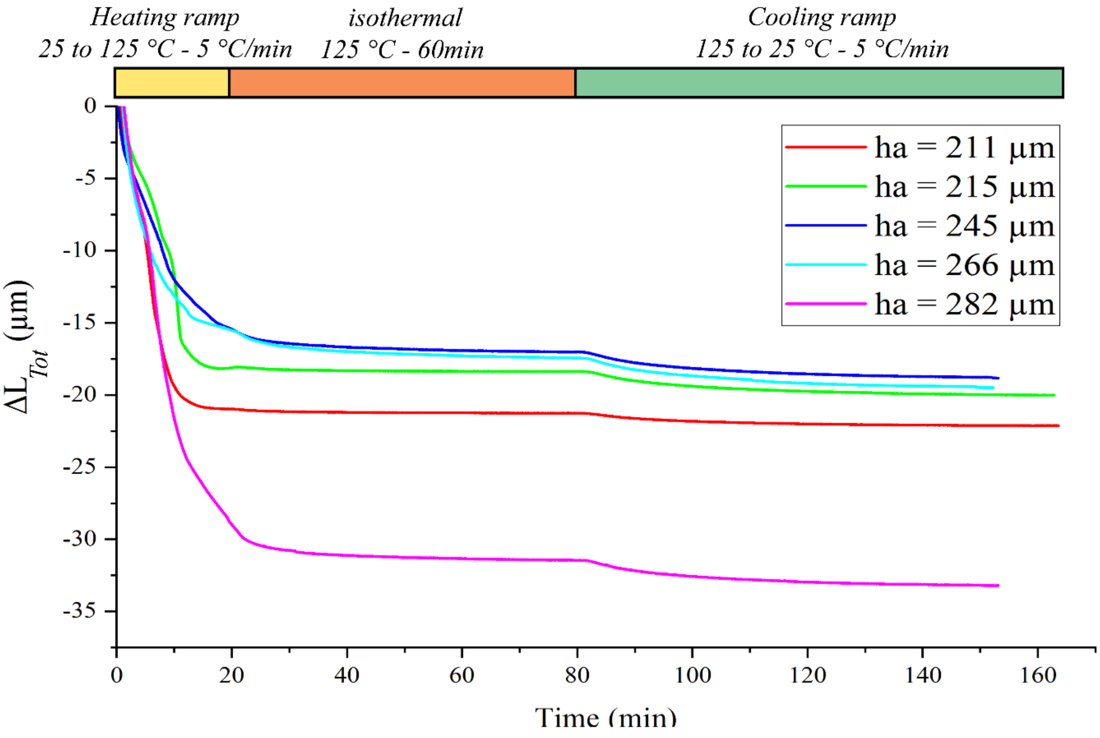

Figure AP5. 3. Thermomechanical analysis with macro-expansion probe

Appendix 5. 3. Thermomechanical Analysis experimental data

The mean values of length variation as a function of time and the standard deviation (semi-transparent regions) of Thermomechanical analysis for specimens with a gauge length of about 11 mm equilibrated at different relative humidity levels are provided below.

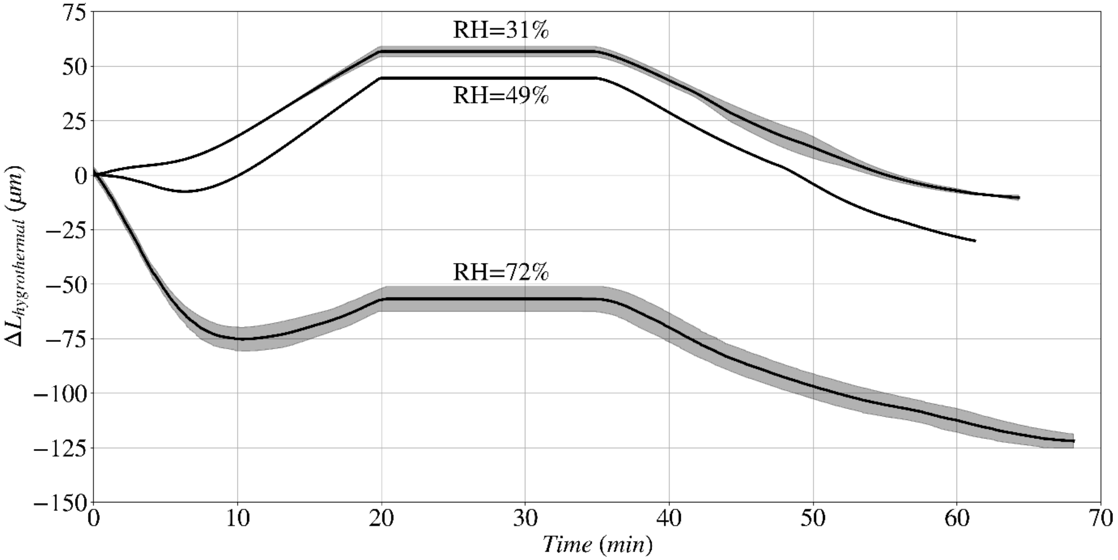

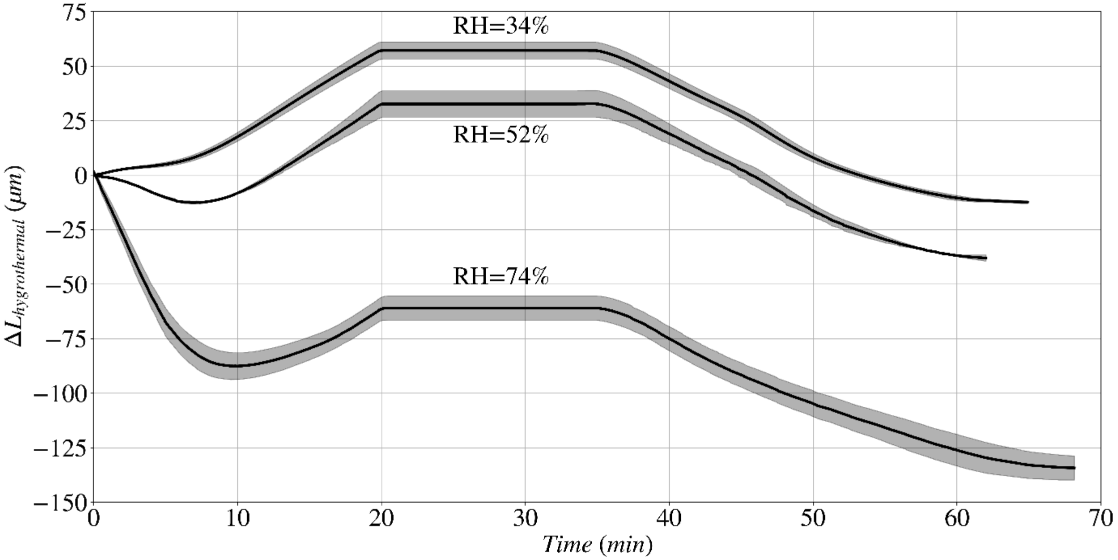

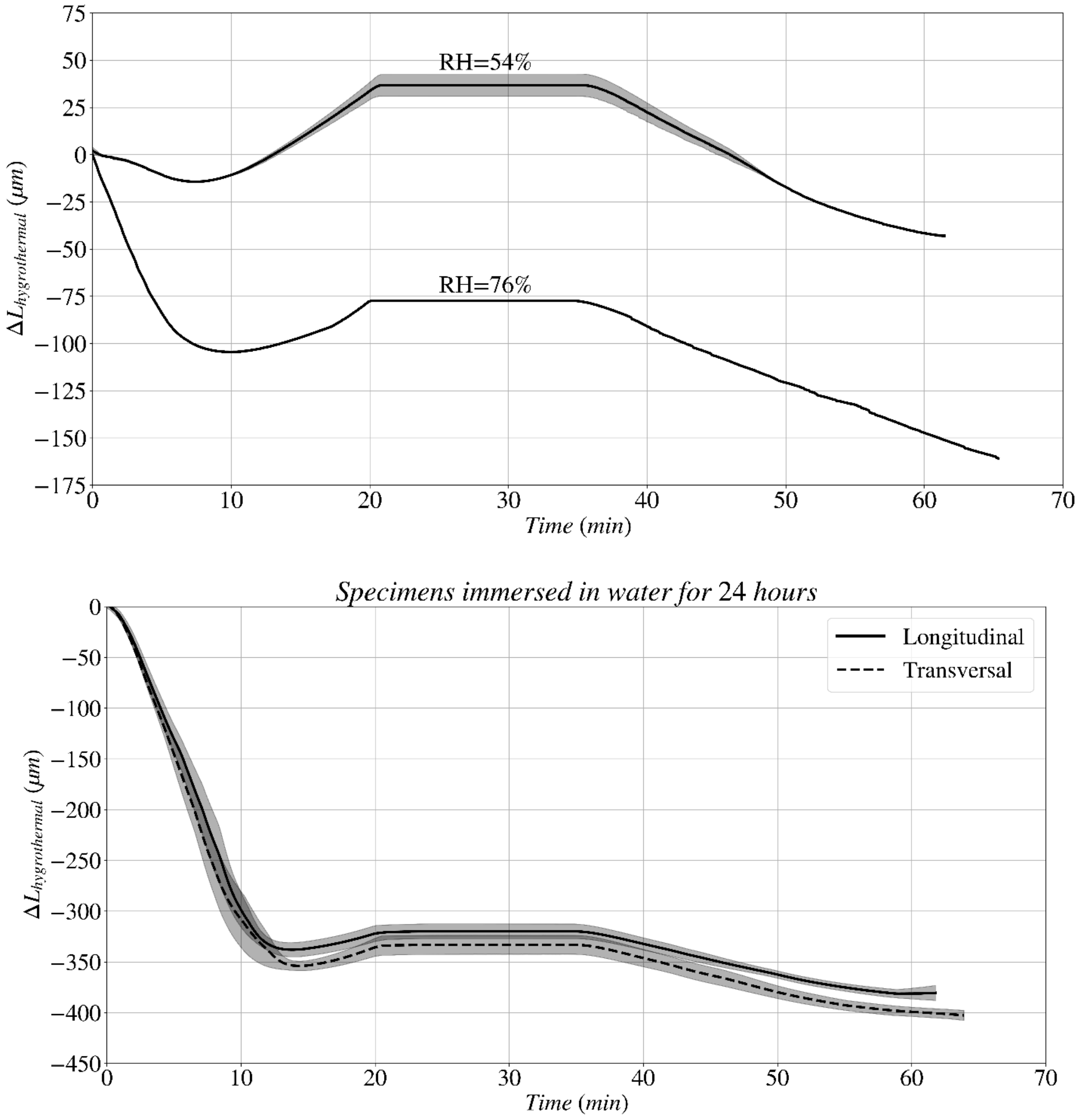

Figure AP5. 4. Complete set of Thermomechanical Analysis

Appendix 5. 4. Thermal expansion of cellulose acetate membrane

Thermal expansion of cellulose acetate membranes measured in longitudinal and transversal (with TA film-fiber Probe), and along the thickness (with macro-expansion Probe).

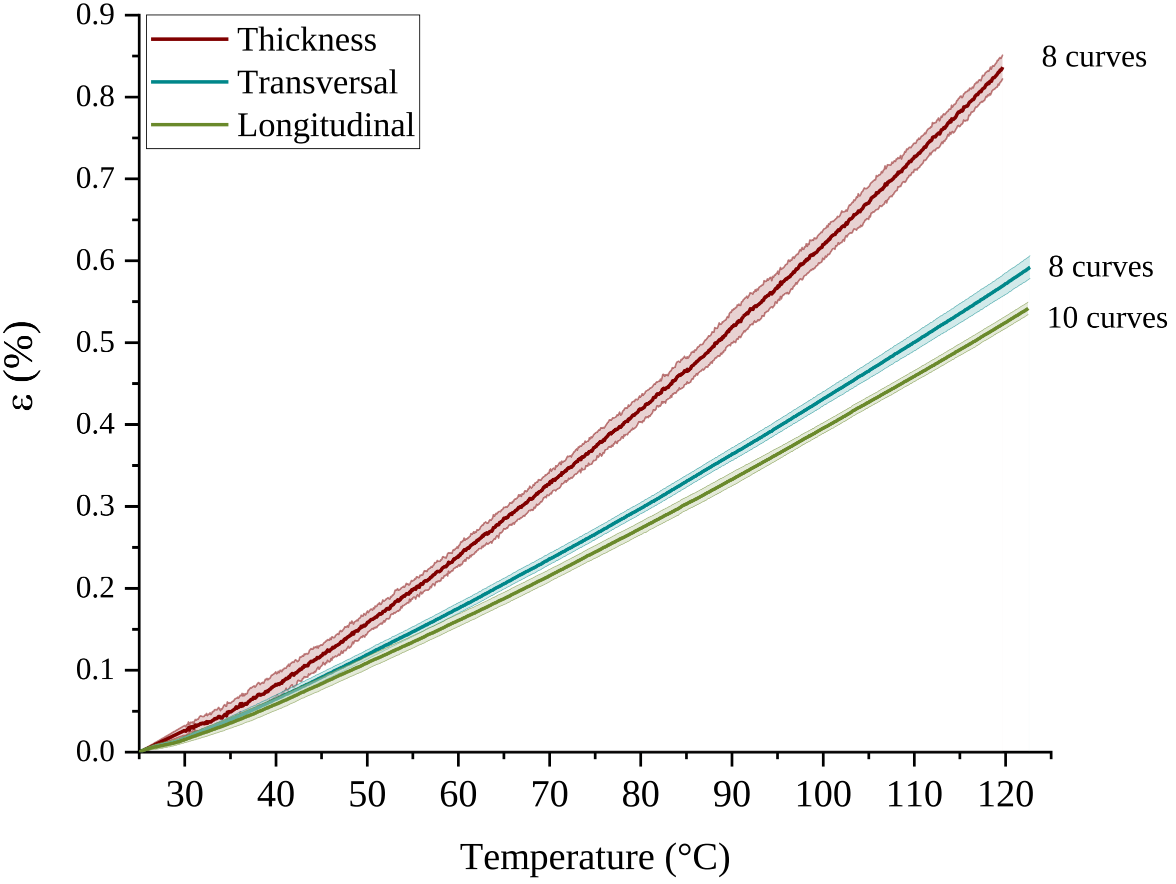

Figure AP5. 5. Thermal expansion of cellulose acetate membrane

6 Bending Deformation of Humidity-responsive Self-actuator

In this chapter, a study of the response to the variation in humidity level of a bi-layered composite formed by coupling the cellulose acetate membrane characterized in this work and a non-hygroscopic substrate is presented. The experimental setup and procedure for characterizing the bending of such a bilayer self-actuator using an image analysis technique are described in detail. The multiphysics finite element model for predicting the self-actuators' deformation is provided. The evolution in time of the bi-layered shape predicted by the finite element simulation and the experimental data are compared. The final bending curvature measured experimentally is compared to prediction of the finite element model and the bending cantilever analytical model.

6.1 Introduction

As discussed in the first chapter, the holistic idea of improving the level of comfort in currently used emergency shelters revolves around the development of humidity-responsive smart textiles by establishing layered self-actuators composed of currently used textiles as a passive layer and a hygroscopic material (cellulose acetate in this study) as an active layer without interfering with the manufacturing process and as a coating.

Due to the anti-adherent coating layer of these textiles, as well as the high wettability and inherently low surface energy of cellulose acetate [1], interfacial bonding between cellulose acetate and these textiles is weak. Although treatments such as chemical modification or plasma treatment can improve the adhesion of cellulose acetate, they may have an effect on the hygroscopic behavior by modifying the quantity or arrangement of the hydroxyl groups. However, the industrial manufacturing process is not the main objective of this research.

Therefore, the emphasis in this chapter is on demonstrating the validity of the multiphysics finite element model for describing the bending curvature of a bi-layered self-actuator using cellulose acetate as the active layer. Once the precision of finite element modeling is confirmed, the coating of the adopted textiles can be replaced by cellulose acetate, during the design phases.

For this purpose, a non-hygroscopic substrate that meets the geometrical and material criteria for the bi-layered substrate is employed. An image correlation approach adopted in literature [2–7] is used to track the change of bending curvature over time. It should be noted that only few studies examined the change of bending curvature over time [2,4,6] and compared the final deformation with bending cantilever analytical model (Equation (2.3)) considering a constant value for coefficient of hygroscopic expansion. Appendix 6. 1 provides a parametric study of this analytical model considering a humidity-dependent coefficient of hygroscopic expansion obtained in this thesis based on Equation (5.3).

6.2 Bending cantilever experiments

6.2.1 Preparation of the bilayered

According to the theoretical background described in chapter 2 (Section 2.6), for the validity of the bending cantilever analytical model, the geometry of the bi-layered composite and the substrate layer material properties must meet certain requirements . Berry and Pritchet's [8] assumptions for the analytical model, in particular, must be taken into account. Therefore, the substrate must be thicker than the CA membrane ($h_p > h_a$), have a negligible hygroscopic property (coefficient of hygroscopic expansion) compared to cellulose acetate ($\alpha_p \ll \alpha_a$), and be humidity resistant with good adhesion to the CA membrane.

As for the substrate, an adhesive tape (Tesa ® 64621) that meets all the requirements was chosen. Tesa ® 64621 is a double-sided adhesive tape with a polypropylene carrier and a synthetic rubber adhesive that is not hygroscopic and provides excellent adhesion to both polar and non-polar surfaces. The adhesive layer of this tape is transparent and has a very low stiffness. The low stiffness of the substrate in these bi-layered may lead to a non-reversible deformation if the induced deformation by the active layer in the substrate exceeds the linear elastic regime. To increase the rigidity of the substrate layer, the release liner (made of silicone-coated paper) was maintained. This improved also the visibility of the bi-layered composite for the image analysis. The adhesive tape, including its release liner (thickness h_p = 145 ± 1 μm) was treated as a homogenous substrate. Uniaxial tensile tests were performed on the adhesive tape at the same conditions adopted for the cellulose acetate membrane tensile testing (strain rate 6×10^{-3} 1/min, T=25± 1 °C). A Young's modulus of 4.62 ± 0.03 GPa was evaluated.

Preliminary attempts to apply the adhesive tape to the CA membrane, soon after it was removed from the oven (24 h, 125 °C drying procedure), highlighted a curvature in the composite due to thermal shrinkage (cooling from 125 °C to room temperature) and hygroscopic expansion at the membrane's surface during the adhesion time (almost 30 seconds). This would be avoided if the composite was assembled in a dry environment, which is not available for this research. The most feasible strategy is to couple the layers in a climatized chamber at a specified relative humidity, with the cellulose acetate membrane at its saturation state. Therefore, the coupling of adhesive tape (h_p = 145 ± 1 μm including the release liner) with three different equilibrated cellulose acetate membranes (h_a = 86 ± 3 μm) was performed in the climatized room (T=25 °C, RH = 35%). Then, three specimens of 60×12.5 mm^2 were hollow punched.

6.2.2 Experimental setup

A polymethylametacrylate close chamber (schematically depicted in Figure 6. 1) has been designed and fabricated to control the relative humidity of the environment. Different levels of relative humidity of 17, 77, and 80% were achieved within the closed chamber at room temperature (T = 25 ± 1 °C) using dry silica gels or salt solutions of sodium chloride in distilled water. The gels or salt solution were placed in the chamber 72 hours in advance to stabilize the relative humidity. To examine reproducibility, three specimens were obtained from three distinct cellulose acetate membranes with the same thickness of 86 ± 3 μm.

Table 6. 1. Bi-layered specimens' geometry at 25 °C and RH = 35% and experimental conditions.

$Specimen$	$Overhang$ L (mm)	$Thickness$ h (mm)		$Width$ w (mm)	RH (%) [from-to]
		CA	Tesa ® 64621		
$S1$	50	0.086	0.145	12.5	[17-80], [35-80]
$S2$	40				[35-77]
$S3$	40				[17-77], [35-77], [35,80]

The experimental setup for acquiring images at constant relative humidity and temperature (T= 25 °C) is depicted schematically in Figure 6. 1. The induced bending deformation of such a bi-layered self-actuator was measured by image analysis of digital images captured during the tests. A digital camera (Nikon D70) was placed perpendicular to the millimeter paper, about 50 cm away from the tested specimen. The acquisition frequency of 0.016 Hz (one image every minute) was set. The specimen (60 mm length) was clamped between two metal supports, leaving an overhanging length of 40 or 50 mm, and it was put with one side (corresponding to the continuous blue line in Figure 6. 2) close to the graph paper background, oriented in such a way that the cellulose acetate membrane always facing down. Approximately one minute was required to adjust the specimen within the chamber. The time for a 86 μm thick dry cellulose acetate membrane to attain saturation at a relative humidity of 80 % has been determined using finite element simulation (Section 4.4) to be roughly 60 minutes when absorption occurs from only one of its surfaces. Given the relative humidity of the climatized room (RH = 35%) which plasticizes the membrane, a longer time for the experimental observation was considered, and the evolution of bending of the bi-layered self-actuator was recorded for 100 minutes.

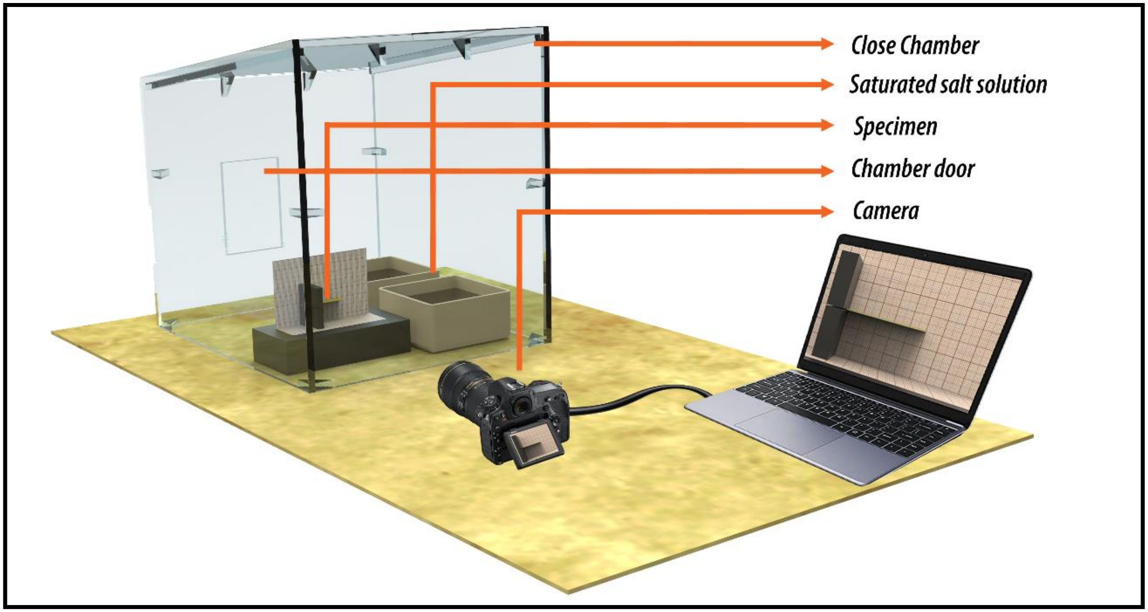

Figure 6. 1. Schematic illustration of the experimental setup

Figure 6. 2 depicts, as an example, the picture of specimen S1 equilibrated at 80% relative humidity together with the adopted reference system for curvature measurement. Some of the obtained digital images of bending curvature for this specimen at different time are presented in Appendix 6. 2. The recorded digital images were imported in Rhinoceros® as a "picture frame". The images were rescaled to have a 1:1 scale in millimeters units of the program and millimeter paper in the imported image. Some minor unexpected twists were observed as the different curvatures of the two sides (continuous and dotted blue lines), which might be attributed to thickness variation of CA membrane (3 μm) or imperfection of CA membrane adherence to substrate during manual application. To avoid any error related to twist, the $X - Y$ reference frame's origin was placed at the closest location to the millimeter paper where the specimen is clamped between the metal supports ($P0$). The specimen's bent curvature was approximated by an arc passing through point $P0$ to point $P1$ along the bi-layered, with $tan(P0) = 0$ (continuous blue line). Equation (6.1) was used to calculate the bending curvature (κ), where x and y are the coordinates of $P1$ (see Figure 6. 2). This procedure was carried out on all of the obtained frames for each specimen.

$$\kappa = \frac{1}{R} = \frac{2x}{y^2 + x^2} \tag{6.1}$$

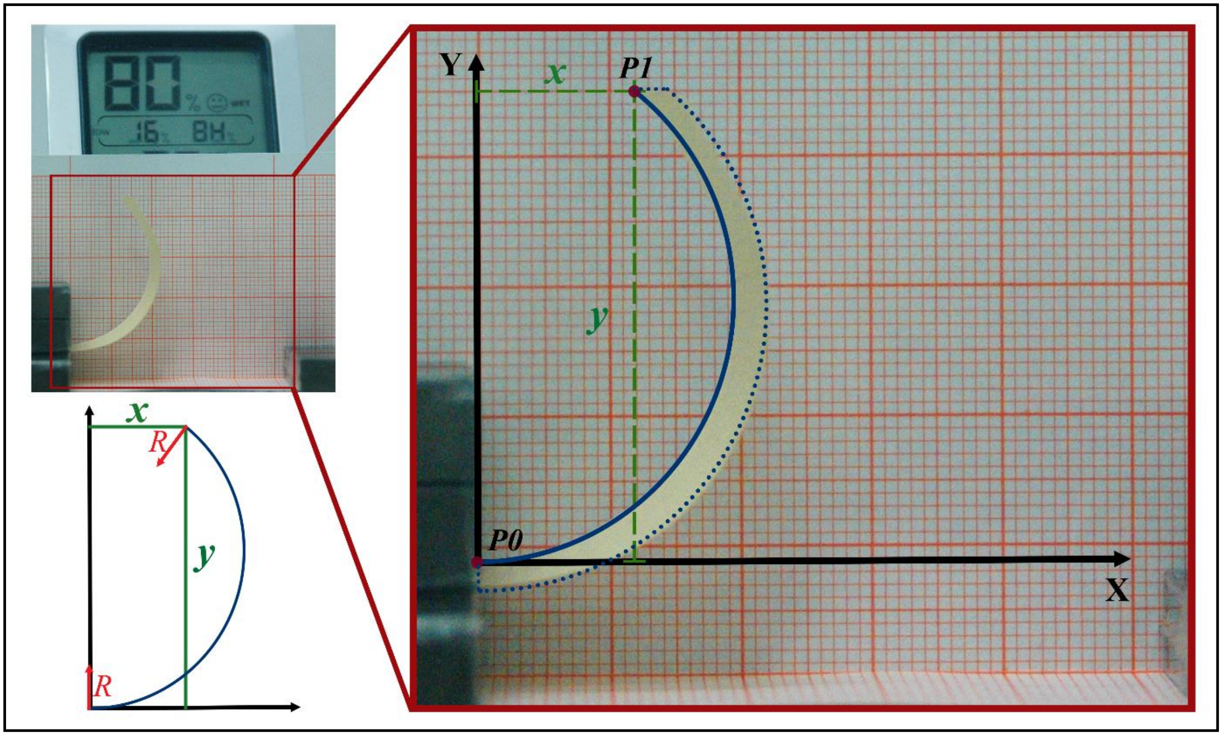

Figure 6. 2. A digital image of Specimen S1 after 100 minutes of exposure to relative humidity of 80 % in the closed chamber (continuous blue line is the considered arc for the calculation of the bending curvature and the dotted blue line is the effect of the slight twist).

6.2.3 Experimental results

Figure 6. 3 depicts the experimental findings of bending curvature (κ) progression in time caused by relative humidity variations for specimens initially equilibrated at RH = 35% and then put in the closed room at RH = 77 or 80%. As expected, the ultimate generated bending curvature in the bilayer rises as a result of an increase in relative humidity. The first point on these graphs shows the bending curvature of the bilayer after one minute of exposure to the relative humidity (77 or 80 %), corresponding to the first image acquired by the camera.

The repeated values of the initial points of these trials, starting with a flat specimen in a climatized room condition (RH=35 %), show the repeatability of the procedure. The bending curvature develops fast over the first 20 minutes. Following this interval, the rate declines progressively up to 40 minutes. The curvature then approaches the plateau between 40 and 60 minutes. After 60 minutes, the curvature shows that the moisture absorption process is complete. It should be emphasized that the observed behavior is comparable to moisture diffusion as a function of time [9,10], highlighting the role of moisture absorption in bending curvature.

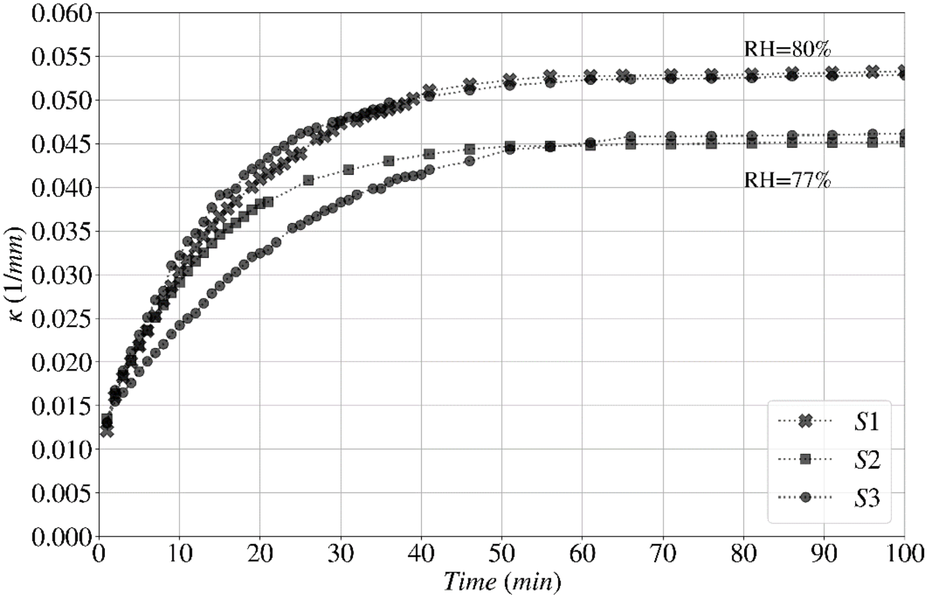

Figure 6. 3. Experimental results of bending curvature of bilayer self-actuators in response to changes in relative humidity

To evaluate the influence of initial relative humidity on bending curvature and the cyclic behavior of these self-actuators, specimens were partially dried for 24 hours in a closed chamber containing silica gel (RH = 17 %), resulting in a negative bending curvature of -0.0199 (see Appendix 6. 3). They were then immediately placed in the closed chamber showed in Figure 6. 1 with a higher value of relative humidity. Figure 6. 4 reports the bending evolution of a specimen ($S1$) preliminary equilibrated at RH = 35% that was (i) exposed to RH = 80 % for 100 min (first step), (ii) dried for 24 h at RH = 17% and (iii) fast exposed again to RH = 80 % for further 100 min (second step). Similar results are reported in Figure 6. 5 for the samples $S3$, that was exposed to a humidity of 77 %. As expected, regardless of the starting relative humidity (17 or 35 %), the ultimate bending curvature is consistent for tests performed at the same relative humidity, RH = 80% for $S1$ and RH = 77% for $S3$. The initial relative humidity, on the other hand, determines the first bending curvature obtained 1 minute after exposure as the first point produced by the first image. The bending curvature of the bilayer after 1 minute of exposure resulted in a lower value for both specimens for the lower initial humidity level 17 %. This effect is due to the difference in the initial bending curvature, as the initial bending curvature for the specimen stabilized at RH = 35% is κ = 0, but the starting bending curvature for the identical specimen stabilized at RH = 17% is κ = -0.0199.

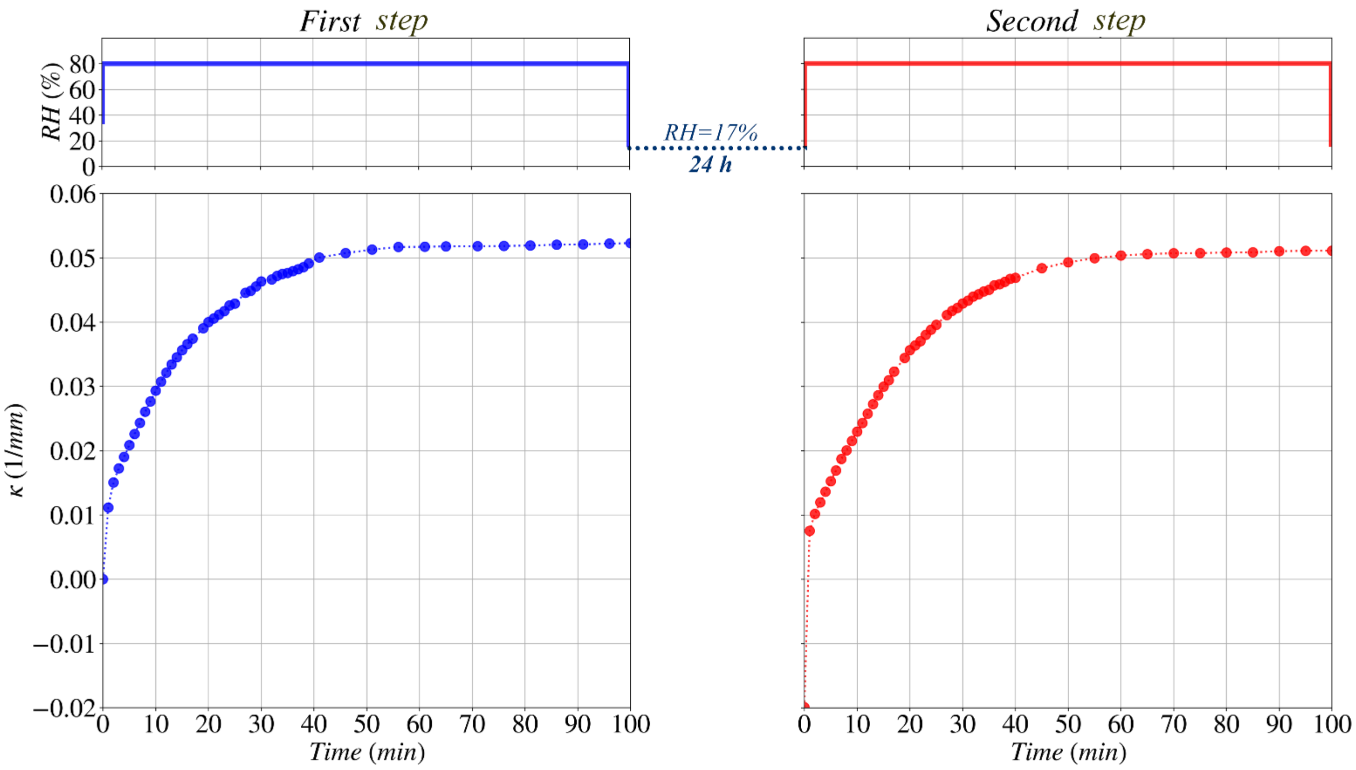

Figure 6. 4. Evolution of bending curvature in time in cyclic variation of relative humidity for specimen *S1*

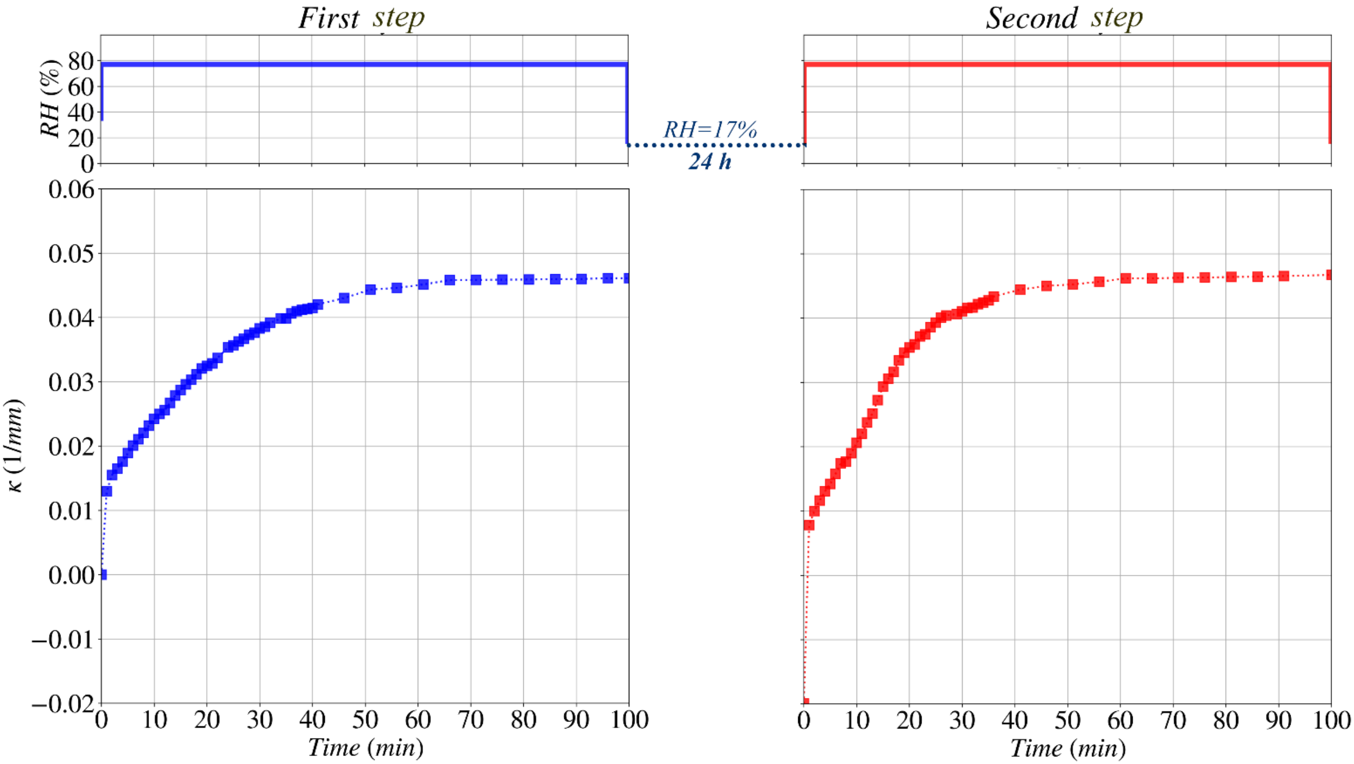

Figure 6. 5. Evolution of bending curvature in time in cyclic variation of relative humidity for specimen *S3*

6.3 Finite element modeling

Figure 6. 6 illustrates some features of the multiphysics finite element model built in COMSOL Multiphysics ® 5.6. Three geometric parameters were held constant in the numerical analyses: the composite width (W = 12.5 mm) and the thickness of both active and passive layers (h_a = 0.086 mm, h_p = 0.145 mm). The composite length (L) has been varied based on overhanging length of each tested specimen as presented in Table 6. 1. Two 3D prismatic layers, one for the cellulose acetate membrane ($L \times W \times h_a$) and the other for the substrate ($L \times W \times h_p$) have been defined. To ensure continuity at the interface, the two layers were regarded as perfectly connected by a tie constraint. Material properties such as density (ρ), Young's modulus (E), Poisson's ratio (ν), relaxation factor (β), and the diffusion coefficient (D) were used to create two user-defined materials for the layers, see Table 6. 2. The mechanical properties are assumed unaffected by the environment relative humidity. The concentration at saturation (C_{sat}) and the coefficient of hygroscopic expansion (α) for cellulose acetate membrane has been defined as function of relative humidity (RH) according to Equation (4.3)and Equation (5.3), respectively.

Table 6. 2. Materials' properties values used for the finite element simulations.

Materials	$\rho\ (g/cm^3)$	$E\ (GPa)$	$\nu\ (-)$	$\beta\ (1/s)$	$D\ (mm^2/s)$
Cellulose Acetate	1.3 [11]	1.1[12]	0.39 [11]	0.026 [13]	3.35×10^{-6} [13]
Tesa ® 64621	1.35	4.64	0.33		

The bending deformation in the bi-layered self-actuator is caused by a mismatch in the linear hygroscopic expansion of the active layer (cellulose acetate) and the passive layer ($\varepsilon_{hygro\ (passive)}$= 0). The hygroscopic expansion in cellulose acetate, however, is the result of deformation by the moisture absorption. Therefore, a multiphysic approach considering two phenomena of moisture diffusion and mechanical deformation was adapted. The input parameters for the diffusion process were set only for the active layer (cellulose acetate membrane) considering a non-Fickian behavior [14]. For the initial dry condition, a null initial moisture concentration (C_0 = 0 g/mm^3) was considered. The concentration boundary condition as the function of time

($C_t = C_{sat}(1 - e^{-\beta t})$) was imposed on the faces of cellulose acetate membranes that were exposed to humid environment.

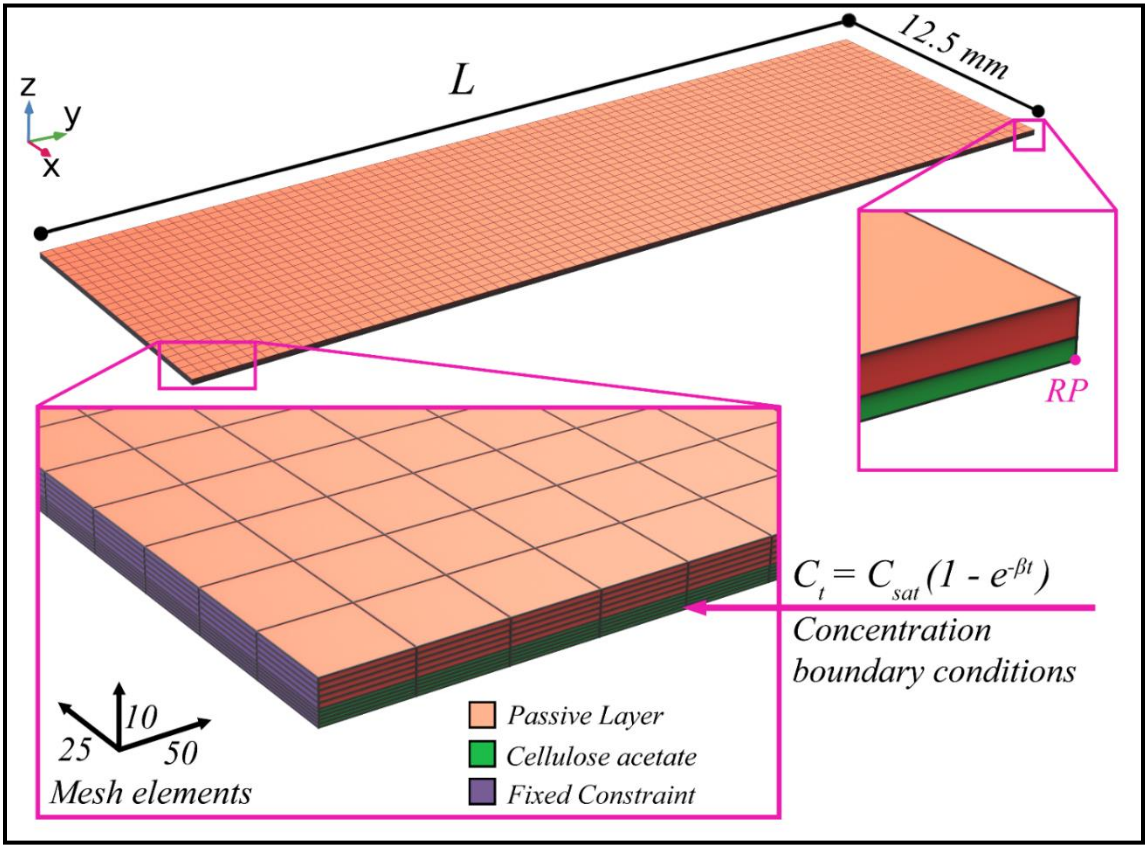

Figure 6. 6. Details of the finite element model

To replicate the cantilever, an exterior face of the model was fixed along its width. A user-controlled sweeping mesh was produced from the top face of the passive layer (adhesive tape) to the bottom face of the cellulose acetate membrane, generating a discretized volume by 25 × 50 × 10 hexahedral elements (total of 12500 finite elements).

To save computational time, two time-dependent multiphysics analyses, one for the diffusion process and the other hygroscopic swelling were established instead of a single one that incorporated all physical processes. A time range of 100 minutes was set for both analyses. First, the diffusion process was simulated. Then, by referring to the output of the diffusion analysis and including geometric nonlinearity, the simulation for the hygroscopic swelling was performed. A built-in function that considers the displacement of one external node (RP in Figure 6. 6) determined the evolution of the bending curvature of the modeled self-actuator over time. It should be noted that the influence of the specimen and absorbed moisture mass on bending deformation is neglected in the simulation.

6.4 Results and comparisons

Figure 6. 7 (a) portrays, as an example, the prediction of finite element modeling for the deformation of the self-actuator due to the moisture absorption, simulated for a completely dried specimen (RH = 0%) with the same geometry as $S1$ at a relative humidity of RH = 80%. The overlapping of the curves reproducing the self-actuator shape at 60 and 70 minutes suggests that no more deformation is occurring in this period, implying that the moisture diffusion process in the cellulose acetate membrane has already ended. Additionally, it demonstrates the self-actuator's rapid response to variations in relative humidity. The actuator deforms significantly during the first two minutes of exposure to the greater relative humidity level, indicating that this self-actuator can be used for applications such as indoor humidity management, as reported in some literature [3,4,15,16].

The experimental and numerical final shape of the $S1$ specimen are compared in Figure 6. 7 (b). The discrepancy between the two final shapes is due to the fabrication of the bilayer at a relative humidity of 35%, which caused a hygroscopic expansion of the cellulose acetate membrane. As stated in section 4, it was not feasible to achieve a relative humidity of 0% in the laboratory, and the adhesive tape-based passive layer was connected to the cellulose acetate membrane at the room's relative humidity (RH = 35%). Due to the fact that the bending curvature at equilibrium is independent of diffusion kinetics, the curvature induced by a variation in humidity from dry condition (RH = 0%) to RH = 80 % is equal to the sum of the curvatures from 0% to 35 % and 35 % to 80 % of relative humidity [4]. Thus, the variation of bending curvature from the relative humidity of 35% to 80 % ($\Delta\kappa_{RH(35-80)}$) can be retrieved by:

$$\Delta\kappa_{RH(35-80)} = \kappa_{RH(0-80)} - \kappa_{RH(0-35)} \tag{6.2}$$

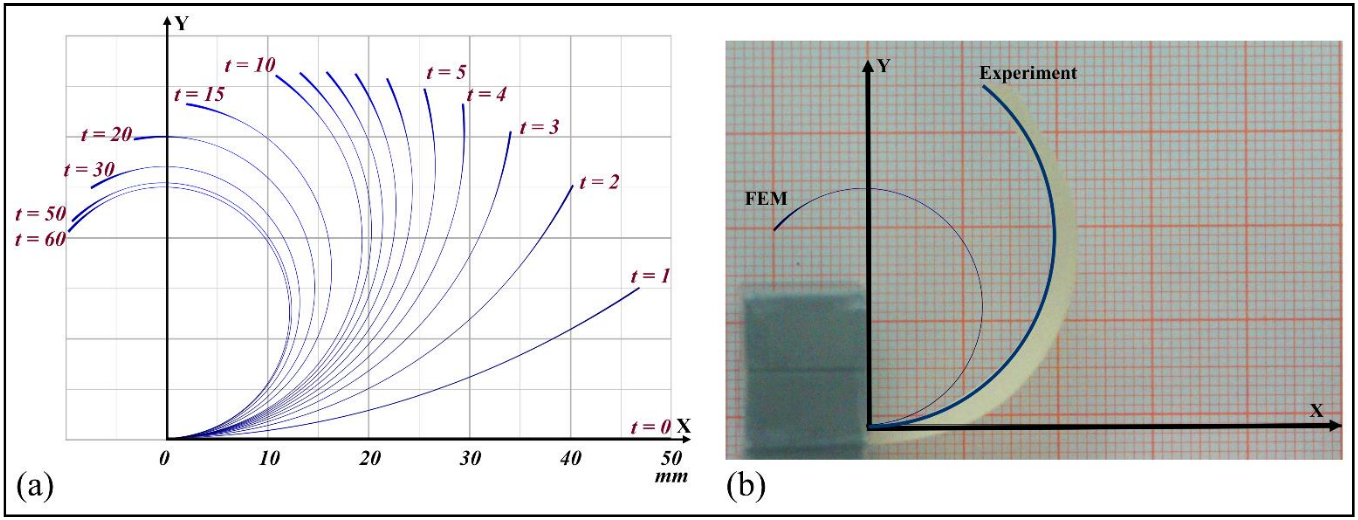

Figure 6. 7. (a) Finite element simulation of self-actuator deformation; (b) Comparison of final deformation between experimental data and numerical model for specimen equilibrated at RH = 80% (Staring relative humidity for the simulation and the experiment are 0% and 35%, respectively)

Figure 6. 8 compares the evolution of the bending curvature in time for the experiment and the numerical simulation for the specimen $S1$ equilibrated at 35 % relative humidity and placed at $RH = 80\%$. Additionally, the analytical model prediction for the ultimate bending curvature (Equation (2.3)) is compared using the relative humidity dependent coefficient of hygroscopic expansion (Equation (5.3)) and the values n = 3.84, m = 1.69, and h_{tot} = 0.228 mm (Table 6. 1 and Table 6. 2). Both the numerical and analytical predictions have been adjusted according to Equation (6.2). Figure 6. 8 illustrates that experimental bending curvature grows at a slower rate than finite element model. This finding might be attributed to the fact that the experiment's starting condition was RH = 35%. At his RH the cellulose acetate has a slightly lower diffusion coefficient than the dry cellulose acetate since it has been partially plasticized by the absorbed moisture.

The experimental results and the finite element simulation agree very well in terms of the ultimate bending curvature. The finite element calculation anticipated a bending curvature of about κ = 0.0519 1/mm (R = 19.26 mm), while the experiment exhibited a value of κ =0.0511 1/mm (R = 19.56 mm). The difference of merely 0.3 mm tend to be relatively acceptable. In contrast, the analytical model provided a curvature of 0.0645 1/mm

(R=15.5 mm), resulting in a 3.43 mm discrepancy in bending radius to the experiment. The analytical model's overestimation of curvature is due to its simplifications and assumptions.

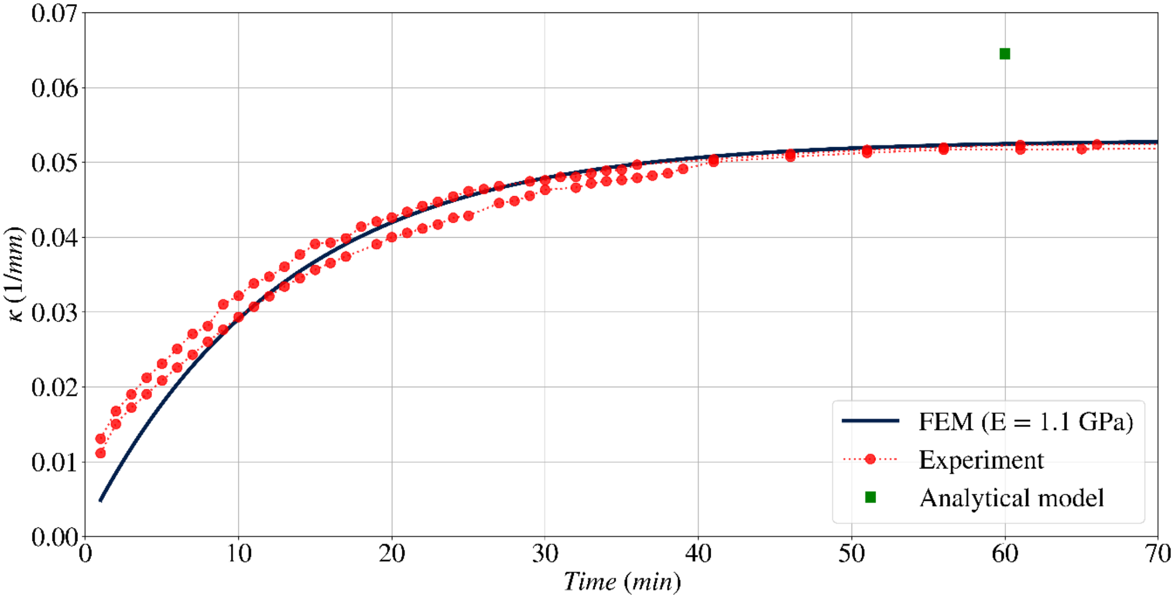

Figure 6. 8. Comparison of experimental data, analytical and numerical models.

References

1. Heinze T, El Seoud OA, Koschella A. Cellulose Derivatives. Published online 2018. doi:10.1007/978-3-319-73168-1

2. Reyssat E, Mahadevan L. Hygromorphs: from pine cones to biomimetic bilayers. *J R Soc Interface*. 2009;6(39):951-957. doi:10.1098/rsif.2009.0184

3. Correa D, Papadopoulou A, Guberan C, et al. 3D-Printed Wood: Programming Hygroscopic Material Transformations. *3D Print Addit Manuf*. 2015;2(3):106-116. doi:10.1089/3dp.2015.0022

4. Holstov A, Bridgens B, Farmer G. Hygromorphic materials for sustainable responsive architecture. *Constr Build Mater*. 2015;98:570-582. doi:10.1016/j.conbuildmat.2015.08.136

5. Vailati C, Bachtiar E, Hass P, Burgert I, Rüggeberg M. An autonomous shading system based on coupled wood bilayer elements. *Energy Build*. 2018;158:1013-1022. doi:10.1016/j.enbuild.2017.10.042

6. Abdelmohsen, Sherif; Massoud, Passaint; El-Dabaa, Rana; Ibrahim, Aly; Mokbel T. A Computational Method for Tracking the Hygroscopic Motion of Wood to develop Adaptive Architectural Skins. In: *Proceedings of the 36th International Conference on Education and Research in Computer Aided Architectural Design in Europe*. Vol 2. ; 2018:253-262. Accessed December 21, 2021. http://ecaade.org/downloads/eCAADe-2018-Volume2.pdf

7. Dingler C, Müller H, Wieland M, Fauser D, Steeb H, Ludwigs S. From Understanding Mechanical Behavior to Curvature Prediction of Humidity-Triggered Bilayer Actuators. *Adv Mater*. 2021;33(9). doi:10.1002/ADMA.202007982

8. Berry BS, Pritchet WC. Bending - Cantilever Method for the Study of Moisture Swelling in Polymers. *IBM J Res Dev*. 1984;28(6):662-667. doi:10.1147/rd.286.0662

9. Mensitieri G, Scherillo G. Environmental Resistance of High Performance Polymeric Matrices and Composites. In: *Wiley Encyclopedia of Composites*. John Wiley & Sons, Inc.; 2012. doi:10.1002/9781118097298.weoc074

10. Hansen CM. The significance of the surface condition in solutions to the diffusion equation: explaining

"anomalous" sigmoidal, Case II, and Super Case II absorption behavior. *Eur Polym J*. 2010;46(4):651-662. doi:10.1016/j.eurpolymj.2009.12.008

11. Wypych G. *Handbook of Polymers: Second Edition*. Elsevier Inc.; 2016. doi:10.1016/C2015-0-01462-9

12. Khoshtinat S, Carvelli V, Marano C. Characterization and modeling the hygroscopic behavior of cellulose acetate membranes. *Cellulose*. Published online February 7, 2022:1-12. doi:10.1007/s10570-022-04450-8

13. Khoshtinat S, Shirvani Dastgerdi A. Inspirations from nature as a Method for Sustainable Architectural Design. In: *4th. International Congress on Civil Engineering Architecture and Urban Development*. ; 2016. https://www.civilica.com/Paper-ICSAU04-ICSAU04_1448.html

14. Khoshtinat S, Carvelli V, Marano C. Moisture absorption measurement and modelling of a cellulose acetate. *Cellulose*. 2021;28(14):9039-9050. doi:10.1007/s10570-021-04114-z

15. Menges A, Reichert S. Performative Wood: Physically Programming the Responsive Architecture of the HygroScope and HygroSkin Projects. *Archit Des*. 2015;85(5):66-73. doi:10.1002/ad.1956

16. Reichert S, Menges A, Correa D. Meteorosensitive architecture: Biomimetic building skins based on materially embedded and hygroscopically enabled responsiveness. *Comput Des*. 2015;60:50-69. doi:10.1016/j.cad.2014.02.010

Appendix 6. 1. Parametric study of the bending cantilever model

A parametric study of Berry and Pritchet's [8] bending cantilever analytical model (Equation (2.3)) is presented here to provide a better understanding of the effect of layers' thickness ratio (m), bi-layer composite overall thickness (h_{tot}), and materials stiffness ratio (n) on both the function f and the bending curvature κ, considering a humidity-dependent coefficient of hygroscopic expansion (α), see Equation (5.3).

$$\frac{1}{R} = \kappa = \frac{\Delta\alpha\ \Delta C\, f(m,n)}{h_{tot}}\ ,\quad f(m,n) = \frac{6(1+m)^2}{3(1+m)^2 + (1+mn)(m^2 + \frac{1}{m})}$$

$$h_{tot} = h_a + h_p\ , \qquad m = \frac{h_p}{h_a}, \qquad n = \frac{\acute{E}_p}{\acute{E}_a}\ , \qquad \acute{E}_a = \frac{E_a}{(1-\upsilon_a)}\ , \qquad \acute{E}_p = \frac{E_p}{(1-\upsilon_p)}$$

Figure AP6. 1 (a) portrays the effect of materials stiffness ratio (n) and layers' thickness ratio (m) on the function f. Since the one of the main assumptions of this model is that the active layer must be thinner than the passive layer ($h_a < h_p$), the minimum value of $m = \frac{h_p}{h_a}$ has been assumed equal to 1. The values of m were varied from 1 to 25, and seven distinct constant values of n were studied. As can be observed, increasing the stiffness of the passive layer (raising n), the function f reduces, which causes a decrease in bending curvature (κ) or an increase in bending radius (R).

Figure AP6. 1 (b) depicts the effect of materials stiffness ratio (n) on bending curvature (κ). Default settings of 1 GPa for $\acute{E}_a$ and 100 µm for active and passive layers thicknesses ($h_a = h_p = 100\mu m \rightarrow m = 1$) were used. Curvature dependence on relative humidity estimated for different n values is insignificant for humidity levels below 40%. For humidity levels above 40 %, on the other hand, the bending curvature of the bilayer self-actuator declines by the increase of stiffness ratio (n). This figure indicates that, when the bi-layer composite constituents have the same thickness for the same hygroscopic material (constant $\acute{E}_a$ = 1 GPa), the stiffer the non-hygroscopic passive layer is, the less deflection is caused by a change in relative humidity. The distinct trend of within the same curve below and above 40% relative humidity stems from the humidity dependency of the hygroscopic expansion coefficient.

Figure AP6. 1 (c), on the other hand, highlights the effect of layers' thickness ratio (m) on bending curvature. A thickness of 100 μm for the active layer (h_a) and a constant value of 1 for the materials stiffness ratio (n = 1) were considered. This figure suggests that an increase in the non-hygroscopic substrate thickness (increasing m), reduces the bending curvature. As expected, the thinner the substrate layer, the more deflection there will be. When the thickness ratio is doubled (from m = 1 to m = 2), the bending curvature is practically cut in half. Furthermore, the disparity becomes more pronounced when the humidity level rises.

Last but not least, Figure AP6. 1 (d), shows the effect of the total thickness (h_{tot}). Constant values of 1 for both thickness ratio (m = 1) and materials stiffness ratio (n=1) were considered. The total thickness of the bilayer self-actuator, on the other hand, was varied in a range from 10 μm to 500 μm. Evidently by the increase of the self-actuator's total thickness the bending curvature decreases. Even at humidity levels of less than 40%, a self-actuator with a total thickness of less than 50 μm exhibits much more deflection than a thicker bilayer.

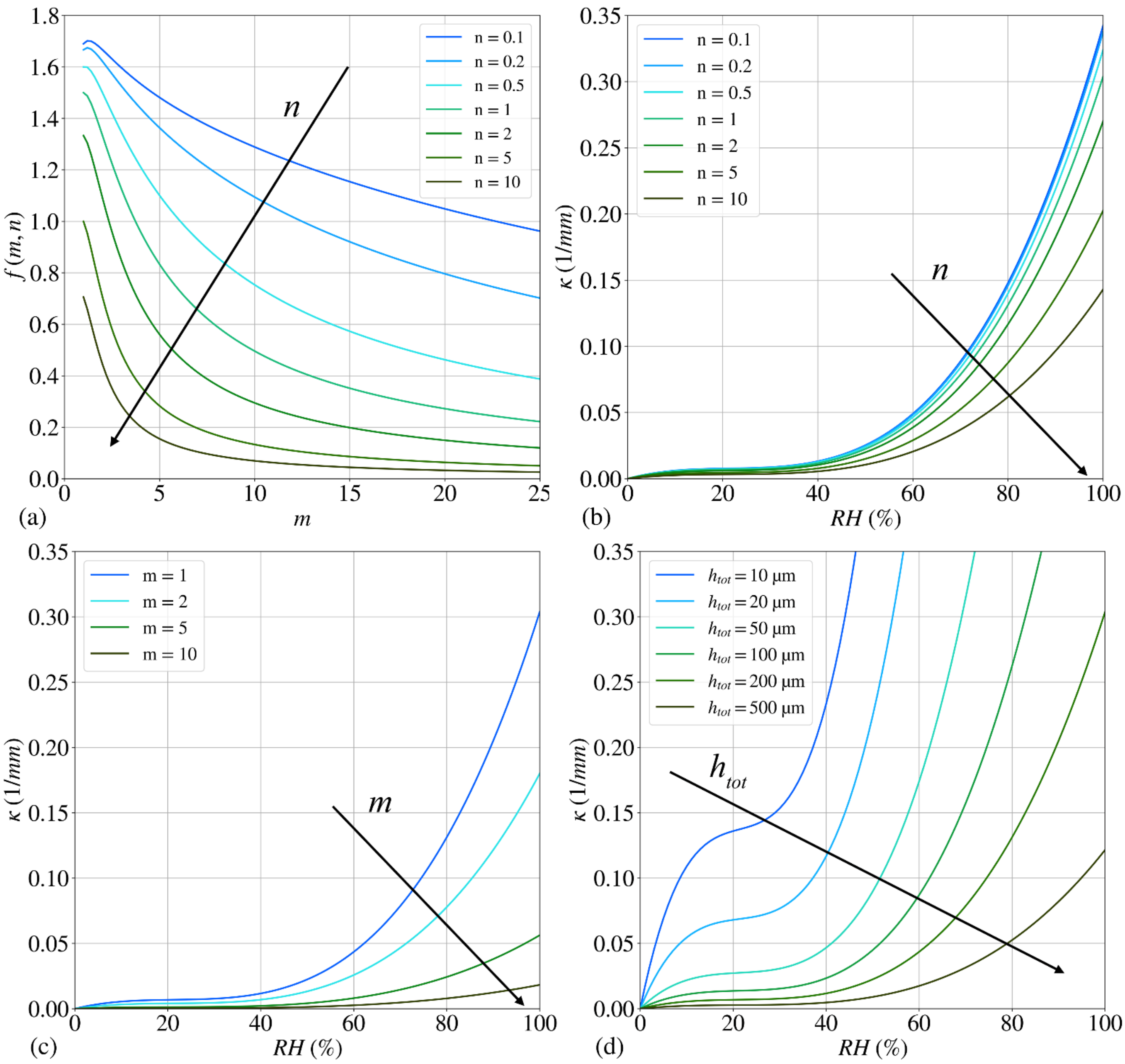

Figure AP6. 1. Parametric study of the bending cantilever model

Appendix 6. 2. Evolution of bending curvature of specimen *S*1 in time

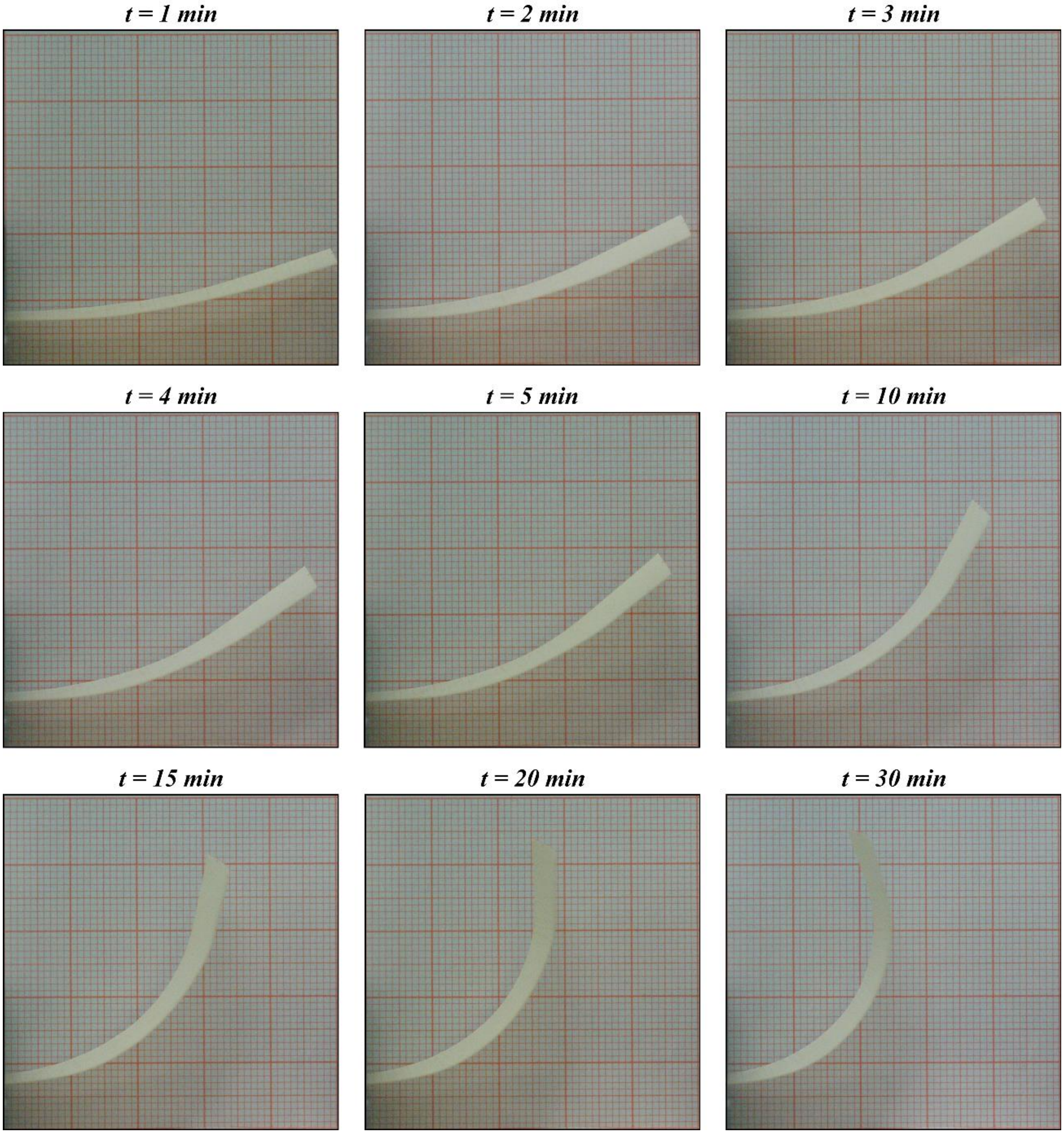

t = 1 min

t = 2 min

t = 3 min

t = 4 min

t = 5 min

t = 10 min

t = 15 min

t = 20 min

t = 30 min

Figure AP6. 2. Digital images of bending curvature evolution of specimen *S*1 in time

Appendix 6. 3. Curvature at RH = 17 %

Figure AP6. 3 portrays the final form of the specimen S1 after 24 hours at the lowest relative humidity possible in the closed chamber (RH=17 %). For the deformation induced by the change of RH from 35% to 17%, a bending curvature (κ) of -0.0199 1/mm was measured.

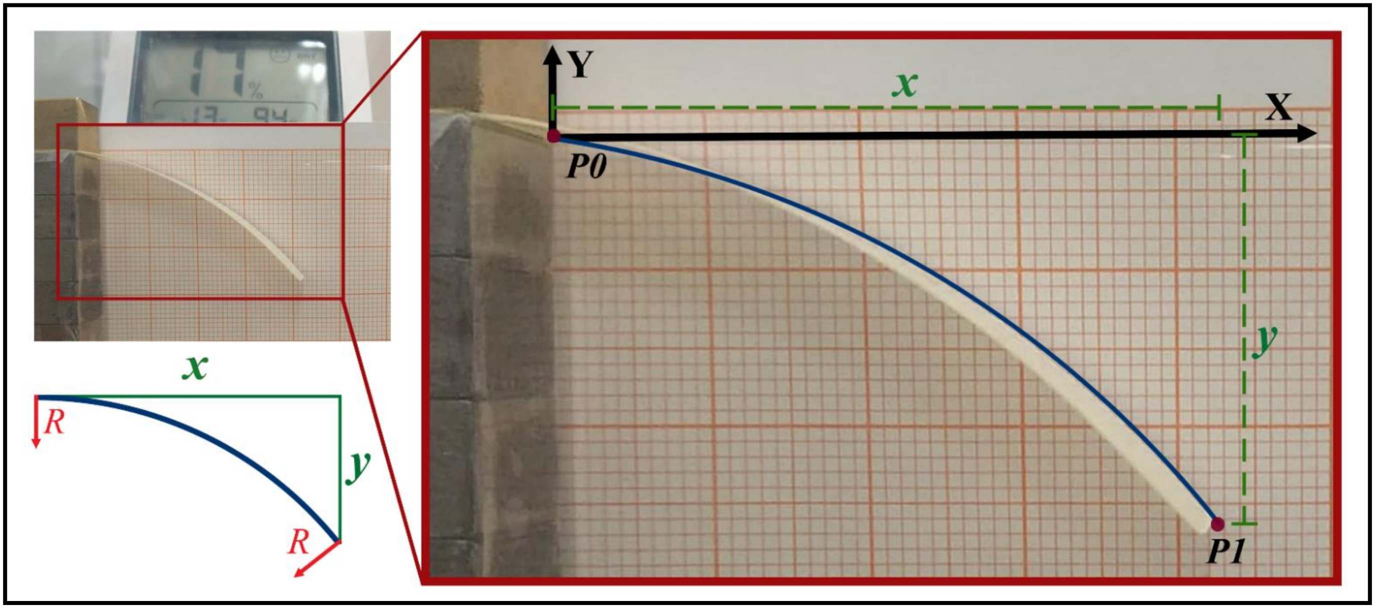

Figure AP6. 3. Bending curvature of the bilayer self-actuator at relative humidity of 17%

7 Conclusions and Further Developments

Toward the development of humidity-responsive layered self-actuators, this thesis explored the possibility of exploiting the humidity sensitivity of hygroscopic materials. The primary objectives were to provide a framework for the fabrication of hygroscopic material membranes, to evaluate the material properties characterizing its hygroscopic behavior, and to develop a comprehensive finite element model for the prediction of a bi-layered self-actuator response to changes in the environment relative humidity.

After a comprehensive review of current advances in the application and characterization of hygroscopic materials, cellulose acetate was chosen as a highly hygroscopic material suitable for this research. The systematic investigation detailed in this thesis for the production of membranes from a cellulose acetate powder highlighted the influence of employed solvent, solution concentration, casting and solvent evaporation methods on the obtained membrane characteristics. Based on: (i) the feasibility of preparing membranes from cellulose acetate solutions with different concentrations, (ii) the time required for the membrane drying, and (iii) the membranes surface quality (its homogeneity) the membrane production process was optimized. The obtained membranes exhibited a smooth surface and no pores at the micro level was visible across the thickness.

The parameters considered in the systematic investigation performed for the optimization of the cellulose membrane preparation process may differ depending on the hygroscopic material's nature (e.g. degree of acetylation of cellulose acetate) or the fabrication technology adopted (e.g. coating of cellulose acetate solution in acetone at industrial level). Nevertheless, the type of experiments carried out, the characteristics considered, and the material properties evaluated (surface, thermal, and mechanical properties) which together define the procedure presented in this thesis can serve as a guide for future studies. It must be noted that, in the scenario of direct application of the hygroscopic coating on the non-hygroscopic substrate in fabrication process, one of the variables that may be included to the assessment step is the interfacial adhesion characteristics between the two layers, which was outside the scope of this thesis.

The characterization of governing properties of hygroscopic behavior, on the other hand, revealed several aspects that had been overlooked in the literature. Gravimetric experiments performed at different values of environment relative humidity at constant temperature demonstrated that the high moisture sensitivity of cellulose acetate impacts the kinetics of moisture diffusion, leading to sigmoidal diffusion and a time-dependent diffusion coefficient (D). On the other hand, due to the limitations of available numerical models, a single value of the moisture diffusion coefficient must be determined for finite element modeling of the diffusion process. The characterization of the non-Fickian behavior with a single value of the diffusion coefficient, required the addition of a new parameter, namely the material relaxation factor (β). The finite element simulation for non-Fickian diffusion has been performed by COMSOL Multiphysics ® 5.6, considering the experimentally measured materials properties. The generated model's accuracy has been validated by a secondary experimental investigation.

The finite element model for prediction of moisture absorption kinetic presented in this research appears to be the first numerical study successful to describe the sigmoidal moisture diffusion of cellulose acetate, which may be extended to other cellulose-based materials as well. It is very difficult to acquire an accurate result for characterization of the moisture diffusion properties of extremely hygroscopic materials due to their rapid reaction to changes in humidity level and the peculiarity of their non-Fickian moisture diffusion behavior. The contributions of this research to experimental, analytical, and numerical modeling lay the groundwork for future studies in the characterization of moisture-sensitive materials such as hydrogels. However, it must be mentioned that the cellulose acetate diffusion coefficient (D) and relaxation factor (β) are expected to vary with the degree of acetylation of the cellulose acetate and on the temperature as well. Due to instrumental and material availability limitations, this research was not able to address and assess the effect of these aspects on the characterized properties.

Another unexpected finding of this research was that, despite conventional assumptions, both the concentration at saturation (C_{sat}) and the hygroscopic strain (ε_{hygro}) exhibit non-linear relationships with environment's relative humidity at constant temperature for the studied cellulose acetate. Two third degree polynomial functions were used to interpolate the relative humidity dependency of these properties, that led to a humidity dependent coefficient of hygroscopic expansion (α). A multiphysics finite element model coupling two phenomena of non-Fickian moisture diffusion and expansion induced by moisture absorption has been developed. Comparing the experimental results of hygroscopic expansion to the predicted values by the adopted numerical model highlighted that the hypothesis of a coefficient of hygroscopic expansion independent on the relative humidity cannot be considered valid for highly hygroscopic materials such as cellulose acetate. These outcomes underscored that for a highly hygroscopic material such as CA, a meticulous attention is needed for the characterization of its hygroscopic behavior.

To the best of author's knowledge, the multiphysics finite element model provided in this thesis for the prediction of the induced bending deformation in the humidity-responsive layered self-actuator due to the variation of humidity level is the first numerical model so far able to predict the evolution in time of the layered composite bending curvature with a good level of accuracy. Moreover, the comparison between the prediction of the layered composite final bending curvature by the proposed finite element model and by the commonly used model known as the bending cantilever model and the experimental results put the stamp of validity on the numerical approach adopted in this research.

Although the similarities between the experimental results and numerical predictions make the presented finite element model very promising, there are other aspects that may be added to the model to make it more comprehensive. Aspects such as the influence of temperature on the mechanical and hygroscopic characteristics of materials may broaden the use of the proposed model for the design and manufacture of humidity-responsive self-actuators in various industrial fields.

In spite of its limitations, the study certainly adds to our understanding and description of the hygroscopic behavior of highly hygroscopic materials in response to the variation in humidity levels in terms of moisture diffusion, hygroscopic expansion, as well as, the induced bending curvature of bilayer self-actuators with a cellulose acetate as active layer. The model presented for the response of the self-actuator to humidity variation, on the other hand, can be used as a design tool before the fabrication process of these humidity-responsive layered self-actuators. This model can provide the manufacturer with a forecast of the response of the self-actuator and aid in the optimization of the actuator's geometrical parameters (e.g. applied coating thickness).

Regarding the development of humidity-responsive layered self-actuators, the next step would be experimental characterization of the hygroscopic behavior of the CA membranes after exposure to the ultraviolet light. Although emergency shelter textiles are expected to have a one-year service life, it would be interesting to investigate the effect of employing TiO_2 or the cyclic variation of temperature on hygroscopic properties and the self-actuator performance. Ultimately, characterization and numerical modeling of indoor air quality using these actuators to monitor the performance of the presented solution.

Concerning potential advancements in the utilization of hygroscopic materials, research on composites of hygroscopic and conductive or piezoelectric materials to produce multi-responsive sensors or energy harvesting devices may be of interest. A composite membrane made of hygroscopic and piezoelectric materials, for example, can be employed as a covering for outdoor surfaces in tensile membrane structures. In humid or rainy conditions, hygroscopic expansion causes mechanical deformation in piezoelectric materials, which results in electrical current. Furthermore, despite advancements in manufacturing methods, the use of hygroscopic materials as fiber sheaths in the design of breathable and waterproof woven textiles appears promising.

Acknowledgement

I would like to express my deepest gratitude to my both families in Iran and in Italy. A special thanks to my sister ***Shirin*** for her continuous support throughout my academic life and to ***Danilo*** for his unwavering encouragement through this experience.

A debt of appreciation is owed to my supervisors, ***Prof. Carvelli*** and ***Prof. Marano***, for teaching me with a great level of patience. Thanks to them I have new horizons, and I know better my limits and potentials. I have to thank also ***Prof. Dotelli*** and ***Prof. Monticelli*** for their availability and support. Surely, I have to thank all the ***members of PolyEngLab*** for challenging my knowledge by asking me practical questions, which helped the development of my project. A special thanks to ***Prof. Pavan*** for his advice and scientific approach through the lens of experience.

There are so many people that I have to thank for their contributions. The completion of this thesis could not have been possible without my colleagues ***Stefano***, ***Tiziana***, ***Lorenzo***, ***Isabella*** who helped me to think loud, and the technicians of the laboratory, ***Oscar*** and ***Marco*** who accompanied me through the experiments. Last but not least, I would like to thank my committee members for their insightful comments and precious questions.

It’s the moment for me to drop the mic, but the show must go on.